DEVELOPMENT OF AN IN-SITU ALLOYED MICROSTRUCTURE IN LASER ADDITIVE MANUFACTURING

DEVELOPMENT OF AN IN-SITU ALLOYED MICROSTRUCTURE IN LASER ADDITIVE MANUFACTURING

BY

FARHEEN FATHIMA AHMED, B. A. Sc.

A THESIS

SUBMITTED TO THE DEPARTMENT OF MATERIALS SCIENCE AND ENGINEERING

AND THE SCHOOL OF GRADUATE STUDIES

OF MCMASTER UNIVERSITY

IN PARTIAL FULFILMENT OF THE REQUIREMENTS

FOR THE DEGREE OF

MASTER OF APPLIED SCIENCE

Master of Applied Science (2020) McMaster University

(Materials Science and Engineering) Hamilton, Ontario, Canada

TITLE:	Development of an In-Situ Alloyed Microstructure in Laser Additive Manufacturing
AUTHOR:	Farheen Fathima Ahmed B. A. Sc. (Materials Engineering), University of Toronto, Toronto, Canada
SUPERVISOR:	Dr. André B. Phillion
CO-SUPERVISOR:	Dr. Hatem Zurob
NUMBER OF PAGES:	xxiii, 122

Preface

With the exception of the following contributions, I am the primary contributor to this work:

- Dr. André Phillion: Running of sXRD experiments, supervision, editing
- Dr. Hatem Zurob: Supervision, editing, running ThermoCalc^{TM} calculations
- Dr. Samuel Clark: Running of sXRD experiments, conversion of 2D .cbf frames to 1D frames via MATLAB, conversion of IR frames to temperature fields and alignment, writing of Rosenthal solution code, editing of Chapter 5: Results and Discussion
- Dr. Peter Lee: Supervision of sXRD experiments, editing of Chapter 5: Results and Discussion
- Dr. Chu Lun Alex Leung and Sebastian Marussi: Running of sXRD experiments, editing of Chapter 5: Results and Discussion
- Leigh Stagner and John Wilmott: Development and calibration of IR detector
- Yunhui Chen and Lorna Sinclair: Running of sXRD experiments
- Dr. Veijo Honkimaki: Assistance with sXRD experiments

- Noel Haynes and Dr. Roque Panza-Giosa: Advice with interpreting results
- Dr. Khaled Abu Samk: Aiding with sample preparation and running ThermoCalc™ calculations
- Dr. Mirnaly Saenz de Miera: Running EBSD

In Chapter 1: Introduction, I give an introduction to laser Additive Manufacturing (AM), and the value of *in-situ* alloying, or printing with elemental powders. In Chapter 2: Literature Review, I explain the research that has been performed to date on laser AM with elemental powders. In Chapter 3: Scope and Objectives, I identify the need to study the alloying process in detail, and state the objectives of this project. In Chapter 4: Methods, I detail the synchrotron X-Ray Diffraction (sXRD) and Infrared (IR) experiments, the Rosenthal Solution estimate, and the Electron Microscopy performed. In Chapter 5: Results and Discussion, I explain and discuss the findings of this project. A paragraph in Section 4.4: Rosenthal Temperature Predictions is taken from the paper *Achieving homogeneity in a high-Fe β-Ti alloy laser-printed from elemental powders* by F. F. Ahmed (the author of this thesis), S. J. Clarke, C. L. A. Leung, L. Stagner, J. Wilmott, S. Marussi, V. Honkimaki, N. Haynes, P. D. Lee, H. S. Zurob and A. B. Phillion. (The contributions of each author have been explained above.) Sections 5.2: Results and 5.3: Discussion in this chapter are also included in the paper mentioned above. Chapter 6: Conclusions and Future Work summarizes the importance and findings of the project, and explains a few avenues for future research based upon this topic.

Abstract

Additive Manufacturing (AM) processes are gaining prominence in industry as they can build parts to near-net-shape with minimal postprocessing. Metal laser AM techniques, such as Selective Laser Melting (SLM), offer rapid cooling rates on the order of $10^5 - 10^6$ K/s. This is due to a highly-focused laser heating a microscopic volume in an otherwise lower-temperature environment. Hence, metal laser AM can manufacture novel, out-of-equilibrium microstructures that cannot be produced in near-net-shapes with other processes. It is desirable to optimize feedstocks for metal AM processes to leverage their advantages. One option of optimizing feedstocks is through *in-situ* alloying, or by using elemental powders. Elemental powders homogenize over the course of multiple laser passes, or intrinsic heat treatments. However, rapid cooling rates prevent the homogenization of a layer when first printed. To investigate the homogenization process, this thesis used synchrotron X-ray Diffraction (sXRD) to track the phase transformations during the SLM of a 14-layer single wall (single-hatch, multilayered) of Ti-1Al-8V-5Fe (Ti-185) from elemental Ti, Fe and an alloyed AlV powders, capturing frames at 250 Hz. Infrared imaging was performed simultaneously on the surface at 1603.5 Hz to observe the temperature changes at the surface. Post-mortem electron microscopy was performed on cross-sections of the wall perpendicular to the scanning direction to observe the changes in the microstructure

with respect to the build direction. Specifically, Electron Dispersive X-Ray Spectroscopy and Electron Backscatter Diffraction were performed to observe the alloying elemental distribution and microstructure of the wall with respect to the build direction. The research performed found that in the melted zone, phase transformation times below 50 ms yielded a partially-alloyed microstructure, with regions concentrated and dilute in alloying elements. Partial mixing was diffusion-induced by laser beam heat and the exothermic heat of mixing of Ti-185 from its constituent elements. Further diffusion during reheating cycles yielded an alloyed microstructure.

To Ambreen and Ian

Acknowledgements

I would like to thank Dr. André Phillion and Dr. Hatem Zurob for their supervision, guidance and mentorship over the past two years. Their enthusiasm for Materials research and their dedication to helping their students succeed made for an enjoyable two years working with them. They always took out the time to meet with me and guide me through my research. They gave me opportunities to share my work and learn from other researchers by sending me to conferences. They taught me to be a better researcher, and I am happy to take their lessons with me as I continue onto the next chapter.

I extend my gratitude to Dr. Peter Lee at University College London for giving us the opportunity to collaborate with his research group on synchrotron experiments, and for his guidance and encouragement. I thank Dr. Samuel Clark for helping me with data processing, and for his guidance and encouragement in completing this project. He answered my many emails clarifying details that helped me in my research, and always tried to help me find a solution when I had an issue with the analysis. I thank Dr. Chu Lun Alex Leung, Dr. Yunhui Chen, Lorna Sinclair and Sebastian Marussi for helping with running sXRD. I thank Leigh Stagner and John Wilmott for developing and calibrating the IR machine to use in the synchrotron experiments. I thank Veijo Honkimaki for aiding with sXRD experiments at the

European Synchrotron Radiation Facility.

I would like to thank the members of Dr. Phillion and Dr. Zurob's research groups for their help and feedback at various points in my research, their encouragement and their friendship. Specifically, I would like to thank Dr. Khaled Abu Samk for helping me with sample preparation, Dr. Mirnaly Saenz de Miera for operating EBSD, and Niloufar Khodaei for helping me with troubleshooting LaTex in writing my thesis.

I would like to thank Dr. Jim Britten and Vicky Jarvis of the McMaster Analytical X-Ray Diffraction Facility for their help in interpreting data, and for what I have learned from them about XRD. What they taught me was very valuable in understanding the limitations of my data, and finding the best way to analyse it.

I would like to thank the Canadian Centre for Electron Microscopy (CCEM) for access to its SEMs to perform BSE imaging, EDX and EBSD. I also appreciate the training and guidance from Jhoynner Martinez and Chris Buther at the CCEM.

I would like to thank Dr. Michel Rappaz at École Polytechnique Fédérale de Lausanne for his guidance on my research, and encouraging me to think outside the box in finding solutions to analysis limitations. I also appreciate his enthusiasm on novel Additive Manufacturing research.

I would like to thank Collins Aerospace for the funding for this project. I also thank Noel Haynes and Dr. Roque Panza-Giosa of Collins Aerospace for their guidance, specifically, for their insight on phase transformations in titanium. I had valuable conversations with them that helped me in my analysis.

I also extend my gratitude towards the the families of H. G. Hilton and Dr. Dante Cosma for their generosity through the H. G. Hilton Memorial Scholarship and Dante Cosma Scholarship respectively.

I would like to thank the Engineering Graduate Society and the Materials Student Technical Society for giving me an opportunity to give back to the McMaster community. They made my final year very enjoyable.

I would like to thank my mentors for their encouragement, advice and support: Robert Alicandri, Dr. Matthew Daly, Kevin Dulhanty and Dr. Chandra Singh. Special thanks to my mentor Dr. Glenn Hibbard, who showed so much excitement for me as if I had never left his group at the University of Toronto, and whose dedication to my learning in undergrad prepared me for my Masters. I have grown the wings of the McMaster Eagle, but my roots are still planted firmly at U of T.

I would like to thank my friends who have looked out for me, helped me out, encouraged me and given me many reasons to laugh over these past two years. They include Andy Ho, Sabat Ismail, Christine McCart and Saad Rahimi. I would also like to thank Sara Filice and Jaime Jewer for the sense of humour and kindness they always brought to our office. A very special thanks to my closest friend and boyfriend Ian Phillips for his love, care, friendship, encouragement and a library's worth of puns. I cannot explain what it means to me.

Finally, I extend my gratitude to my family. I would like to thank my aunt Asma Ahmed for her encouragement, love, and dedication to helping me. I would also like to thank Faraz Nomani, Yusuf Nomani, Humzah Nomani, Maryam Nomani, Imran Ahmed, Sumaiyah Rehman, Nusayba Ahmed, Anam Nomani, Ammar Ashraf, Hassan Ashraf and Zainab Ashraf for their love and encouragement. Last, I owe a very large thank-you to my sister Ambreen Ahmed for her love, care, friendship, encouragement and her sense of humour. I could not have imagined the past two years without our many jokes shared together over texts, calls and of course, while dining on sushi on

a pre-pandemic night in Toronto. Every moment of it is warmly appreciated.

Contents

Preface **iii**

Abstract **v**

Acknowledgements **viii**

List of Figures **xx**

List of Tables **xxi**

List of Acronyms **xxii**

List of Symbols **xxiv**

1 Introduction **1**

1.1 An Introduction to Laser Additive Manufacturing 1

1.2 The Need for *In-Situ* Alloying 4

2 Review of the Literature on *In-Situ* Alloying in Laser AM **7**

2.1 Introduction 7

2.2 Bulk Microstructure 8

2.3 Surface Microstructure and Melt Pool Behaviour 17
2.4 The Gradient between the Surface and Bulk Microstructure 18
2.5 Strategies to Improve Homogeneity 20
2.6 Conclusion 25

3 Scope and Objectives **28**
3.1 Scope 28
3.2 Objectives 36

4 Methods **38**
4.1 Introduction 38
4.2 Materials 38
4.3 Real-Time sXRD and IR Experiments 41
4.4 Rosenthal Temperature Predictions 47
4.5 Post-Mortem Analysis of the Printed Wall 49
4.6 Chapter Summary 55

5 Results and Discussion **56**
5.1 Introduction 56
5.2 Results 57
5.3 Discussion 66
5.4 Chapter Summary 71

6 Conclusions and Future Work **74**
6.1 Thesis Summary and Concluding Remarks 74
6.2 Recommended Future Work 76

A Plotting of Individual XRD Frames **78**

A.1 MATLAB Script to Import and Sort .mat Files 78

A.2 MATLAB Script and Function to Open and Plot data for each file . . 96

B Conversion of Infrared Images to Temperature Fields **103**

List of Figures

1.1 The process of a) SLM, b) DED and c) LWMAM. a), b) and c) are taken from [1], [2] and [3] respectively. 3

1.2 a) Secondary electron image of an elemental powder mixture containing Ti, Ni and Al powders. b) DED using separate hoppers for different elemental powders. The augers were used to control the powder concentration in the mixture. c) EDX images showing homogeneity in the bulk microstructure of elemental Cu and 316L-steel powders printed via SLM. The consistency of the EDX image of Cu (bottom left) demonstrates that alloying was achieved. a), b) and c) are taken from [4], [5] and [6] respectively. 5

2.1 Elemental distribution in the SLM of CoCrFeNi and elemental Mn at energy densities of a) 120 J/mm^3 and b) 259 J/mm^3. Stronger mixing of Mn in the alloy is demonstrated in b) over a). Taken from [7]. . . . 9

2.2 SEM image (top) and spatial elemental distribution of alloying element (bottom) of a) (Left) Ti-Cr and b) Ti-Nb printed via DED. Taken from [8]. 11

2.3 Relationship between energy density, the presence of defects and the degree of alloying in NiTi printed via SLM. Taken from [9]. 14

2.4 a) X-ray tomographic reconstruction of Ti-22Al-25Nb printed via SLM from elemental Ti, Al and Nb. Purple represents the Ti-Nb-Al phase. Red represents the volume without Nb. Yellow represents the unalloyed Nb particles. Blue represents the porosity. b) shows only the unalloyed Nb. Taken from [4]. 14

2.5 Backscatter electron images of a), b) W6Ni2Fe2Co, c), d), W12Ni4Fe4Co and e), f), W18Ni6Fe6Co printed via SLM. The build direction is facing upwards. Taken from [10]. 16

2.6 (Left) Secondary electron and (Right) EDX images showing a single layer of MoNbTaW printed via DED on a Mo substrate. Adapted from [11]. 18

2.7 (Left) Trajectories of tungsten particles in an Al-6061 melt pool during SLM. Taken from [12]. 19

2.8 a) Composition of Al and V in a Ti-6Al-4V single wall printed via SLM along the build direction from the substrate (-0.3 mm) to the surface (2.1 mm). b)-d) Microstructure at the top, middle and bottom of the sample respectively. Taken from [13]. 21

2.9 Microstructure at the a) top and b) bottom of a single wall of Ti-Mo printed via DED. Taken from [14]. 22

2.10 (Left) Secondary electron and (Right) EDX images of a MoNbTaW layer printed via DED on a Mo substrate a) without and b) with remelting. a) was previously shown in 2.6. Taken from [11]. 22

2.11 a) Difference in composition at different scan speeds in the SLM of TiTa with and without remelting. b), c) Microstructure without and with remelting respectively. Taken from [15]. 23
2.12 Comparison between expected and actual compositions in the DED of MoNbTaW high-entropy alloys, where nozzle speeds were directly proportional to the desired concentration. Taken from [5]. 24
2.13 a), b), e) and g) Microstructure and c), d), f and h) EDX images of the microstructure printed via SLM through the powder set Simply Mixed 1 (Coarse Ti, Al and V powders). Taken from [16]. 26
2.14 a), b) Microstructure and c), d) EDX images of the microstructure printed via SLM through the powder set Simply Mixed 2 (Coarse Ti, fine Al and V powders). The arrow points to a region high in Ti along a melt pool striation. Taken from [16]. 26
2.15 a), b) Microstructure and c), d) EDX images of the microstructure printed via SLM through the satellited powder mixture. Taken from [16]. 27
3.1 a) (Left) Diagram of sXRD with DED. b) (Right) A customized beamline-compatible DED replicator. Taken from [17]. 31

3.2 a) A sample of three 2D sXRD images at -1 (a1), 3.5 (a2) and 11 (a3) ms with respect to the arrival of the laser at the acquisition volume (0 ms) during the SLM of Ti-6Al-4V. A diffraction spot corresponding to a coarse grain is shown at 3.5 ms (a2). b) A 1D series of diffraction acquisition patterns with respect to time. Colour represents the intensity of peaks, demonstrating phase transformations. c) Evolution of the α-{101} and β-{110} peaks with respect to time. Taken from [18]. 32

3.3 Psuedo-binary Ti phase diagram as a function of increasing β-stabilizer concentration. Taken from [19]. 34

3.4 a) Optical micrograph of the microstructure of Ti-185 printed via SLM from elemental powders. b) is a high-resolution close-up of the box specified in a). Taken from [20]. 35

4.1 a) Secondary electron image of the elemental Ti, Fe and AlV powder mixture used in this study. b) XRD of powder. c) Powder size distribution. Taken from [20]. 40

4.2 Setup of the ISOPR. Image provided by Samuel Clark. 43

4.3 Setup of SLM concurrent with sXRD and IR imaging in the ISOPR. For the purpose of highlighting important features of the setup, this diagram is not to scale. 44

4.4 a) cp-Ti substrate on which the Ti-185 single wall was printed. b) shows a close-up of the printed wall. 44

4.5 Position of the X-ray beam during sXRD relative to the powder layer and the printed layers beneath it. 45

4.6 Accumulation and diffraction of unmelted powder between the printed Ti-185 layers and the glassy carbon walls. 46
4.7 Imaged face for electron microscopy. 50
4.8 a) Sections of the sample formed by cutting. b) Imaged face of the resulting section. 51
4.9 The sample prior to being cut in the precision cutter. Two jets of water are on either side of the blade. 52
4.10 a) Cut sample mounted in epoxy. b) is a close-up of the printed layers in a). 52
4.11 Secondary electron image of the grinded and polished epoxy-mounted sample. Cu tape and Ni paste are also featured on the mount. 53
5.1 Time- and position-dependent temperature profile at the surface as a (top) two-dimensional map and (bottom) one-dimensional centreline profiles during SLM. For reference, the melting point of titanium (1941 K) is also plotted as a gray, dotted line. At points i) and iii), the heating and cooling rates are 1,000 K/ms; at point ii), the maximum temperature observed, 2830 K; at point iv), a cooling rate of 200 K/ms is observed. 58
5.2 Estimation of the steady-state sub-surface temperatures via the Rosenthal equation assuming an input power of 290 W. The x- and z- axes are not to scale relative to one another to emphasize the temperature gradient in the z-direction. 59
5.3 Melt pool sXRD. Frames are shown before printing (0 ms), at the start of the phase transformation (4 ms) and at its completion (64 ms). . . 61

5.4 a) Post-phase-transformation sXRD frames after each laser pass when a single layer is tracked through reheating cycles. The duration of each phase transformation is also shown. b) and c) show the $\alpha\{102\}$ and β-$\{002\}$ peaks in the 2ϑ=5.5-6.7° range magnified by a factor of 13.3 at depths of 75 and 100 µm respectively. 63

5.5 a) BSE image of the printed layers cross-sectioned perpendicular to the scanning direction. b) EDX maps of Ti, Fe, Al and V. 65

5.6 a) EBSD Orientation map and b) phase map of the microstructure. c) Orientation map and d) phase map of a high-resolution image of a melted zone area highlighted in a) and b). In b) and d), α and β are represented by red and blue respectively. e) Legend for orientation maps map in a) and c). Grain orientations are with respect to the build direction (vertical, pointing upwards). The scanning direction is into the page. 67

List of Tables

4.1 Values of Ti-6Al-4V inputted into the Rosenthal equation. Values were taken from [21]. 48

List of Acronyms

AM Additive Manufacturing

BCC Body-Centred Cubic

BSE Backscatter Electron

DED Direct Energy Deposition

DLD Direct Laser Deposition

EBSD Electron Backscatter Diffraction

EDX Electron Dispersive X-Ray Spectroscopy

HCP Hexagonal Close-Packed

ISOPR In-situ and Operando Processing Replicator

IR Infrared

LWMAM Laser Wire-Feed Metal Additive Manufacturing

LPBF Laser Powder-Bed Fusion

SLM Selective Laser Melting

SEM Scanning Electron Microscope

sXRD synchrotron X-Ray Diffraction

XRD X-Ray Diffraction

List of Symbols

α Absorptivity

ρ Density [$\mathbf{kg/m^3}$]

b Thickness of printed layers/substrate [$\boldsymbol{\mu}\mathbf{m}$]

c Heat capacity [$\mathbf{J/kg{\cdot}K}$]

k Thermal conductivity [$\mathbf{W/m{\cdot}K}$]

Q Laser power [$\mathbf{W}$]

T Temperature [$\mathbf{K}$]

T_0 Ambient temperature [$\mathbf{K}$]

t Time elapsed from contact with laser [$\mathbf{ms}$]

V Laser speed [$\mathbf{mm/s}$]

x Distance to laser along the scanning direction (sXRD and IR experiments) [$\mathbf{mm}$]

x_0 Distance to laser along the scanning direction (Rosenthal solution) [$\mathbf{mm}$]

$\bar{x_0}$ Dimensionless coordinate (scanning direction) as used in the Rosenthal Equation **[mm]**

y Distance to laser along the thickness direction **[mm]**

z Distance to laser along the build direction (sXRD and IR experiments) **[mm]**

z_0 Distance to laser along the build direction (Rosenthal solution) **[mm]**

$\bar{x_0}$ Dimensionless coordinate (build direction) as used in the Rosenthal Equation **[mm]**

Chapter 1

Introduction

1.1 An Introduction to Laser Additive Manufacturing

In 2018, the Additive Manufacturing (AM), also termed 3D-printing, economy in North America was worth $3.9 billion USD and was projected to reach $51.77 billion USD by 2026, highlighting the importance of AM as a viable manufacturing process [22]. AM processes are those in which an object is formed, or printed, layer-by-layer from a feedstock. A computer-designed model outputs a pattern for each layer which corresponds to its cross-section area at that specific height [1]. AM offers multiple benefits that make it a growing process in the global economy. Parts can be produced with very few postprocessing steps. As a result of this, and because the process is additive, the buy-to-fly ratio (ratio of input to output material in a manufacturing process) is high. For example, for an aerospace engine, AM can reduce the buy-to-fly ratio from 10:1 to almost 1:1 [23]. Lattices, internal channels, and undercuts,

geometries which are difficult to produce via other methods, can be produced [24]. It also offers an opportunity for part repair. Additionally, less human labour is required than other processes, with labour costs consisting of only 2-3% of the total cost in printing. AM can be applied in multiple fields, such as biomedical, aerospace, automotive and oil and gas applications [23].

Laser AM techniques are valuable to manufacture novel alloys. These processes use a finely-focused laser to melt powder or wire in a series of layers. Selective Laser Melting (SLM), also termed Laser Powder Bed Fusion (LPBF), utilizes a powder bed as shown in the diagram in Figure 1.1 a). A layer of powder is deposited from a reservoir onto a substrate, and fused with the laser. From the reservoir, another layer of powder is deposited upon the previous layer, and another layer is printed. This process continues until a part is built. Direct Energy Deposition (DED), also termed Direct Laser Deposition (DLD), injects powder into the laser beam via nozzles, where it melts and fuses onto the part [25]. A diagram of DED is shown in Figure 1.1 b). Another technique, better suited for larger materials, is Laser Wire-Feed Metal Additive Manufacturing (LWMAM), in which a wire is fed into the system instead of powder, as shown in Figure 1.1 c) [26]. Laser additive manufacturing processes offer extremely high cooling rates on the order of $10^5 - 10^6$ K/s [27]. The resulting microstructures are, in the terms of Boussinot et al., "strongly out of equilibrium" [28]. The cooling rates can be leveraged produce novel microstructures, and hence, novel materials, that cannot be processed with conventional techniques such as casting, which have significantly lower cooling rates.

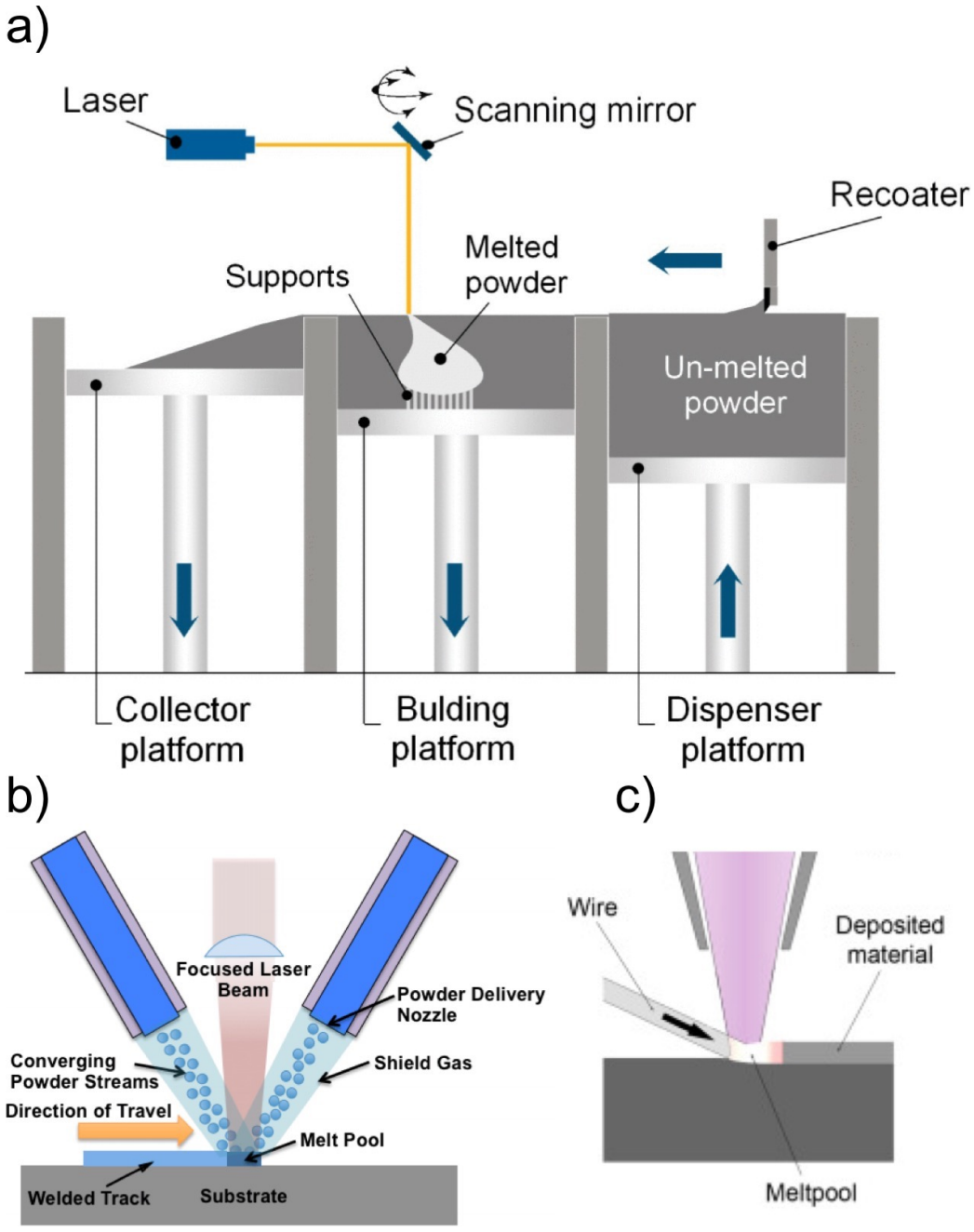

Figure 1.1: The process of a) SLM, b) DED and c) LWMAM. a), b) and c) are taken from [1], [2] and [3] respectively.

1.2 The Need for *In-Situ* Alloying

Because the field of AM is relatively novel, alloys designed for optimized processing and properties with other techniques are conventionally used in AM. To make the most of laser AM, the opposite needs to be done, i. e. optimize the compositions of alloys to leverage the advantages of AM to yield the most ideal properties for a given application [29]. Developing optimal powder compositions is expensive, as it involves producing, printing and testing different feedstocks. Finding optimal feedstocks are crucial to the progress of laser AM, as materials costs consist of a significant part of the total cost in AM [23].

There is an emerging technique called *in-situ* alloying, however, which uses elemental powders instead of pre-alloyed powders [25]. An example of an elemental powder mixture is shown in 1.2. The elemental powders alloy within the melted and heat-affected zones during AM to generate an alloyed microstructure [30]. The diagram in Figure 1.2 b) shows the printing of alloys via DED from an elemental feedstock. Figure 1.2 c) shows an example of an alloyed bulk microstructure. *In-situ* alloying offers a wide range of alloying customizability, which is very useful for research and development. It is also less expensive than fabricating and printing pre-alloyed powders, offering cost savings during manufacturing. Additionally, the process may be aided by an exothermic heat release during mixing, reducing the powder input needed. Furthermore, it is easy to produce functionally graded alloys, i. e. alloys that vary spatially in their compositions [30]. The process of *in-situ* alloying is shown in Figure 1.2.

Though studies on in-situ alloying have verified that alloying can be achieved in the bulk microstructures with the desired printing parameters, a layer is initially not

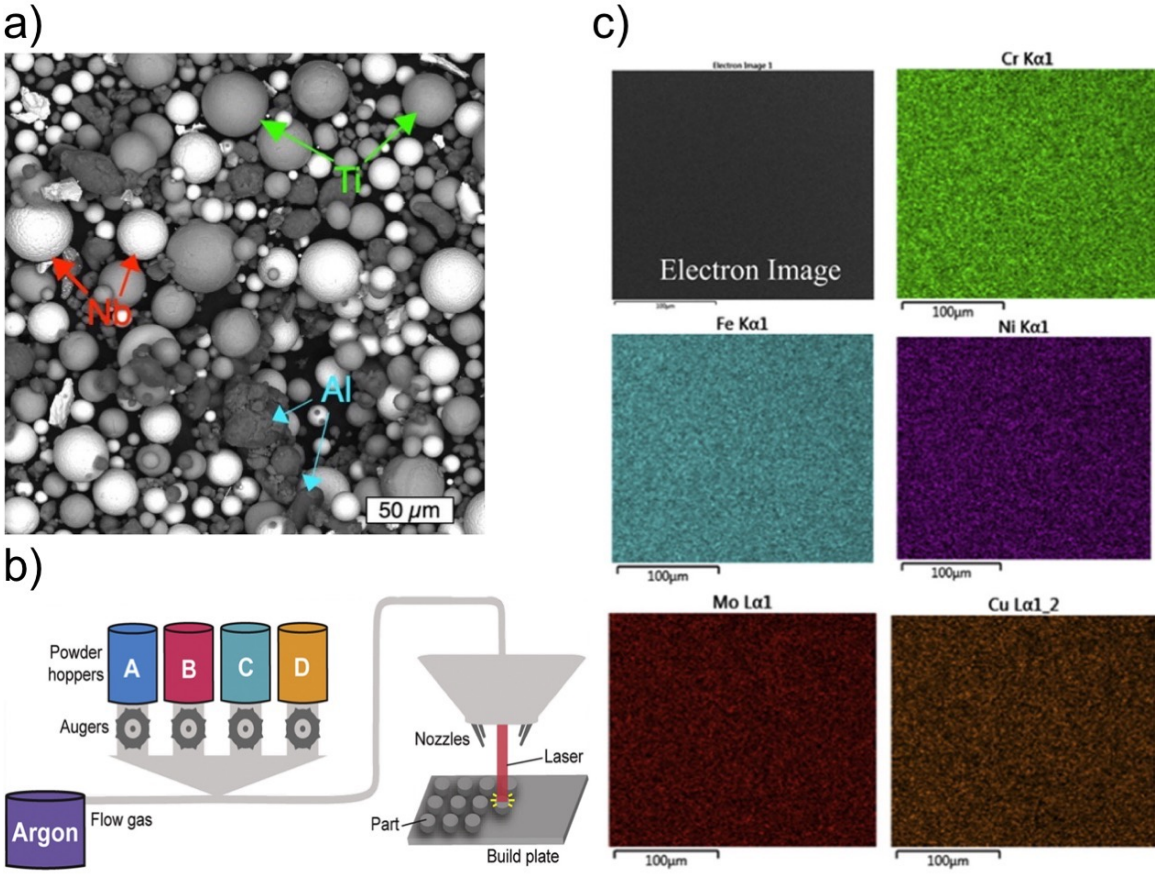

Figure 1.2: a) Secondary electron image of an elemental powder mixture containing Ti, Ni and Al powders. b) DED using separate hoppers for different elemental powders. The augers were used to control the powder concentration in the mixture. c) EDX images showing homogeneity in the bulk microstructure of elemental Cu and 316L-steel powders printed via SLM. The consistency of the EDX image of Cu (bottom left) demonstrates that alloying was achieved. a), b) and c) are taken from [4], [5] and [6] respectively.

homogenous upon printing, with unmelted powders potentially remaining [31, 11]. Via intrinsic heat treatments caused by the laser as it prints layers above it, the originally printed layer transforms its microstructure each time, becoming more homogenous at each step. With optimal parameters, alloying can be completed by the time it is outside the heat-affected zone [20, 8, 6, 32, 33, 9, 7]. However, the process of developing an alloyed microstructure is not well known. This is the gap in the literature that this research aims to fill. Chapter 2: Review of the Literature on Elemental Powders in Laser AM will detail the current literature on using elemental powders. With the foundation of Chapter 2, Chapter 3: Scope and Objectives will explain the research which needs to be performed for a stronger understanding of developing an alloyed microstructure, and outline the objectives that this research aims to accomplish. Chapter 4: Methods will explain the printing and analysis techniques used to understand alloying further. Chapter 5: Results and Discussion will show the findings and use them to explain the alloying process. Chapter 6: Conclusions and Future Work will conclude this thesis, and offer future avenues for research.

Chapter 2

Review of the Literature on *In-Situ* Alloying in Laser AM

2.1 Introduction

The objective of this review is to provide the reader with an understanding of how homogeneity is achieved in *in-situ* alloying in laser AM, the factors influencing whether homogenization is complete, and strategies to improve homogenization. First, this chapter shows examples in which homogeneity was achieved in the bulk microstructure. This review then explains factors that influence whether homogeneity is achieved, such as the enthalpy of mixing and the difference in melting point between different elements. An exothermic enthalpy of mixing aids in mixing by providing additional heat which promotes diffusion. High-melting-point elements may take longer to mix due to their lower tendency to melt. The melting and boiling point difference also raises the issue of vaporization of low-melting-point/high-vapour-pressure elements. While homogenization may be achieved in the bulk microstructure, attention must

also be paid to the surface, where layers undergo only a single heating cycle: that which transformed them from powder to printed material. It is explained how alloying is incomplete at the surface as a result of rapid cooling. As for the gradient between the final layer and the bulk microstructure, a few studies have investigated this, and their findings are discussed. Strategies for improving homogeneity, including remelting, increasing the build temperature and satelliting, are then explained. This review builds the knowledge required to understand the need for a thorough study investigating the alloying process, which will be discussed further in Chapter 3: Scope and Objectives.

2.2 Bulk Microstructure

2.2.1 Achievement of Homogeneity in the Bulk microstructure

Multiple examples of *in-situ* alloying in laser AM have demonstrated complete homogenization of the bulk microstructure. For example, Schwendner *et al.* first achieved homogeneity in the printing of Ti-10Cr (at. %) via DED in 2001 [8]. Wang *et al.* printed 316L-steel with Cu powder at 25 and 50% Cu powder via SLM, and found that Cu had dissolved in the 316L-steel [6]. Azizi *et al.* printed Ti-1Al-8V-5Fe via SLM from Ti, Fe and an alloyed AlV powder, and obtained a homogenous microstructure [20]. Polozov *et al.* printed Ti-5Al via SLM and found that Al had fully dissolved in Ti [32]. Schönrath *et al.* printed Ni-21.5Fe via SLM and found that at a high energy density of 429 J/mm^3, homogeneity was achieved. However, this sample was more porous than its inhomogeneous lower-energy-density counterpart, printed at 71

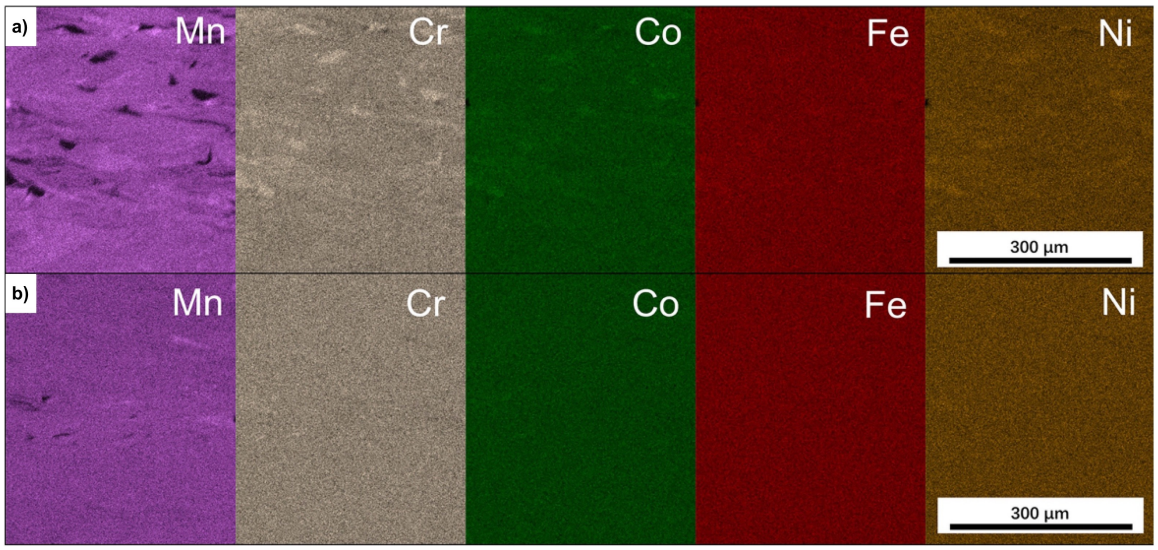

Figure 2.1: Elemental distribution in the SLM of CoCrFeNi and elemental Mn at energy densities of a) 120 J/mm^3 and b) 259 J/mm^3. Stronger mixing of Mn in the alloy is demonstrated in b) over a). Taken from [7].

J/mm^3, potentially due to higher material evaporation [33]. Wang *et al.* found in the printing of Ni-Ti (powders mixed 50% by volume) via SLM that homogeneity was mostly achieved at a high energy density (130 J/mm^3), however, there were many keyhole defects [9]. Chen *et al.* printed a high-entropy alloy from an alloyed CoCrFeNi and elemental Mn powder via SLM. As shown in the EDX maps in Figure 2.1 c), they found that the sample was not homogenous at a low energy density of 120 J/mm^3. However, as shown in the maps in in Figure 2.1 d), homogeneity was mostly achieved at 259 J/mm^3 [7]. This will be discussed further in Section 2.2.2: Factors Influencing Homogeneity in the Bulk Microstructure.

2.2.2 Factors Influencing Homogeneity in the Bulk Microstructure

Enthalpy of Mixing

The mixing enthalpy of the constituent powders will influence how easily it mixes. This was first demonstrated in 2001 by Schweneder *et al.* They compared the DED of Ti-10Cr and Ti-10Nb (at. %) via elemental powders. As shown in Figure 2.2 a), a homogenous microstructure was achieved in Ti-10Cr. Its SEM image (top) appeared consistent without heterogeneities. An EDX linescan through a layer (bottom) confirmed this finding by showing that the composition varied by only ±0.6%. However, as shown in Figure 2.2 b), Ti-10Nb did not homogenize. Unmelted Nb was observed between layers in its SEM image (top). An EDX linescan through a layer (bottom) demonstrated a ±3% variation in concentration. They attributed this to the mixing enthapies of Ti with Cr and Nb, which are -12.7 kJ/mol and 4.2 kJ/mol respectively [8]. However, this may also be attributed to the melting point difference between Cu and Nb, which are 1,358 K and 2,750 K respectively. This will be discussed in the next subsection.

Melting Point Difference

With a significant difference in melting points, a higher-melting-point component may not fully melt and dissolve, and hence the microstructure may only be partially alloyed. In 2010, Fallah *et al.* printed Ti-Nb coatings on Ti-6Al-4V via laser cladding (DED). They found that under a power of 900 W, a powder feed rate of 0.100 g/s, a beam diameter of 2 mm and laser speeds of 5-11.67 mm/s (energy densities of 39-90 J/mm^2), unmelted Nb particles were remaining. Increasing the power to 1100 W

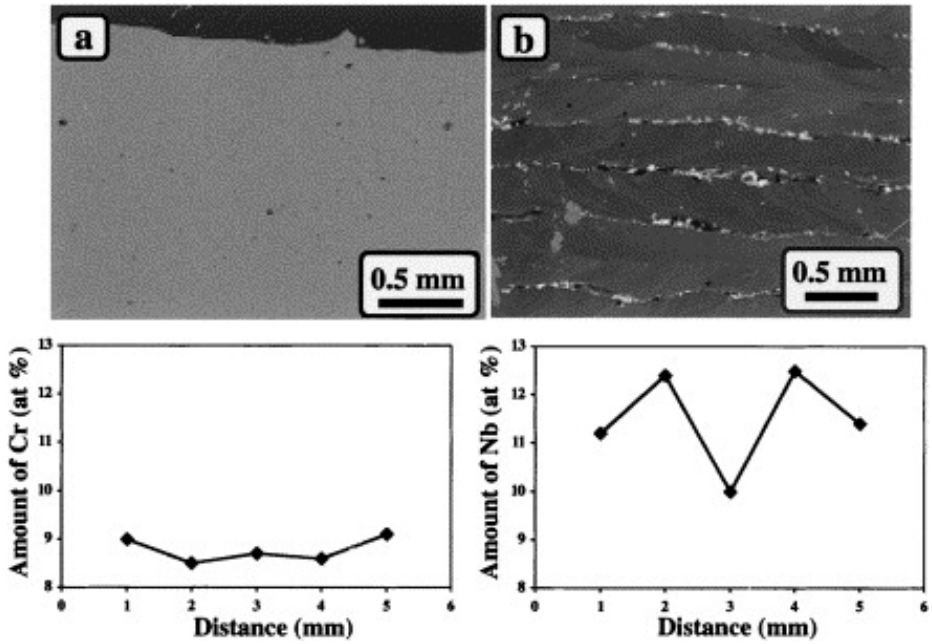

Figure 2.2: SEM image (top) and spatial elemental distribution of alloying element (bottom) of a) (Left) Ti-Cr and b) Ti-Nb printed via DED. Taken from [8].

ensured homogeneity. However, increasing the powder feed rate to 0.133 g/s from the ideal conditions again yielded unmelted Nb particles [34]. Polozov *et al.* observed in the SLM of Ti-6Al-7Nb, and Ti-22Al-25Nb the presence of unmelted Nb. However, in Ti-6Al-7Nb, in regions far from the unmixed Nb, they observed a concentration close to the powder composition; this shows that the sample contained unmixed and mixed regions [32]. Wang *et al.* also studied the influence of varying energy densities in printing NiTi (1:1 atomic ratio). Figure 2.3 shows optical microscopy images of microstructures printed at a low (40 J/mm^3), medium (80 J/mm^3) and high (130 J/mm^3) energy density (left, middle and right, respectively). At a low energy density, they observed the presence of unmelted powder. The diffusion region surrounding the Nb shows that part of the Nb had melted and started to alloy, although insufficiently, with its surroundings. At a high energy density they observed better homogeneity,

but more keyholing defects [9]. Wang *et al.* found in the SLM of Ti-35Nb that there were partially alloyed Nb particles in the microstructure [35]. Polozov *et al.* used X-ray microtomography to observe and analyze a volumetric sample of SLM-printed Ti-22Al-25Nb at an energy density of 55.6 J/mm^3. Their reconstructed volume is shown in Figure 2.4 a). Of interest to this review is the volume of unalloyed Nb, which is shown in Figure 2.4 b). As demonstrated in this subfigure, the unalloyed Nb phase occupied 6% of volume [4]. The above findings in printing Ti-Nb alloys in [4, 35, 32, 34, 9] are due to Nb having a significantly higher melting point (2741 K) over Ti (1941 K). Sing *et al.* printed Ti-50Ta (wt. %) via SLM and found unmelted Ta, although the amount of dissolved Ta increased at higher energy densities, from ∼20% at 16 J/mm^3 to ∼45% at 144 J/mm^3 [36]. Zhao *et al.* printed Ti-6Ta, Ti-12Ta, Ti-18Ta and Ti-25Ta (wt. %) via SLM and found unmelted Ta [37]. The melting point of Ti is significantly lower than that of Ta (3290 K), explaining the presence of unalloyed powders in [36, 37]. Traxel *et al.* found in the printing of Ti-20Zr the presence of unmelted Zr. The melting point of Zr is at 2128 K, which is slightly higher than that of Ti. It is not clear, however, what the uneven alloying can be attributed to [38]. Martinez *et al.* printed Al-12Cu via SLM and found retained, unalloyed Cu [39]. Cu has a higher melting point than Al, at 1358 K and 934 K respectively. Biffi *et al.* printed $TiCr_{1.78}$ from elemental and prealloyed powders as a comparison via SLM and found regions of unalloyed Ti and Cr [40]. Nagase *et al.* studied the SLM of four binary Ti alloys containing 20% Cr, Nb, Mo and Ta (at. %) respectively. They observed that in the printing of Ti-Cr, unmelted Cr particles were visible on the surface at 1.5 J/mm^2, but not at 3 J/mm^2. Weak, unalloyed Mo peaks were also observed in XRD of Ti-Mo, though the conditions at which this

sample was taken were not made clear [41]. Mo and Cr have melting points of 2896 K and 2180 K. The melting point of Cr is similar to that of Ti, which explains why unmelted Cr was only observed at a low energy density. Hanemann *et al.* printed a mixture of alloyed AlSi10Mg and elemental Si via SLM to produce a hypereutectic AlSi alloy. Samples were found to contain unmelted Si particles, as Si has a melting point of 1703 K, compared to the melting point of AlSi10Mg at 887 K [42]. Ewald *et al.* (2019) printed a high-entropy AlCCoFeMnNi alloy via SLM. At the low energy density of 143 J/mm^3, they found regions of Ni, Fe and Co. They did not observe this at a high energy density of 247 J/mm^3. Ni, Fe, and Co have melting points of 1,728 K, 1,811 K and 1,768 K. They are higher than the melting points of Al and Mn, the latter which is 1,519 K. This explains why Ni, Fe and Co did not dissolve sufficiently at 143 J/mm^3 [43]. Schönrath *et al.* found in the printing of Ni-21.5Fe (at. %) that at an energy density of 71 J/mm^3, unmelted Ni powders remained in the bulk due to the higher melting point of Ni [33]. Chen *et al.* printed W-6Ni-2Fe-2Co, W-12Ni-4Fe-4Co and W-18Ni-6Fe-6Co via SLM. Due to the very high melting point of W (3,695 K), unmelted W was observed, surrounded by a W-Ni-Fe-Co phase and intermetallic Fe_7W_6. This demonstrated that the W had partially dissolved [10].

Depending on the system, unalloyed powders may aid or hinder the performance of the alloy. A benefit of unmelted powders is that they may act as a composite component in the alloy. In some systems they may act as a detriment, causing lack-of-fusion defects and porosity due to insufficient coating of particles by the surrounding phase. This is best demonstrated in Chen *et al.*, as shown in Figure 2.5. They observed in the printing of WNiFeCo alloys that at high W concentrations (80-90 wt. %), there was insufficient NiFeCo phase surrounding the W particles, causing

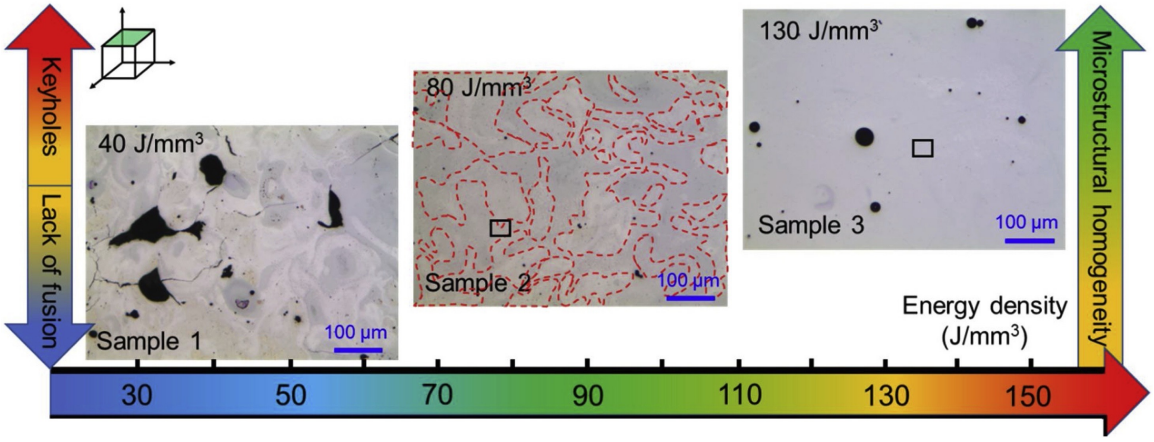

Figure 2.3: Relationship between energy density, the presence of defects and the degree of alloying in NiTi printed via SLM. Taken from [9].

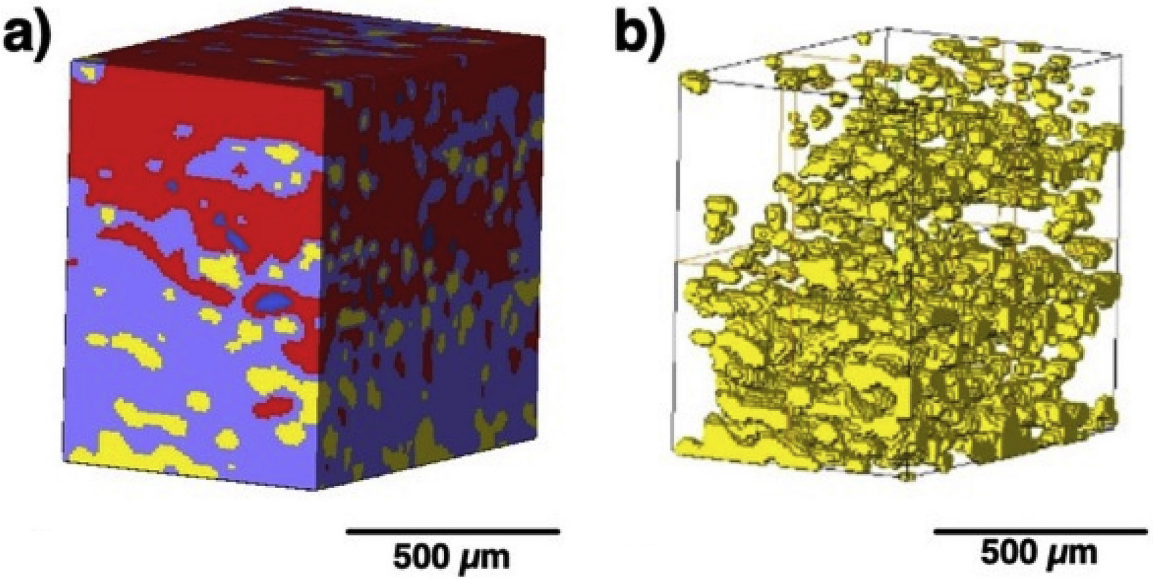

Figure 2.4: a) X-ray tomographic reconstruction of Ti-22Al-25Nb printed via SLM from elemental Ti, Al and Nb. Purple represents the Ti-Nb-Al phase. Red represents the volume without Nb. Yellow represents the unalloyed Nb particles. Blue represents the porosity. b) shows only the unalloyed Nb. Taken from [4].

cracking and porosity (Figure 2.5 a)-d)). However, with 70% W, premature cracking and porosity were avoided (Figure 2.5 e) and f)), and hence it behaved as a composite material [10]. Using a high power can aid in melting and dissolving high-melting-point alloying elements. However, using a high power may lead to keyholing defects, and, as will be discussed in the next section, loss of material through vaporization.

2.2.3 Loss of Material via Vaporization

Even if homogeneity is achieved in the bulk microstructure, the microstructure may not conform to the desired composition. In contrast to insufficient melting and dissolving of high-melting-point components at low energy densities, excessive vaporization of a component with a with a relatively low boiling point or high vapour pressure at high energy densities may lead to loss of a fraction of this component. Polozov *et al.* noticed a decrease in the Al concentration in printing Ti-22Al-25Nb. The Al concentration varied from 16.5% at or below ∼100 J/mm^3 to 12% at 370 J/mm^3 (at. %). This is because the boiling point of Al is at the melting point of Nb at 2,743 and 2,750 K respectively [4]. Wang *et al.* found in the DED of Ni-Ti alloys that at high laser powers with DED, the Ni concentration was lower relative to the Ti concentration, as it has a lower boiling point than Ti (3,005 and 3,560 K respectively) [9]. Chen *et al.* found in the SLM of W-6Ni-2Fe-2Co, W-12Ni-4Fe-4Co and W-18Ni-6Fe-6Co a lower composition of Ni, Fe and Co in each alloy than in the powder. As they have low boiling points relative to the melting point of W, they vaporized during printing [10]. Chen *et al.* printed a high-entropy CoCrFeMnNi alloy via SLM from a pre-alloyed CoCrFeNi and elemental Mn powder. They observed that the Mn concentration decreased from 21% in the powder to 16% in the sample. They attributed this to the

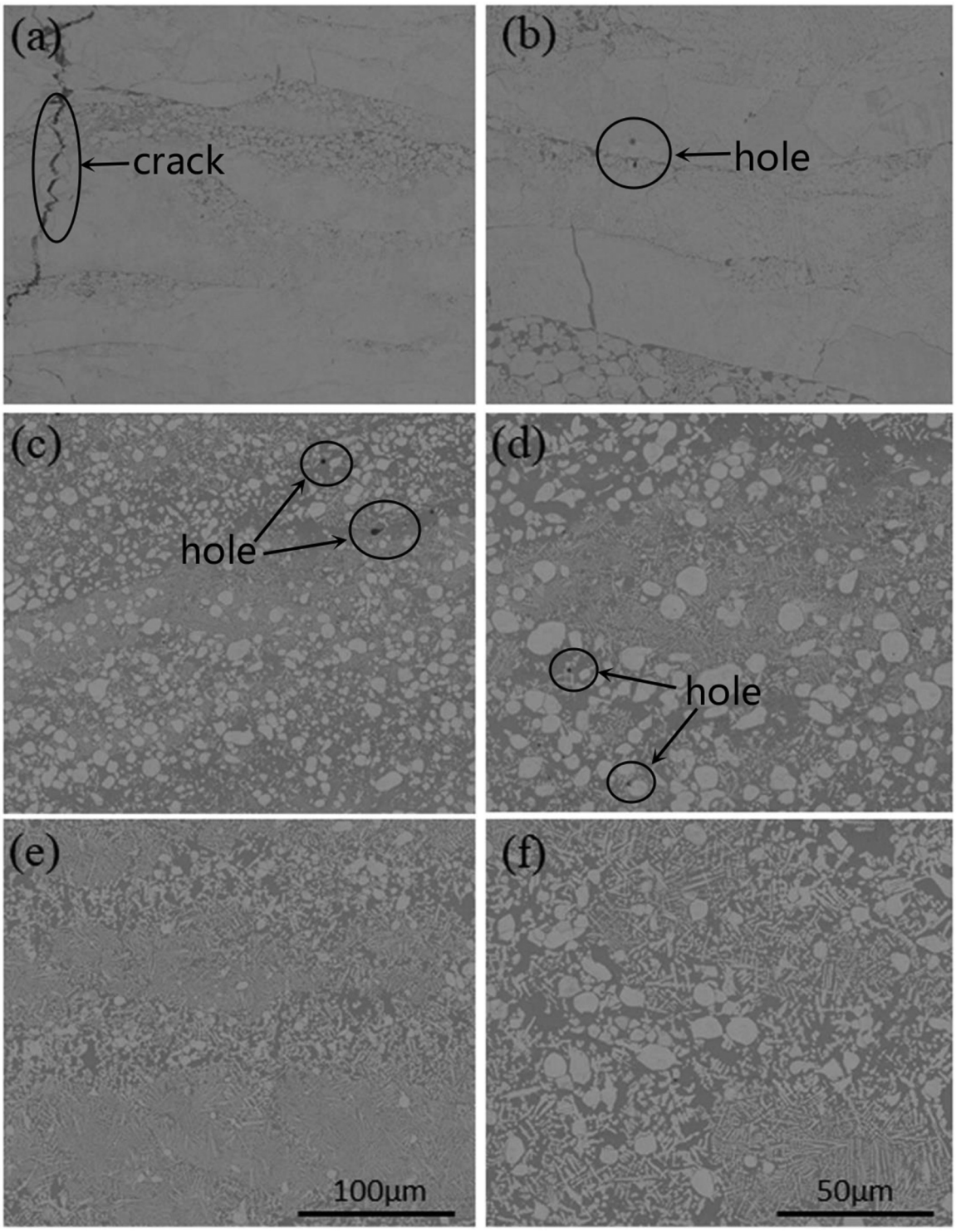

Figure 2.5: Backscatter electron images of a), b) W6Ni2Fe2Co, c), d), W12Ni4Fe4Co and e), f), W18Ni6Fe6Co printed via SLM. The build direction is facing upwards. Taken from [10].

low melting point of Mn (relative to the CoCrFeNi alloy) and the irregularity of the Mn powder, though they did not specify the melting point of the CoCrFeMnNi alloy [7]. Moorehead (2020) *et al.* observed in the printing of high-entropy MoNbTaW alloys via DED that, even with remelting (which will be discussed later), that they observed a lower than desired Mo concentration due to its high vapour pressure [5].

2.3 Surface Microstructure and Melt Pool Behaviour

Though most studies on *in-situ* alloying have focused on the bulk microstructure, only two studies have shown how the surface microstructure appears. They have demonstrated that the surface layer is unalloyed, unlike the bulk microstructure. Grigoriev *et al.* observed on the surface of Ti-22Al-25Nb printed via SLM from elemental powders the presence of insufficiently-dissolved Al and Nb. They were located both between and within melt tracks [31]. Dobbelstein *et al.* printed a single track of high-entropy alloy MoNbTaW from elemental powders on a Mo substrate preheated to 873-973 K. Figure 2.6 shows the SEM and EDX images of the track. They show the presence of unmelted powders sintered to, but not mixed with, the substrate. Though this was performed with substrate preheating, it can be assumed that unmixed, but sintered powders would also remain when printing at room temperature [11].

Insufficient dissolving in the melt pool can be explained through the negligible role of Marangoni convection (mixing induced via surface tension), as shown in the work of Clark *et al.* They used real-time synchrotron X-Ray Radiography (X-ray transmission imaging) to visualise and analyze the behaviour of undissolved W particles in an Al-6061 melt pool during SLM [12]. This combination of parent and tracer powders has been used previously by Guo *et al.* They chose Al-6061 as the parent powder for its

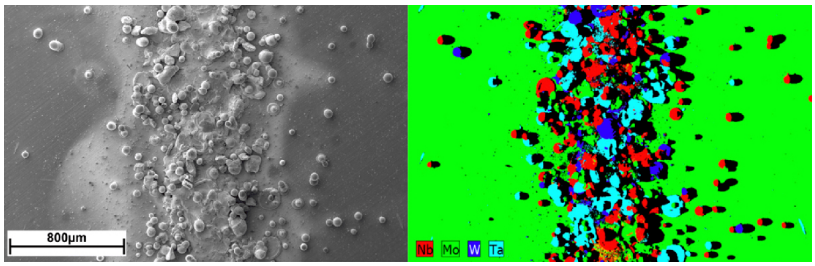

Figure 2.6: (Left) Secondary electron and (Right) EDX images showing a single layer of MoNbTaW printed via DED on a Mo substrate. Adapted from [11].

high X-ray transparency and low melting point. They chose W as a tracer particle due to its high opaqueness to X-rays and extremely high melting point, allowing one to visualize the flow of W particles in molten Al without losing W to melting or diffusion in the melt pool [44]. Clark *et al.* observed the trajectories of individual particles, the traces of which are shown in Figure 2.7. As shown in Figure 2.7, particles melt pool travel on the same order of magnitude as the laser beam itself. With the extremely low time the melt pool spends molten, powders may complete only one convective current cycle before solidification. As a result, Marangoni flow plays a small role in particle dissolution in *in-situ* alloying [12]. Rather, alloying is incomplete at the surface because the time powders spend at high temperatures is insufficient to complete their dissolution.

2.4 The Gradient between the Surface and Bulk Microstructure

As implied through Section 2.2 and 2.3, there is a gradient between the unalloyed surface and an alloyed microstructure. However, this gradient has only been investigated superficially. The work of Yan *et al.* is shown in Figure 2.8. They studied

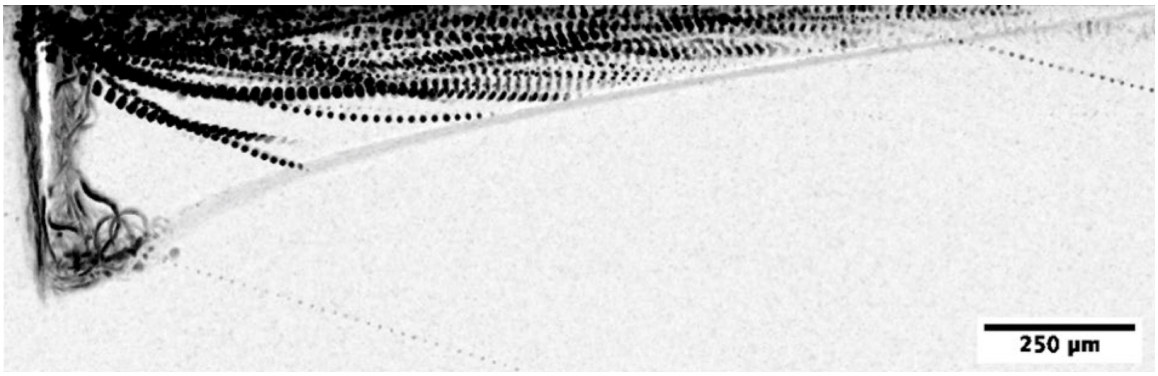

Figure 2.7: (Left) Trajectories of tungsten particles in an Al-6061 melt pool during SLM. Taken from [12].

the DED of a single wall (single-hatch, multiple layers) of Ti-6Al-4V. They observed a microstructural gradient along the build direction, as demonstrated in Figure 2.8. Figure 2.8 a) shows the concentration as a function of the build direction. Yan *et al.* attributed the decrease in Al and V concentration to the decrease in heat conduction with increasing layer built. The thin layer thicknesses of the wall hindered heat conduction. Hence, closer ot the surface, more Al and V evaporated. Micrographs of a top, middle and bottom section of the wall (Figure 2.8 b)-d) respectively) demonstrated a coarser grain size with increasing build height. This was attributed to the increase in cooling rate. However they never elaborated upon which were the top and bottom parts [13]. Kang *et al.* printed a single wall of Ti-Mo and observed the resulting gradient structure between top and bottom sections. As shown in Figure 2.9, they observed unmelted Mo in the top section (Fig. 2.9 a)-c)), but no unmelted Mo in the bottom section (Fig. 2.9 d)-f)). This demonstrated a gradient structure resulting from successive intrinsic heat cycles in which alloying slowly occurred over a series of steps. However, they did not elaborate on the distance between the top and bottom sections to the topmost surface, preventing a clear understanding of how

alloying occurred in the heat-affected zone [14].

2.5 Strategies to Improve Homogeneity

Remelting

One strategy that has been tested to improve homogeneity is remelting each layer after printing it to homogenize it. Remelting was first tried by Dobbelstein *et al.* in the printing of a single track of a high-entropy MoNbTaW alloy on a Mo substrate with preheating temperatures of 873-973 K. Figure 2.10 shows the SEM and EDX images of printing a) (previously shown in Fig. 2.6) without and b) with remelting. Without remelting, the track was covered in unalloyed particles. With remelting, however, a smooth, homogeneous track with few unalloyed particles was produced [11]. Brodie *et al.* observed the microstructures of Ti-25Ta (wt. %) alloy printed via SLM with and without remelting at various scanning speeds. As shown in the graph in Figure 2.11 a) the percentage of partially-melted Ta decreased after remelting, especially at high scanning speeds. Figure 2.11 b) and c) show the micrographs of the microstructure printed at 300 mm/s with and without remelting, repectively. It shows a decrease in the in the number of particles from b) to c) [15]. Lin *et al.* found, in the SLM of a FeCoCrNi high-entropy alloy, an even distribution of alloying elements at the surface with remelting compared to without remelting [45]. Dobbelstein *et al.* (2018), Dobbelstein *et al.* (2019) and Moorehead *et al.* also remelted each layer before depositing a new one upon it in the printing of TiZrNbHfTa, functionally-graded TiZrNbTa, and MoNbTaW high-entropy alloys respectively, also demonstrating that a homogenous microstructure can be achieved with remelting [46, 47, 5].

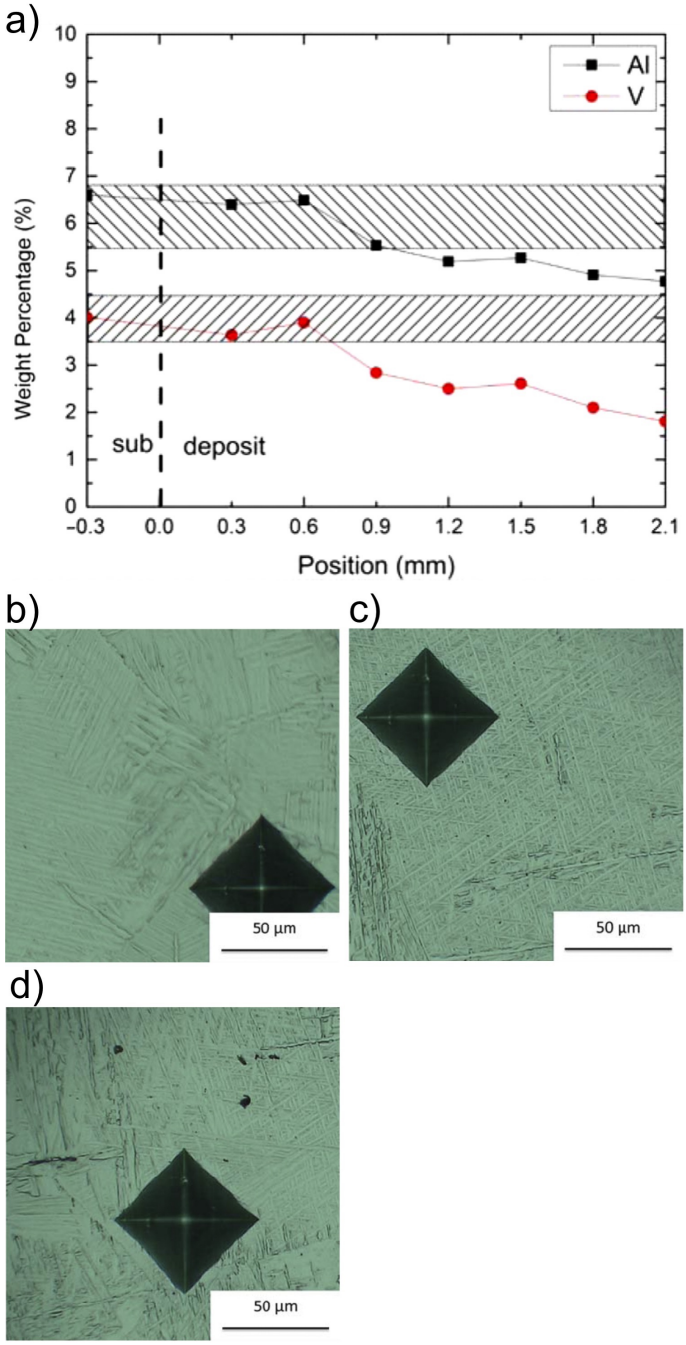

Figure 2.8: a) Composition of Al and V in a Ti-6Al-4V single wall printed via SLM along the build direction from the substrate (-0.3 mm) to the surface (2.1 mm). b)-d) Microstructure at the top, middle and bottom of the sample respectively. Taken from [13].

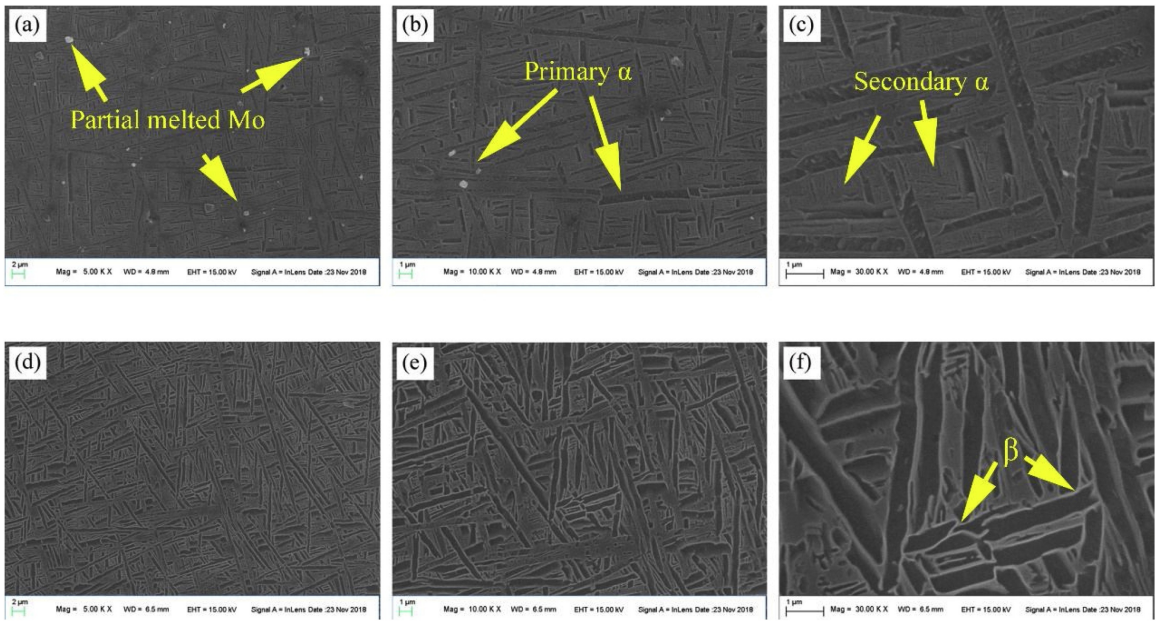

Figure 2.9: Microstructure at the a) top and b) bottom of a single wall of Ti-Mo printed via DED. Taken from [14].

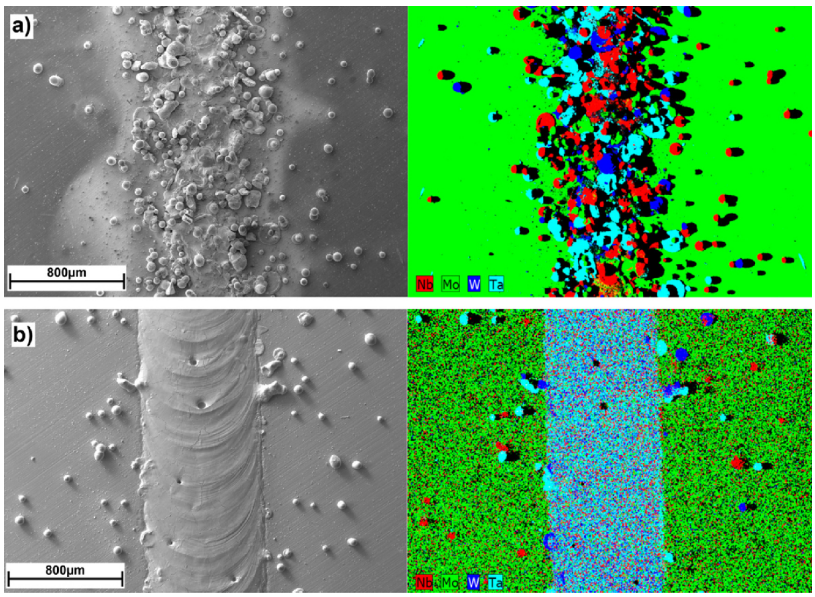

Figure 2.10: (Left) Secondary electron and (Right) EDX images of a MoNbTaW layer printed via DED on a Mo substrate a) without and b) with remelting. a) was previously shown in 2.6. Taken from [11].

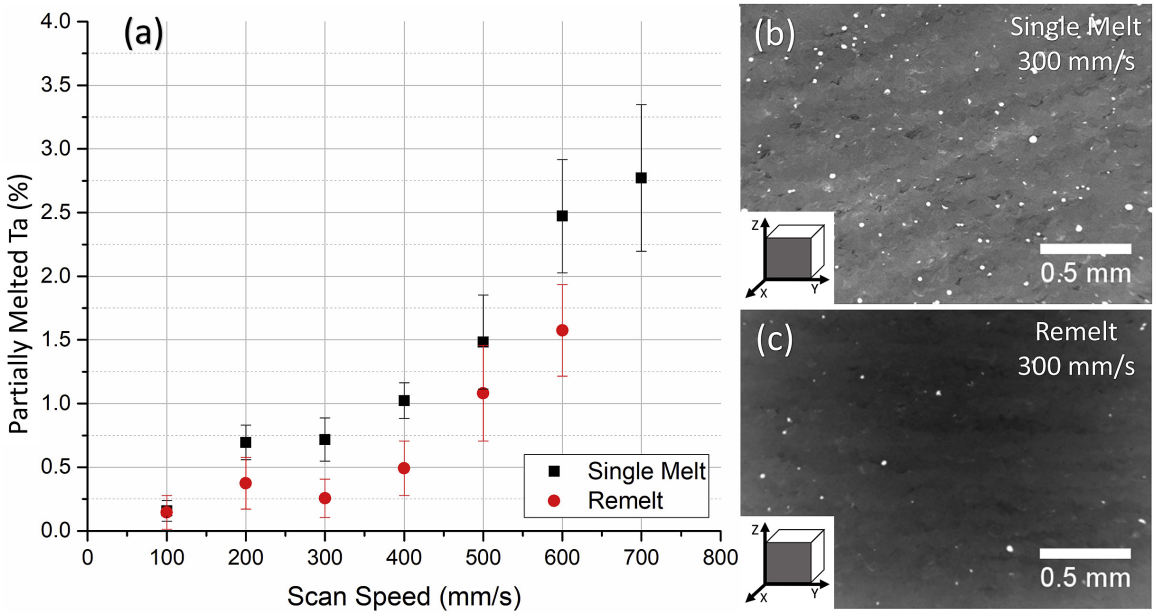

Figure 2.11: a) Difference in composition at different scan speeds in the SLM of TiTa with and without remelting. b), c) Microstructure without and with remelting respectively. Taken from [15].

However, compositional issues in printing different elemental powders remain with remelting. For example, Dobbelstein *et al.* found in printing a MoNbTaW high-entropy alloy with preheating to 873-973 K and remelting that less Mo than was in the powder was retained [11]. Moorehead *et al.* printed MoNbTaW high-entropy alloys with a single remelting step via DED. Initially, they set nozzle flow rates proportional to the desired compositions. As shown in Figure 2.12, the resulting alloys had less Mo and higher Nb and W than desired due to the high vapour pressure of Mo. However, they were able to alter nozzle flow rates based on their initial results to yield Mo and W concentrations within ± 10% of the desired composition and the Ta and Nb concentrations within ±5% of the desired composition [5]. Dobbelstein *et al.* also modified the powder composition from equiatomic to $Ti_{14.1}Zr_{16.3}Nb_{19.8}Hf_{19.7}Ta_{30.1}$ (at. %) to yield an equiatomic TiZrNbHfTa high-entropy alloy [47].

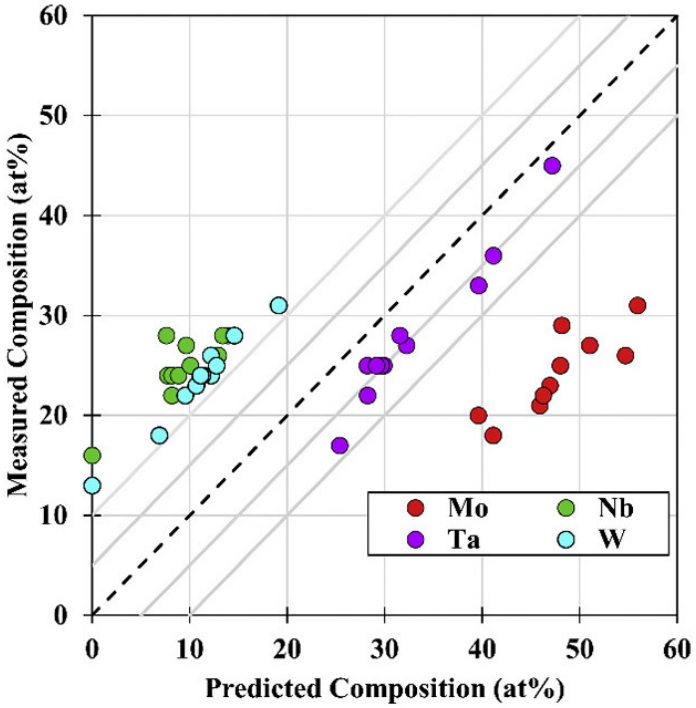

Figure 2.12: Comparison between expected and actual compositions in the DED of MoNbTaW high-entropy alloys, where nozzle speeds were directly proportional to the desired concentration. Taken from [5].

Increasing the Build Temperature

Another method to improve homogeneity is preheating the substrate and holding it at this temperature during printing. For example, Dobbelstein *et al.* found in the DED of a MoNbTaW high-entropy alloy that preheating at 923 K instead of 773 K improved the homogeneity near the base of a single wall slightly [11]. However, normal additively manufactured objects take hours to print; this time may be sufficient to induce phase transformations in the substrate and the originally printed material. Furthermore, Dobbelstein *et al.* noticed that the single wall preheated to 923 K was slanted and had less dimensional accuracy; this may also be an influencing factor in using a low or no preheating temperature[11].

Satelliting

One other method that may improve homogeneity is satelliting, or adhering fine minority powder particles to the coarse parent element particles. Simonelli *et al.* tested this technique in printing Ti-6Al-4V, and compared it to pre-alloyed powders, a simply-mixed mixture with coarse Ti, Al and V powders (Simply Mixed 1), and a simply-mixed mixture with coarse Ti and fine Al and V powders (Simply Mixed 2). BSE and EDX images of Simply Mixed 1, Simply Mixed 2 and the satellited-powder-printed microstructures are shown in Figures 2.13, 2.14 and 2.15 respectively. As is shown in Fig. 2.14 a) and b) and Fig. 2.13 a), b), e) and g), comparing Simply Mixed 2 to Simply Mixed 1, they found lower porosity. As is shown in 2.14 c) and d) and 2.13 c), d), f) and h), there was less elemental segregation in Simply Mixed 2 than Simply Mixed 1 and hence more homogeneity. They attributed this to the lesser packing of particles, and hence, less ability of the powder mixture to absorb and melt from the laser energy. With regards to the material printed from satellited powder, as shown in Fig. 2.15, they also found lower porosity than with Simply Mixed 2 (Fig. 2.14). They found a more homogeneous microstructure (Fig. 2.15 c) and d)) than Simply Mixed 2 (Fig. 2.14 c) and d)), although they still found some elemental inhomogeneity. They attributed this to Al and V particles which did not successfully bind to Ti particles[16].

2.6 Conclusion

In conclusion, this review has summarized and outlined the current work to date on the use of elemental feedstocks in laser AM. They have shown the following:

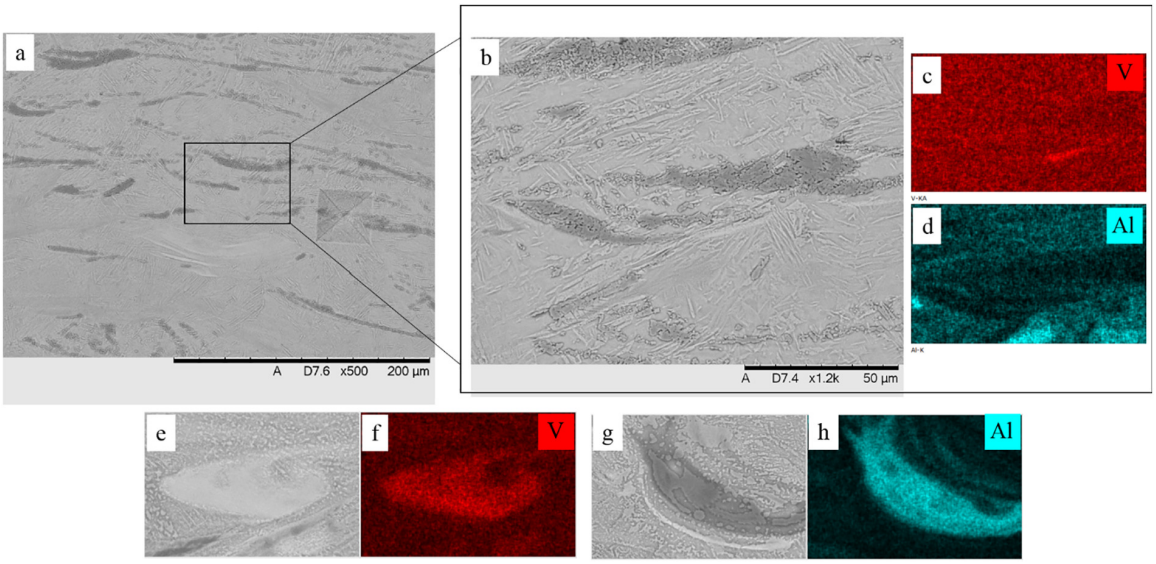

Figure 2.13: a), b), e) and g) Microstructure and c), d), f and h) EDX images of the microstructure printed via SLM through the powder set Simply Mixed 1 (Coarse Ti, Al and V powders). Taken from [16].

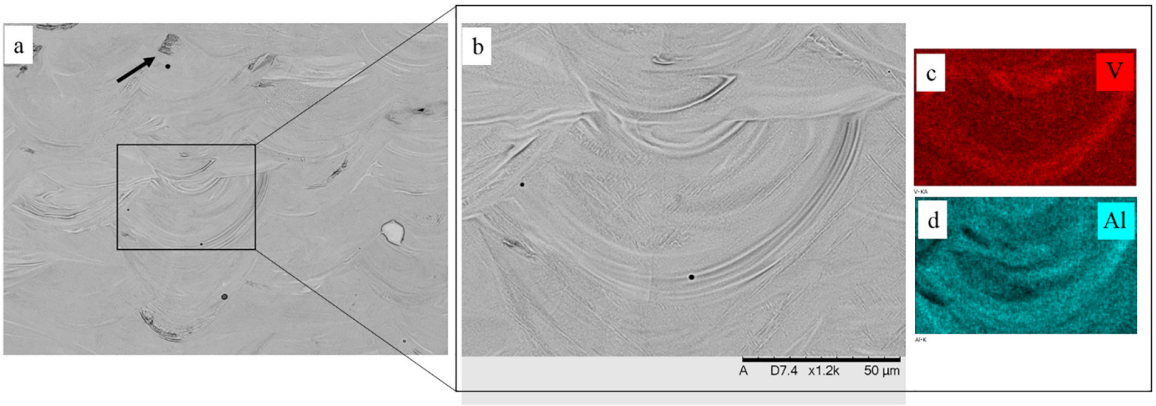

Figure 2.14: a), b) Microstructure and c), d) EDX images of the microstructure printed via SLM through the powder set Simply Mixed 2 (Coarse Ti, fine Al and V powders). The arrow points to a region high in Ti along a melt pool striation. Taken from [16].

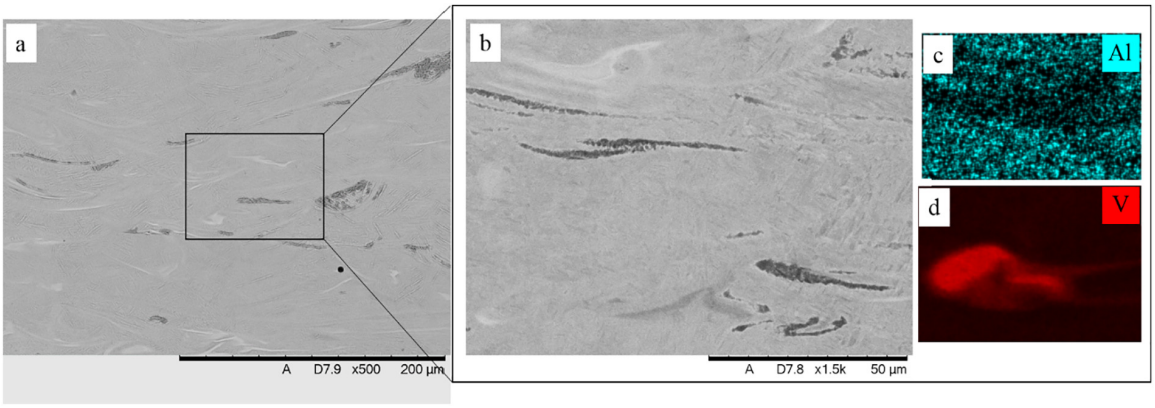

Figure 2.15: a), b) Microstructure and c), d) EDX images of the microstructure printed via SLM through the satellited powder mixture. Taken from [16].

1. Though alloying is not achieved at the surface, a layer can undergo multiple intrinsic heat treatments to be successfully alloyed. There is a gradient between the unalloyed surface and the alloyed bulk microstructure, however, not much is known about this gradient.

2. Different factors influence homogenization. An exothermic mixing enthalpy aids alloying, while an endothermic mixing enthalpy hinders it. Additionally, using powders with a high difference in melting or boiling point may lead to high-melting-point elements dissolving insufficiently and low-boiling-point elements vaporizing.

3. Techniques to improve alloying such as remelting, preheating and satelliting have been tested to improve alloying, and can be used in the implementation of elemental powders in commercial uses of laser AM.

Chapter 3

Scope and Objectives

3.1 Scope

3.1.1 The need to understand homogeneity during *in-situ* alloying

The only studies showing how homogeneity develops either focus on the need for remelting, or are vague about the development of an alloyed microstructure. While some show the comparison in printing a single layer between not using and using remelting, they do not explain in detail how the effect of multiple heat treatments creates an alloyed structure. We need a fundamental understanding in which it is clear how homogeneity develops from a single layer. This is important to understand how to improve this microstructure. A detailed mictrostructural analysis on the wall can, unlike the work of Yan et al. [13] and Kang et al. [14], identify the phases present at each depth via EBSD, and correlate them back to the elemental distribution via EDX.

3.1.2 The case for sXRD

Synchrotron X-ray diffraction (sXRD) gives the opportunity to identify the phase transformations during printing [18]. (This is termed an *in-situ* or operando technique. For the sake of not confusing sXRD with *in-situ* alloying, the term *in-situ* will not be included when discussing this technique.) Using a customized laser AM chamber compatible with a beamline, a thorough-transmission, high-energy X-ray beam (energies on the range of 10-100 keV [48, 17]), diffract through the powder, melt pool and printed layers [49, 48, 50, 51, 17, 18]. Figure 3.1 a) shows a diagram of the sXRD process when performed with DED. This diagram shows a single wall (single-hatch, multiple layers) being printed upon a substrate concurrently to sXRD of the sample. Figure 3.1 b) shows the completed wall in the customized laser AM replicator. This figure was taken from Epp et al. [17], whose work will be discussed further below. Diffraction patterns can be collected at frequencies of up to 20 kHz. The phase transformation sequence during printing may then be determined [18]. An example of the data that can be obtained from sXRD is shown in Figure 3.2. Figure 3.2 a) shows 2D patterns at various points in the printing process. The colourmap in Figure 3.2 b) shows the diffraction intensities as they vary with respect to time. Figure 3.2 c) shows the intensity variation of two peaks with respect to time. This figure was taken from Zhao et al. [18], whose work will be discussed below.

Since 2017, several studies have investigated phase transformations in laser AM with sXRD. For example, Zhao et al. investigated the SLM of Ti-6Al-4V. By studying the changes in peak intensity during printing, they found that the post-melting phase transformation of β (high-temperature-stable phase) to α (low-temperature-stable phase) took $\sim$ 10 ms, confirming that it produced martensitic α (α') [18]. Calta

et al. also printed Ti-6Al-4V via SLM, using a frame rate of 1 kHz and a beam cross-section of 100 x 500 µm. They observed lattice parameter shrinkage during cooling. They found that the β microstructure which formed at solidification was fully converted to α [50]. Epp et al. performed DED during sXRD with a frame rate of 10 Hz to track the phase transformations in the steel X40CrMoV5-1. They observed melting and the formation of martensite (α'), with little remaining austenite (γ), in the first layer. By tracking a layer as it underwent multiple reheating cycles, they were able to determine the extent of the melted zone, and the amount of α' and γ remaining in the heat-affected-zone. Assuming that the contribution of stress to the lattice parameter was negligible, they used the lattice parameters of α' to estimate its carbon content during reheating cycles [17]. Hocine et al. used a miniaturized SLM device, which they termed MiniSLM [49]. This device is compatible with a beamline, and can print multi-track parts that can transmit or reflect X-rays. Using a frame rate of 20 kHz, they also observed the phase transformations in the printing of Ti-6Al-4V, and demonstrated the role of the scanning strategy on the resulting phase transformations. They found that lower cooling rates resulted from a shorter scanning vector [48]. Calta et al. used sXRD to study the phase transformations in Ti-64 and Ti-5553. They used a large X-ray beam of cross-section dimensions 300x50 µm and a frame rate of 1 kHz. With the sufficient powder statistics, they were able to deconvolute each peak to a contribution from the melted and heat-affected-zones, hence demonstrating the phase transformations in both zones [51].

Current studies on *in-situ* alloying have used electron microscopy and X-ray tomography to examine the microstructure post-mortem (after printing) to understand the extent of alloying. While this is crucial to understanding the microstructural

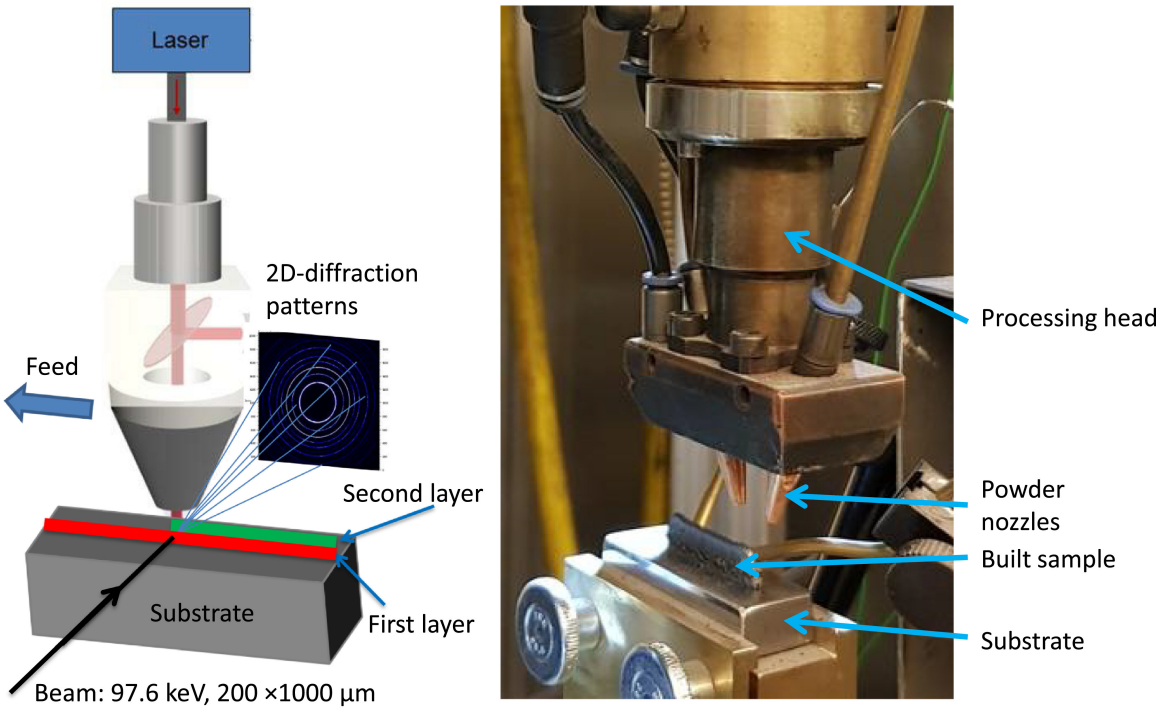

Figure 3.1: a) (Left) Diagram of sXRD with DED. b) (Right) A customized beamline-compatible DED replicator. Taken from [17].

development and hence the alloying, it is also important to examine the development during the process. Only one real-time study has been performed on *in-situ* alloying to date. This study by Clark et al., cited earlier in Section 2: Literature review, used synchrotron X-Ray Radiography (X-ray transmission). As was explained in further detail in Chapter 2: Literature Review, this study determined that unmelted particle velocities are on the order of 0.5-1 m/s, preventing sufficient mixing in the melted zone [12]. No studies have been performed on *in-situ* alloying using sXRD. The phase transformation sequence found via sXRD can be related to the microstructural development and hence the alloying process, giving insight into how the alloyed microstructure develops.

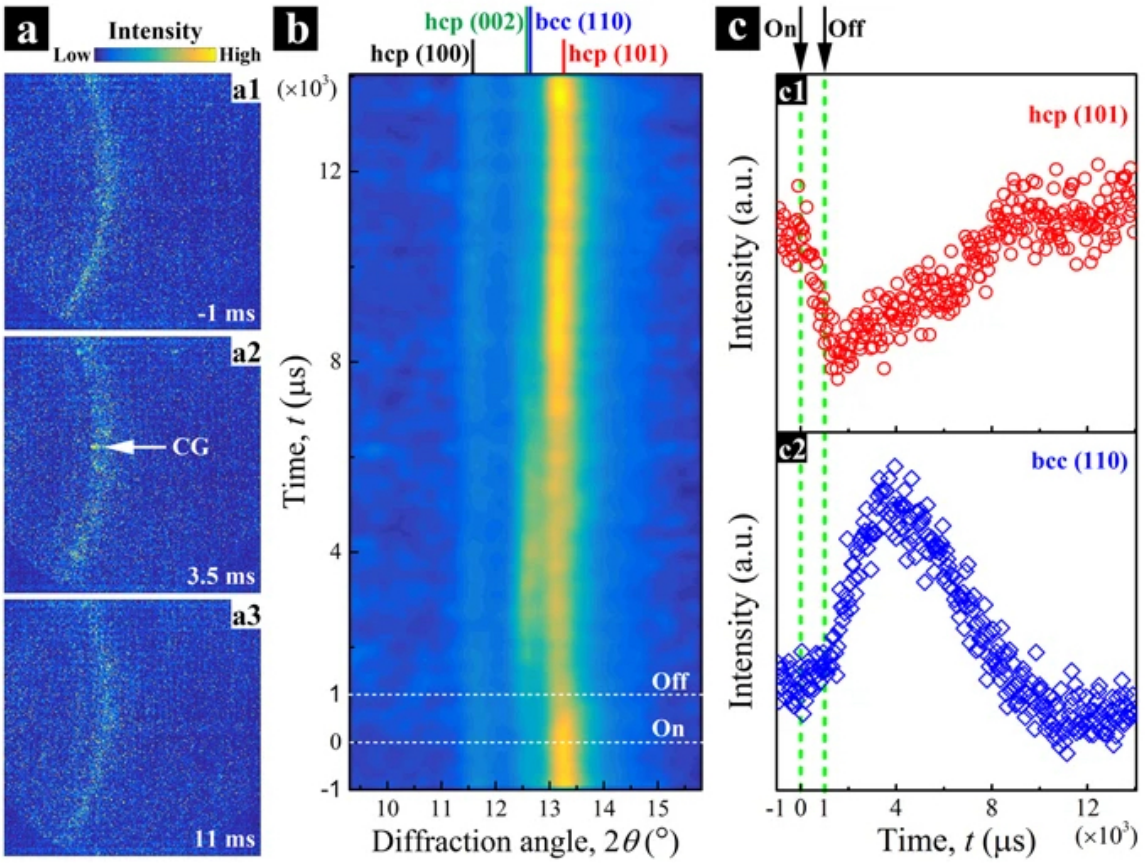

Figure 3.2: a) A sample of three 2D sXRD images at -1 (a1), 3.5 (a2) and 11 (a3) ms with respect to the arrival of the laser at the acquisition volume (0 ms) during the SLM of Ti-6Al-4V. A diffraction spot corresponding to a coarse grain is shown at 3.5 ms (a2). b) A 1D series of diffraction acquisition patterns with respect to time. Colour represents the intensity of peaks, demonstrating phase transformations. c) Evolution of the α-{101} and β-{110} peaks with respect to time. Taken from [18].

3.1.3 Ti-185 as a Model System

A model system is required to perform a sXRD and post-mortem microscopy analysis. Ti-1Al-8V-5Fe (Ti-185) was chosen as an example system with which to investigate the alloying process. Ti-185 is a β-Ti alloy (BCC) [52]. At equilibrium in pure Ti, β-Ti is stable at high temperatures, while α-Ti (HCP) is stable at low temperatures. The β-transus temperature in pure Ti is 1158 K, however, adding α- or β-stabilizers can increase or decrease this point respectively. α-stabilizers include Al and O, while β-stabilizers include Mo, V, Fe, Cr and Cu. Figure 3.3 shows a pseudo-binary phase diagram of generic Ti alloys as a function of β-stabilizer concentration [53].

β-Ti alloys are useful in the aerospace industry for their high strength and ductility over α alloys or $\alpha+\beta$ alloys. For example, Ti-10V-2Fe-3Al (Ti-10-2-3) is used in the landing gear of the Boeing 777. Ti-15Mo-3Al-3Nb-0.2Si (Beta-21S) is used in the Rolls-Royce Trent 400 engine of the Airbus A340 and the Boeing 777. Ti-5Al-5Mo-5V-3Cr (Ti-5553) is used in the airframe and landing gear of the Boeing 787 [54]. However, they are also very expensive due to their alloying with Mo, an expensive β-stabilizer. Fe is a lower-cost alternative to Mo. However, it is not commonly used, or used in low amounts, due to its tendency to segregate during casting to form β-flecks, or solute-enriched β precipitates, which embrittle them [55]. However, as demonstrated in our group's previous research on the SLM of Ti-185 from elemental powders, the rapid cooling rates in SLM can prevent the formation of β-flecks, as shown in the microstructure displayed in 3.4 a) and b). Additionally, a high compressive strength and formability can be obtained [20].

The Ti-185 system is ideal to use to study the development of a homogenous microstructure for two reasons. First, it has been demonstrated to achieve homogeneity

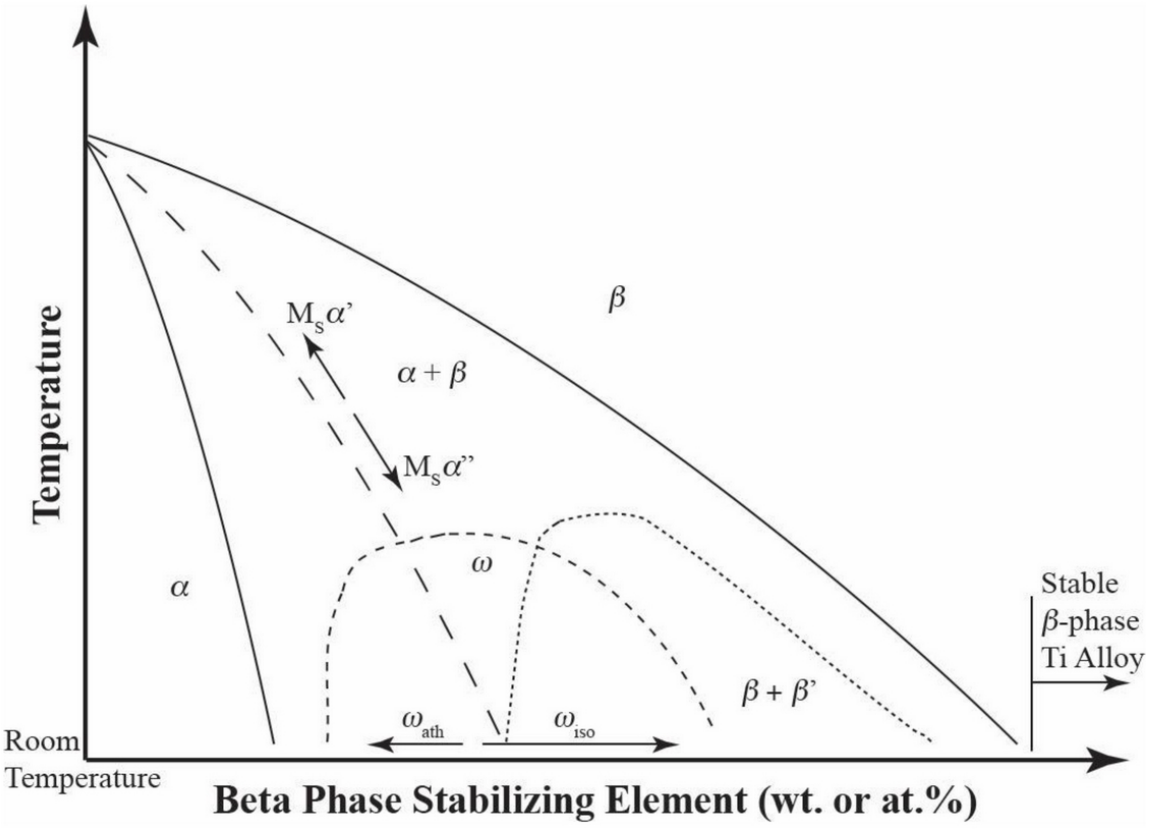

Figure 3.3: Psuedo-binary Ti phase diagram as a function of increasing β-stabilizer concentration. Taken from [19].

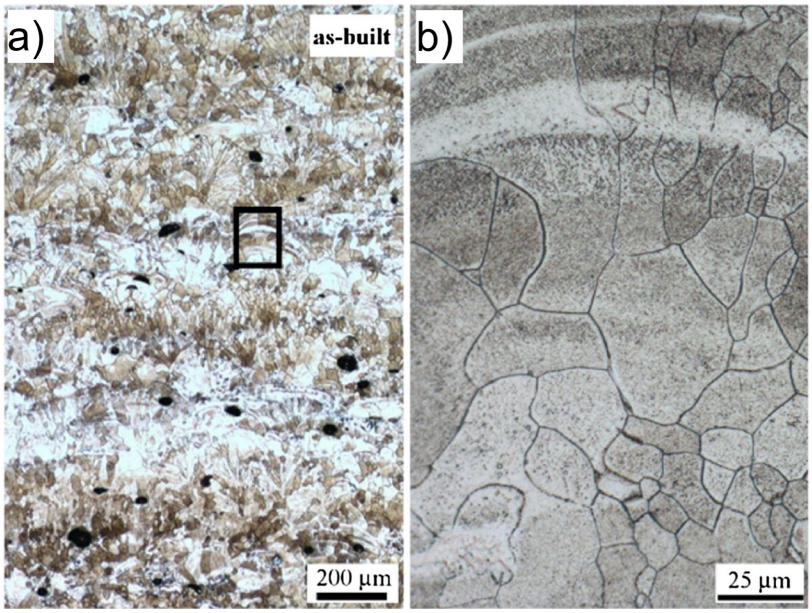

Figure 3.4: a) Optical micrograph of the microstructure of Ti-185 printed via SLM from elemental powders. b) is a high-resolution close-up of the box specified in a). Taken from [20].

in SLM [20]. Second, it was printed from Ti, Fe and AlV powders, which have melting points of 1941 K, 1811 K and 2183 K [56] respectively. The similarity of the melting points can prevent the over-vaporization of a constituent. Third, comparison is facilitated with our previous research on Ti-185. Hence, this is an excellent system to study how alloying develops over the course of multiple layers. Though the phase transformations are specific to β-Ti alloys, the phases which precipitate upon printing are dependent on the degree of alloying in the system. Therefore, the phase transformations in Ti-185 can be used to understand the concept of homogeneity in in-situ alloying in general.

3.2 Objectives

The overarching goal of this project is to understand how an alloyed microstructure develops in laser additive manufacturing from elemental powders. Using the system of Ti-185 from elemental powders as an example, and to serve a comparison to our group's previous work on Ti-185, this project aimed to accomplish its goal via the following objectives:

1. Identify the phase transformations, their time to completion and their respective temperature changes that occur in the melt pool and the heat-affected zone in Ti-185 as it is printed from elemental powders.

2. Relate the microstructural development to the elemental distribution in the melted and heat-affected zones to understand the alloying process.

This thesis will accomplish the goals using the following steps, which will be described in further detail in Chapter 4: Methods, and their results shown and discussed in Chapter 5: Results and Discussion:

1. Identify the phase transformation sequence and time to completion in Ti-185.

2. Identify the temperature changes during the laser additive manufacturing.

3. Identify the phase distributions in the melted and heat-affected zones.

4. Determine the relationship between microstructural development and degree of alloying.

This thesis will not focus on mechanical or corrosive properties in Ti-185 or other materials printed from elemental powders, as they are outside the scope of this work.

However, they will be occasionally commented upon as ultimately, it is desired to print engineering parts with elemental powders for a range of applications. If one wants to understand the mechanical properties of Ti-185 printed from elemental powders, they are referred to the work by Azizi et al [20]. Further exploration of the performance of in-situ-alloyed microstructures may occur in the future.

Chapter 4

Methods

4.1 Introduction

The purpose of this chapter is to explain the experimental and analytical methods used to achieve the objectives described in the previous section. First, it is explained how SLM was used to build the single Ti-185 wall concurrently with performing sXRD and IR imaging to track the phase transformations and temperature changes in the melt pool respectively. It is then explained how the two-dimensional Rosenthal solution was employed to predict the below-surface temperature. Sample preparation and the post-mortem electron microscopy techniques are then explained.

4.2 Materials

To ensure adequate comparison with our group's previous work on Ti-185, the same powder batch used in it (see [20]) was utilized. This elemental powder mixture contained Ti, Fe and an alloyed AlV powder. An alloyed AlV powder was used instead

of individual Al and V powders to prevent the issue seen in other studies in the literature (see Section 2.2.3: Loss of Material via Vaporization) in which low-melting-point elements evaporated in great proportions. Ti, Fe and V have melting points of 1,941 K, 1,811 K and 2,093 K respectively. On the other hand, Al has a melting point of 934 K, and a boiling point of 2,743 K. The temperatures required to melt Ti, Fe and V would vaporize significant amounts of Al. Hence, Al was alloyed with V to have a melting point of 2,183 K [56].

The powder mixture was sourced from ADMA Advanced Materials Products Inc. The powder was mixed via ball milling, and sieved to ensure the desired powder sizes. As a result of the ball milling, they were irregularly shaped (Figure 4.1 a)) and hence had zero flowability. X-ray diffraction verified that only α-Ti (the HCP phase, stable in pure Ti [52]), Fe and AlV were present in the mixture (Figure 4.1 b)). The powder had a size distribution of $d_{10\%}$=21 µm, $d_{50\%}$=51 µm and $d_{90\%}$=68 µm, and an apparent density of 3.1 g/cm^3 [20]. The size distribution is shown in Figure 4.1 c). Using ThermoCalc^{TM}, it was found that the β-transus, solidus and liquidus of Ti-185 are 970.68 K, 1703.45 K and 1848.86 K respectively. ThermoCalc^{TM} was also employed to determine the mixing enthalpies of Ti-1.1Al, Ti-5.5Fe, Ti-8.5V (the concentrations of Ti-185 if other alloying elements were excluded) and Ti-185 with respect to their constituent elements.

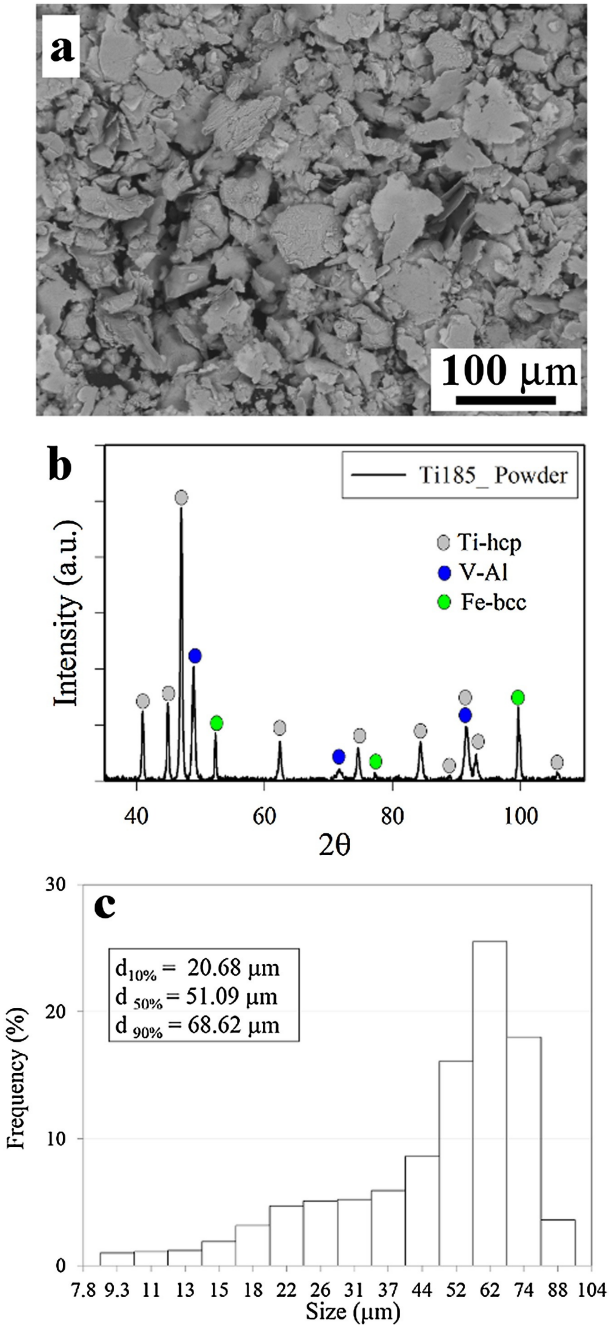

Figure 4.1: a) Secondary electron image of the elemental Ti, Fe and AlV powder mixture used in this study. b) XRD of powder. c) Powder size distribution. Taken from [20].

4.3 Real-Time sXRD and IR Experiments

4.3.1 sXRD

sXRD was performed at the European Synchrotron Radiation Facility on Beamline ID31. Laser printing was performed concurrently to sXRD using the In-situ and Operando Process Replicator (ISOPR). The ISOPR has previously been used successfully to perform SLM and DED concurrently with synchrotron X-ray imaging [57, 58, 59, 60]. Figure 4.2 shows the ISOPR. Figure 4.3 shows a diagram of the process within the ISOPR. A commercially pure Ti substrate of thickness 300 µm, width 4.5 cm and height 1.7 cm was sandwiched between two panels of glassy carbon, each 500 µm thick (not pictured). Because glassy carbon is transparent to X-rays, the panels supported the powder without interfering in the experiments. A hopper deposited a 25 µm-thick layer onto the substrate. A 200 W laser travelling at 400 mm/s with a focus diameter of 50 µm printed a 3 cm-long track. The platform holding the substrate shifted downward and the platform holding the powder shifted upwards, both by 25 µm (one layer height). The hopper deposited another layer upon the previous layer, and the process was repeated. In total, 14 layers were printed. Concurrently to printing, an X-ray beam with cross-section dimensions 20 x 50 µm and wavelength λ=1.812 Å was diffracted through the powder and printed layers. The diffraction patterns were collected by a Dectric Pilatus3 X CdTe 2M detector recording 2D .cbf frames at 250 Hz. The frames were integrated to 1D diffraction patterns, which were processed and plotted in MATLAB. The MATLAB scripts to collect the diffraction frames can be found in Appendix A. The printed sample is shown in Figure 4.4 a), with a close-up of the printed layers shown in 4.4 b).

Figure 4.5 shows the positioning of the X-ray beam with respect to the powder and printed layers. The X-ray beam was positioned 40 µm below the top of the powder layer. If layers were consistently 25 µm-thick, the X-ray beam would have diffracted through the printed layer directly below the powder layer. As a result of powder denudation and shrinkage during melting, printed layers were below 25 µm in thickness. Hence, the X-ray beam overlapped the powder layer. This setup was utilised for 10 laser passes (Figure 4.5, top left). In the next 4 laser passes, the laser beam was shifted downwards by 25 µm each (one platform height differential) to track a layer as it underwent subsequent laser heating cycles (Figure 4.5, top middle and right, bottom left and right). As will be shown in Section 5.2.3: Microscopy, the laser beam had a melt pool diameter of below 300 µm and hence, it did not melt all the powder. The X-ray beam still diffracted through the unmelted powder, as shown in Figure 4.6.

4.3.2 IR Imaging

Concurrently to printing and sXRD, IR imaging was also performed. A Hamamatsu ORCA-Flash4.0 V3 Digital CMOS camera was mounted in the ISOPR (Figure 4.3). The camera had a pixel size of 6.3 µm. It had a field of view of 2048 x 2048 pixels, or 13.312 x 13.312 mm. To increase its frame rate, it was operated in Region of Interest Mode. The resulting field of view was 2048 x 128 pixels, or 13.312 x 0.832 mm. (It is pictured in Figure 4.3 as a rectangular detector for simplicity, however is shown accurately in Figure 4.2). The detector was mounted at 43° to the substrate surface. It was operated at 1603.5 Hz.

The IR images were converted to temperature plots in MATLAB. The scripts

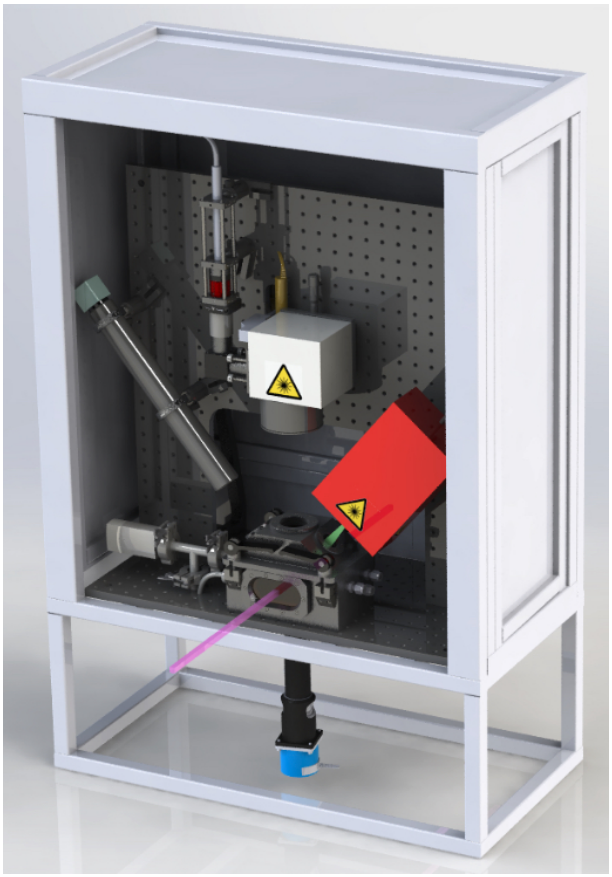

Figure 4.2: Setup of the ISOPR. Image provided by Samuel Clark.

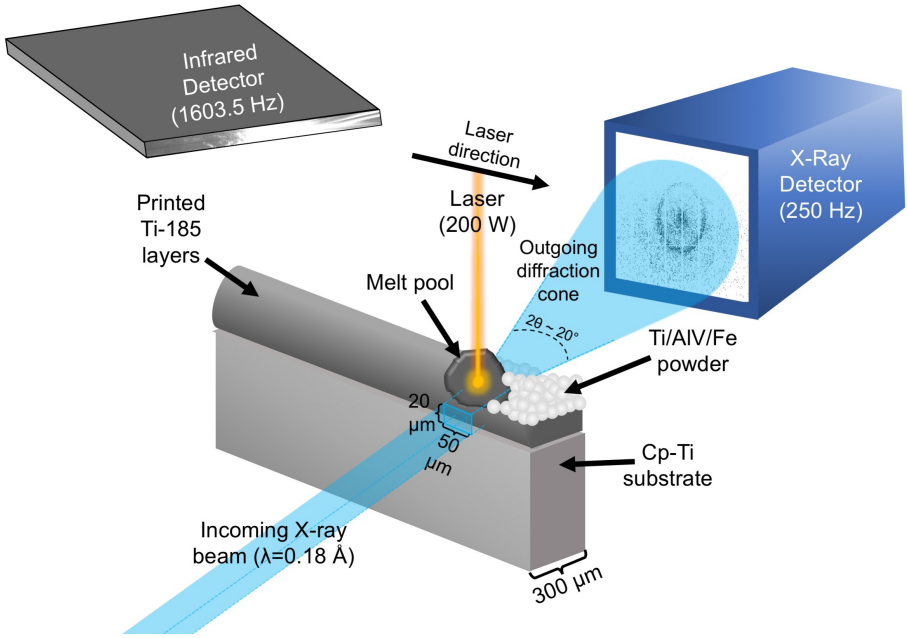

Figure 4.3: Setup of SLM concurrent with sXRD and IR imaging in the ISOPR. For the purpose of highlighting important features of the setup, this diagram is not to scale.

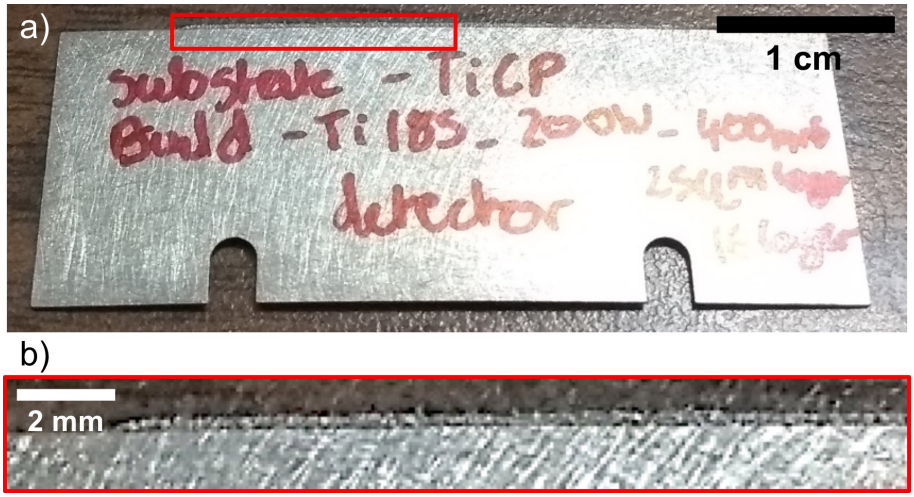

Figure 4.4: a) cp-Ti substrate on which the Ti-185 single wall was printed. b) shows a close-up of the printed wall.

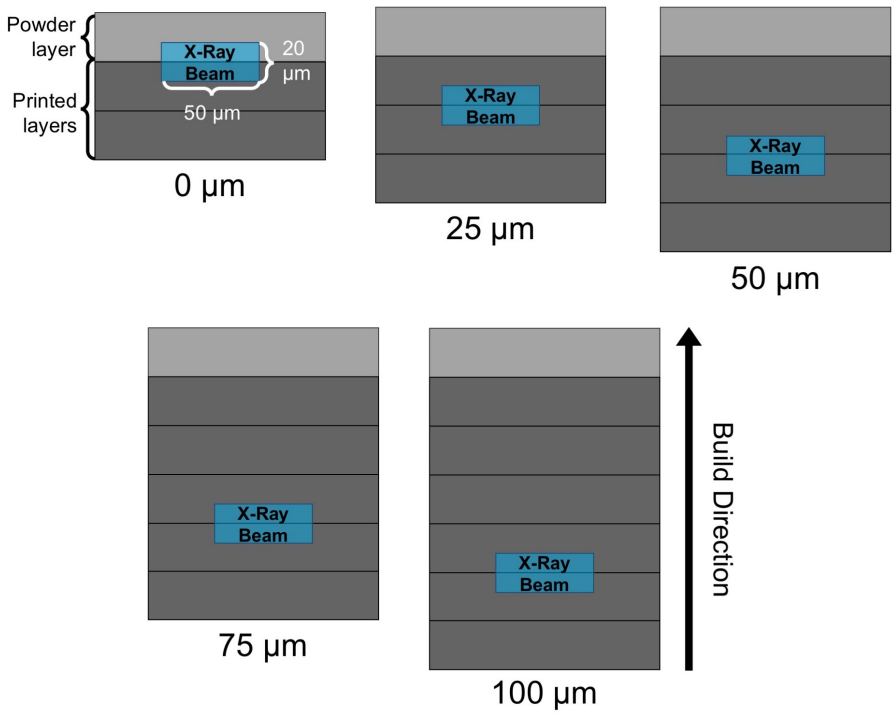

Figure 4.5: Position of the X-ray beam during sXRD relative to the powder layer and the printed layers beneath it.

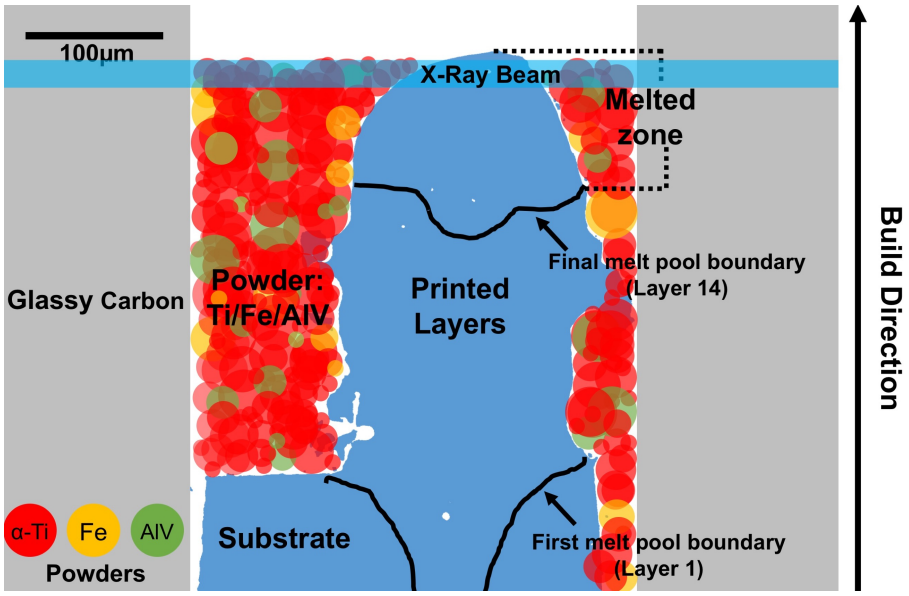

Figure 4.6: Accumulation and diffraction of unmelted powder between the printed Ti-185 layers and the glassy carbon walls.

which performed the conversion can be found in Appendix B. Due to the angled mounting of the IR detector, the temperature fields required a readjustment. A readjustment was performed by setting the maximum temperature point at each frame to coordinates (x,y)=(0,0). The frames were averaged. Hence, from a spatial perspective, (x,y)=(0,0) represented the point of the laser, a moving frame of reference, and a point at a distance x µm represented a single point in time at a given distance from the maximum temperature. However because the laser speed was constant, the scanning direction, x, could be converted to time, where (t,y)=(0,0) represented a stationary frame of reference, and the time t ms represented a single point in space at a given time in printing. Because the y-direction was spatial, a slice of constant x or constant t represented the same x or t value respectively at a given time. The detector could not detect temperatures below 958 K, and temperatures were inaccurate close to this limit. Hence, 1273 K was set as a temperature cutoff limit.

4.4 Rosenthal Temperature Predictions

The high temperature limit of 1273 K and its applicability only to the experiment surface called for a method to predict the temperatures outside this limit and the temperatures below the surface. The Rosenthal Solution, originally developed to predict temperature changes during welding [61], has been adapted to predict temperatures in SLM. The Rosenthal Solution assumes the following:

1. The laser is a point source.

2. Material properties are constant (i. e. not a function of temperature, and do not vary between the powder, the printed material, and the substrate).

3. Radiation and convective losses to the surroundings are negligible. The only heat loss is via conduction of a semi-infinite sink below the layers (that is, the substrate).

Temeperatures are valid only below the melting point. The thin-wall solution adapted for SLM by Bontha et al. was employed, as follows:

$$T = \frac{\alpha Q}{\pi k b} e^{-\bar{x_0}} (\sqrt{\bar{x_0}^2 + \bar{z_0}^2}) + T_0 \tag{4.1}$$

where T is the temperature at coordinates x_0 and z_0 (scanning and depth directions respectively with respect to the moving laser), T_0 is the ambient temperature, Q is the laser power, α is the absorptivity, k is the thermal conductivity, b is the width of the thin wall, $\bar{x_0}$ is

$$\bar{x_0} = \frac{x_0 \rho c V}{2k} \tag{4.2}$$

and $\bar{z_0}$ is

$$\bar{z_0} = \frac{z_0 \rho c V}{2k} \tag{4.3}$$

where ρ is the density, c is the specific heat capacity and V is the laser speed [62].

Properties were used from [21]. The properties of Ti-6Al-4V were used at 1600 °C, or 1873 K. High-temperature properties as a function of temperature are only available for Ti-6Al-4V and commercially pure Ti. The properties of Ti-64 are similar to that of other Ti alloys, but different from those of cp-Ti. For example, cp-Ti has a higher thermal conductivity and lower heat capacity relative to that of other Ti alloys [52, 63, 64]. Properties at the solidus were taken to better reflect the thermal behaviour at high temperatures. The solidus of Ti-6Al-4V is at 1605 °C, or 1878 K. Properties were only available at 1600 °C and not 1605 °C, and hence they were used. The thermal properties of Ti-6Al-4V at this temperature are shown in Table 4.1.

Property	Value
T_m	1873 K (1600 °C)
ρ	4198 kg/m^3
k	27 W/m·K
C_p	750 J/kg·K

Table 4.1: Values of Ti-6Al-4V inputted into the Rosenthal equation. Values were taken from [21].

The ambient temperature T_0 was set to 298 K. The power inputted into the equation was modified from 200 W, used in the experiments, to match the melt pool length found in the experiments. It was found that an apparent power of 290 W gave a matching melt pool length in the Rosenthal solution to that of the experiment, as will be explained further in Section 5.3.1: Mixing in the Melted Zone. An α value of 0.4 was used. The work of Allen et al. showed that in the transition mode between

conduction and keyhole melt pool shapes, α is 0.34-0.53 [65]. As will be shown in Section 5.2.3: Microscopy, the melt pool shapes conform to the transition mode.

4.5 Post-Mortem Analysis of the Printed Wall

While sXRD could demonstrate the phase transformations at and below the surface, it could not show the final microstructures, or the degree of alloying. Hence, Backscatter Electron (BSE) imaging, Electron Dispersive X-Rray Spectroscopy (EDX) and Electron Backscatter Diffraction (EBSD) were employed. The following section explains the sample preparation on the ISOPR-printed wall and the resulting electron microscopy which was performed. Electron microscopy was performed at the Canadian Centre for Electron Microscopy.

4.5.1 Sample Preparation

The goal of electron microscopy was to understand the microstructural gradient along the build direction. Hence, the sample face utilized in electron microscopy needed to be parallel to the build direction. As shown in Figure 4.7, the face parallel to the thickness and build directions and perpendicular to the scanning direction was chosen for viewing in electron microscopy. This face was chosen, rather than that perpendicular to the thickness direction, as it allowed for more room for error in grinding and polishing along the scanning direction. This was required as the printed tracks were 3 cm long, compared to the thickness direction, which was 300 µm thick.

Samples were sectioned perpendicular to the scanning direction into three 1 cm-long pieces using a water-cooled precision cutter. The sectioning of the sample is

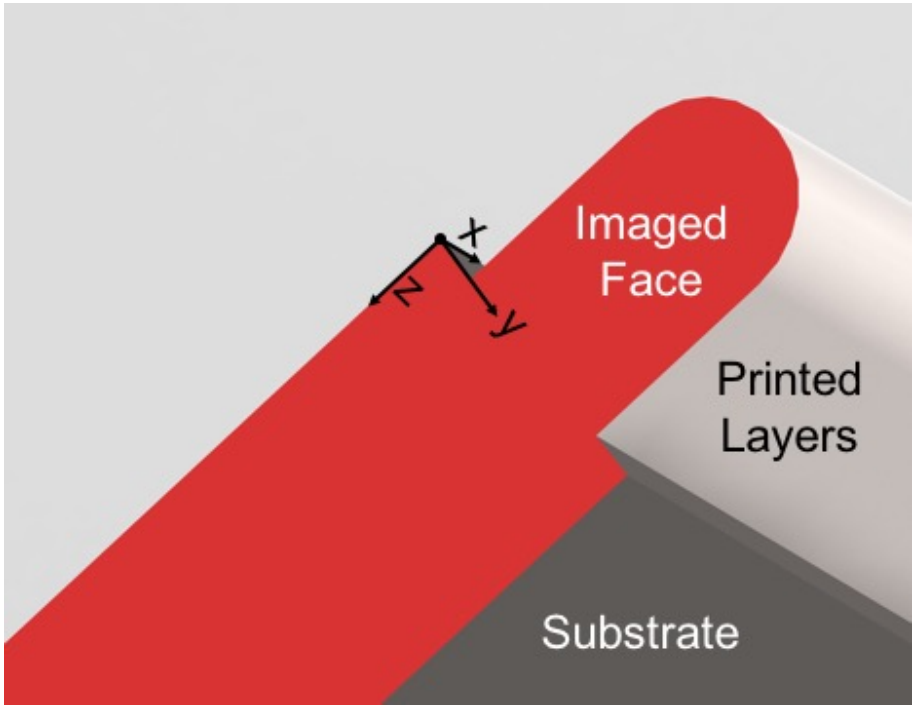

Figure 4.7: Imaged face for electron microscopy.

shown in Figure 4.8. Sections were cut for the first millimetre at 0.020 mm/s and for the remaining length at 0.030 mm/s. This ensured care in sectioning the printed wall (estimated 350 µm in height). Figure 4.9 shows the sample just before it was cut in the precision cutter. The three samples were mounted in epoxy, with the length perpendicular the scanning direction facing upward. The epoxy-mounted samples are shown in Figure 4.10 a), with a close-up of the printed layers shown in b). The epoxy-mounted sections were grinded and polished using an automatic polisher on co-rotation. They were grinded using 600, 800 and 1200 SiC paper for 3 min per size with a force and speed of 15 N and 300 rpm respectively. They were first polished using a diamond suspension of 3 µm for 20 minutes with a force and speed of 20 N and 150 rpm respectively. They were then polished using a solution of 75% OPS and 25% hydrogen peroxide at 0.25 µm for 10 minutes using a force and speed of 10 N and

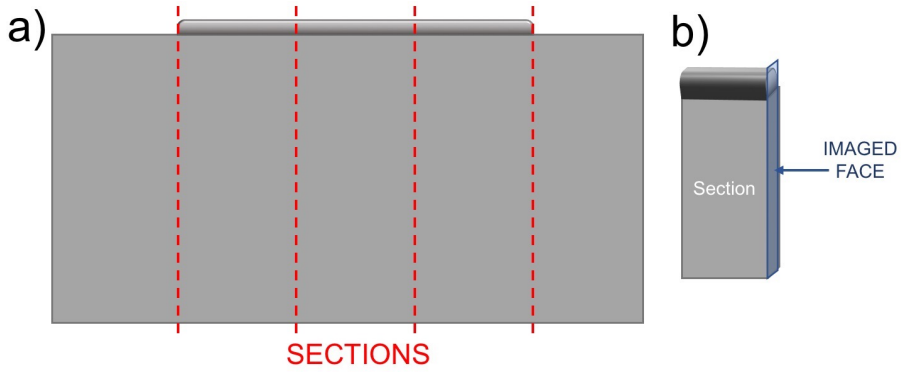

Figure 4.8: a) Sections of the sample formed by cutting. b) Imaged face of the resulting section.

140 rpm. The polished samples were coated with a carbon coating and Ni paint to ensure electrical conductivity. Prior to performing EDX, a strip of Cu tape was added for calibration. Carbon coating was performed at the Canadian Centre for Electron Microscopy. Figure 4.11 shows a secondary electron image of the sample with the Ni paint and a strip of Cu tape.

4.5.2 Electron Microscopy

Backscatter electron (BSE) imaging was performed as a precursor to other forms of electron microscopy. The image depended on the atomic numbers of the different constituents; regions with higher atomic number reflect more electrons and hence appear as lighter than regions with lower atomic numbers [66]. Hence, composition contrast indicates varying elemental distribution. In this project, it indicated either of the following: different phases, or regions of varying homogeneity. It also allowed the visualization of the melt pool boundaries, hence showing the melted zone, the heat-affected-zone and the substrate-mixed zone due to the varying contrast. Melt pool boundaries have varying contrast due to varying cooling rates between top and

Figure 4.9: The sample prior to being cut in the precision cutter. Two jets of water are on either side of the blade.

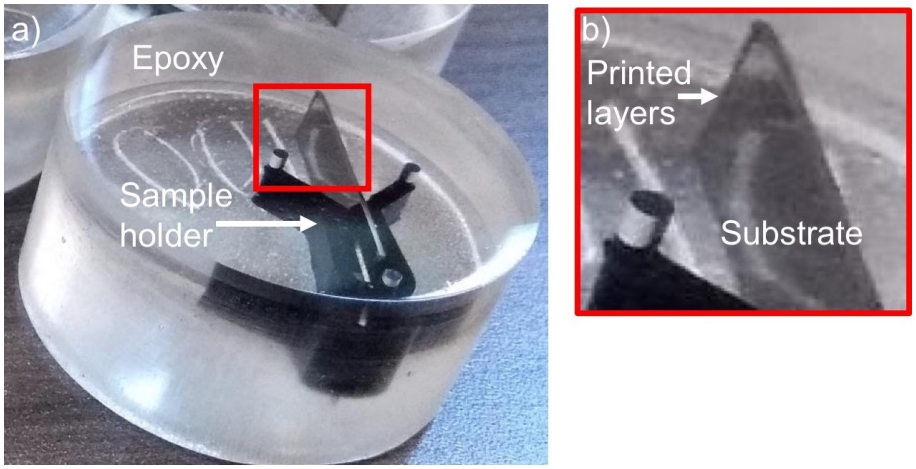

Figure 4.10: a) Cut sample mounted in epoxy. b) is a close-up of the printed layers in a).

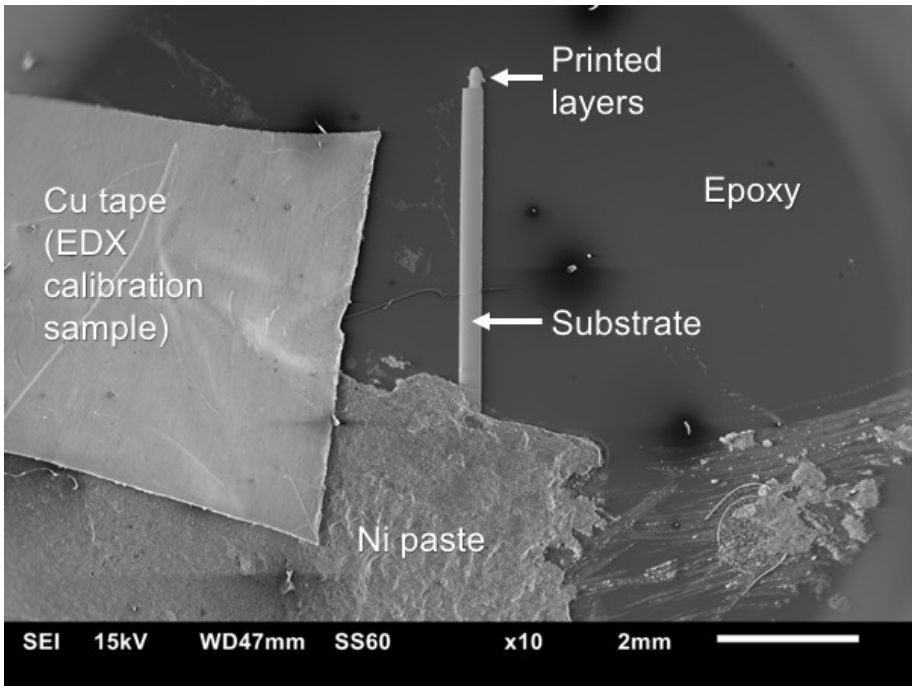

Figure 4.11: Secondary electron image of the grinded and polished epoxy-mounted sample. Cu tape and Ni paste are also featured on the mount.

bottom, and hence different rates of elemental segregation. BSE imaging was performed on the JEOL 6610 LV using a working distance of 10 mm, a voltage of 15 kV and a zoom of x200.

EDX was performed to investigate the compositional differences in detail. EDX detects characteristic X-rays produced from interaction with the X-ray beam. Characteristic X-rays correspond to the atom from which they were emitted, and can be used to identify individual elements. The results of EDX should be treated with a degree of caution, however. It has a low dimensional accuracy on the order of 1 µm. Furthermore, X-ray emission induced by an electron beam may induce further X-ray emission in the interaction volume. However EDX can qualitatively show relative concentration differences in an area [66]. For this study, it showed whether alloying was completed along the length of the printed wall. EDX was performed on the JEOL 6610 LV on 150-µm sections at a zoom of x700, which were later joined. The pixel dwell time was 50 µs, the process time was 4, and 20 frames were produced per image.

EBSD was performed to identify the grains' positions and orientations and to obtain a phase map. While Section 4.2. explained about using diffraction with X-rays, this method performs diffraction using outgoing backscatter electrons. The diffracted backscatter electrons create a pattern of intersecting bands of different slopes and widths called a Kikuchi Band Pattern. Indexing and matching Kikuchi patterns to phases and orientations is done via software through a Hough transform. EBSD has a high resolution. For example, at a voltage of 20 kV, the resolution is below 0.1 µm [66]. EBSD was performed with the JEOL JSM-7000F using an accelerating voltage of 30.00 kV and a specimen mount angle of 70.00° (which maximized the BSE emission). Matches with α-Ti and β-Ti CIF files in the system were performed.

Image cleaning was performed to clear the images of noise.

4.6 Chapter Summary

In this chapter, the methods to carry out the objectives explained in Chapter 3: Scope and Objectives were explained. In the ISOPR, SLM of Ti-185 from elemental Ti, Fe and alloyed AlV powders was performed concurrently with sXRD, allowing the phase transformations during printing to be observed. sXRD was performed at the melt pool surface and at depths of up to 100 µm below the melt pool surface, showing how a layer transformed as it underwent repeated heat treatments. Recording of IR images and their subsequent conversion to temperature fields showed the temperature changes. Prior to electron microscopy, the sample was mounted in epoxy to image the face perpendicular to the scanning direction to view the changes in post-printed microstructure along the build direction. This face was grinded and polished. BSE imaging, EDX and EBSD were performed on the polished face to understand the compositional and phase differences with respect to the build direction.

Chapter 5

Results and Discussion

5.1 Introduction

Using the methods present in Chapter 4: Methods, the goal of understanding the process of alloying was accomplished through the step explained in Chapter 3: Scope and Objectives. This chapter gives the reader an understanding of alloying by showing and discussing the results of this investigation. First, temperature profiles during printing are shown. The surface profile recorded using the IR detector and the below-surface Rosenthal prediction are shown. Together, they show the extent of melting at and below the surface, and the high cooling rates that influence the phase transformations. The phase transformation evolution, captured via sXRD, is then shown. It is explained in detail for the surface. The phase transformations recorded at depths of 25-100 µm are then shown and explained. Next, the results of post-mortem electron microscopy are shown, which includes which includes BSE imaging, EDX and EBSD. The degree of alloying and the final phase distribution in the melted and heat-affected zones are shown via EDX and EBSD respectively. In the Discussion, the results are

connected to provide a fundamental understanding of how homogenization begins in the melted zone, and progresses through the heat-affected zone until an alloyed microstructure is achieved.

5.2 Results

5.2.1 Thermal Profiles during SLM

Figure 5.1 shows the (top) two-dimensional and (bottom) centreline temperature profiles on the powder surface during SLM as acquired by the IR camera as the laser beam moved from right to left. Due to the steady-state nature of the process, a stationary frame-of-reference can be used. Thus, position $(x, y) = (0, 0)$ corresponds to the centre of the laser. The x-coordinate can additionally be converted to a time coordinate by dividing by the laser scanning speed. Negative horizontal coordinates represent in front of the laser or in the future for a spatial- and time-based coordinate respectively. Positive horizontal coordinates represent the position behind the laser or in the past for a spatial- and time-based coordinate respectively. Due to temperature limitations of the camera, the thermal profile was only generated between -1 and 1.5 mm, or -2.5 to 3.75 ms.

As can be seen in the figure, when the laser arrived, the powder heated rapidly at a rate of $\sim$ 1,000 K/ms to a temperature of 2,800 K, which is above the melting temperatures of Ti, AlV, Fe and the Ti-185 alloy. It then cooled rapidly at an initial rate of 1,000 K/ms, spending 1.5 ms molten before solidifying, and then cooling at a rate of 200 K/ms. The melt pool was 580 µm wide. From the point of solidification, it took 1.7 ms to reach the β-transus temperature (1583 K).

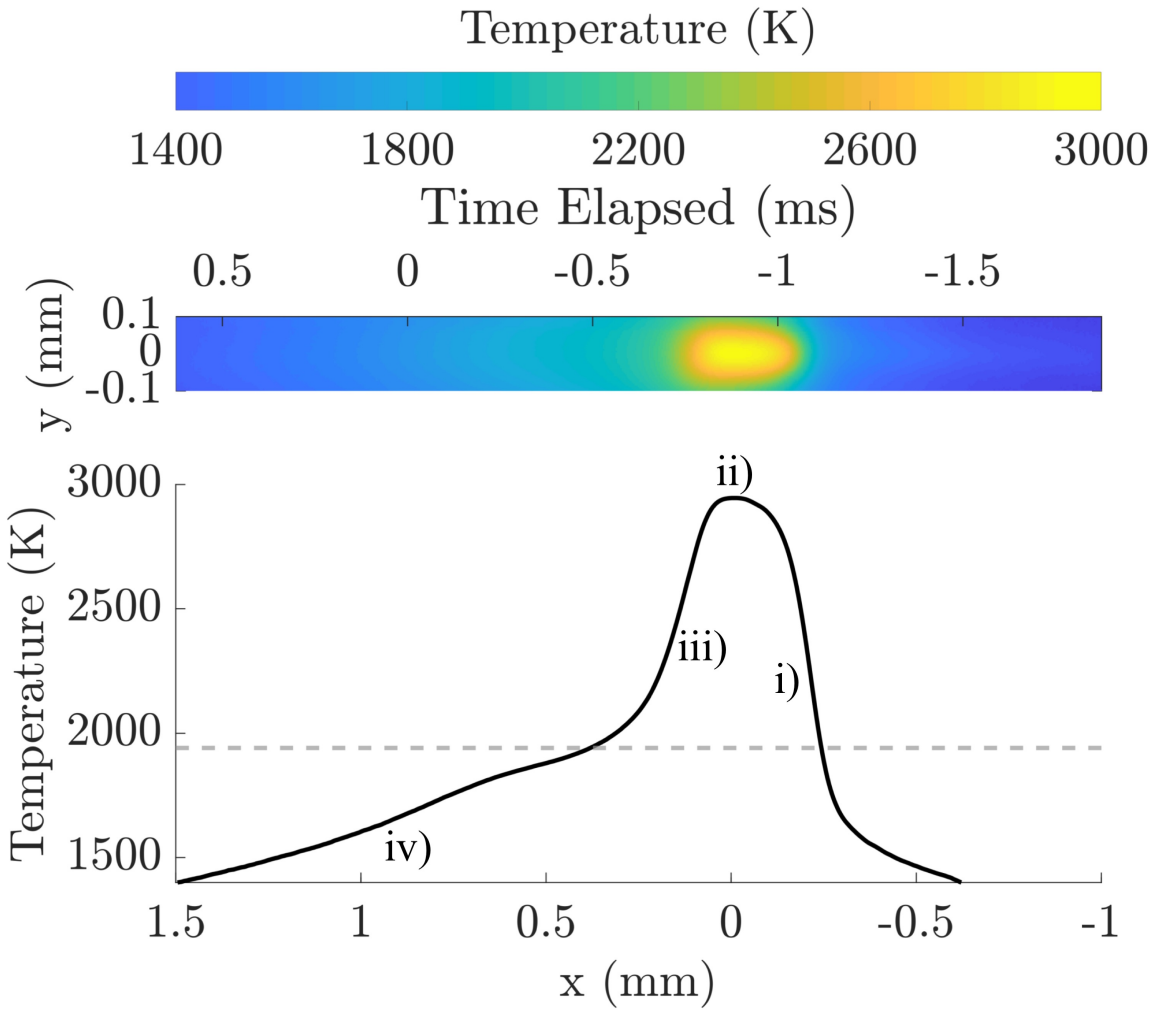

Figure 5.1: Time- and position-dependent temperature profile at the surface as a (top) two-dimensional map and (bottom) one-dimensional centreline profiles during SLM. For reference, the melting point of titanium (1941 K) is also plotted as a gray, dotted line. At points i) and iii), the heating and cooling rates are 1,000 K/ms; at point ii), the maximum temperature observed, 2830 K; at point iv), a cooling rate of 200 K/ms is observed.

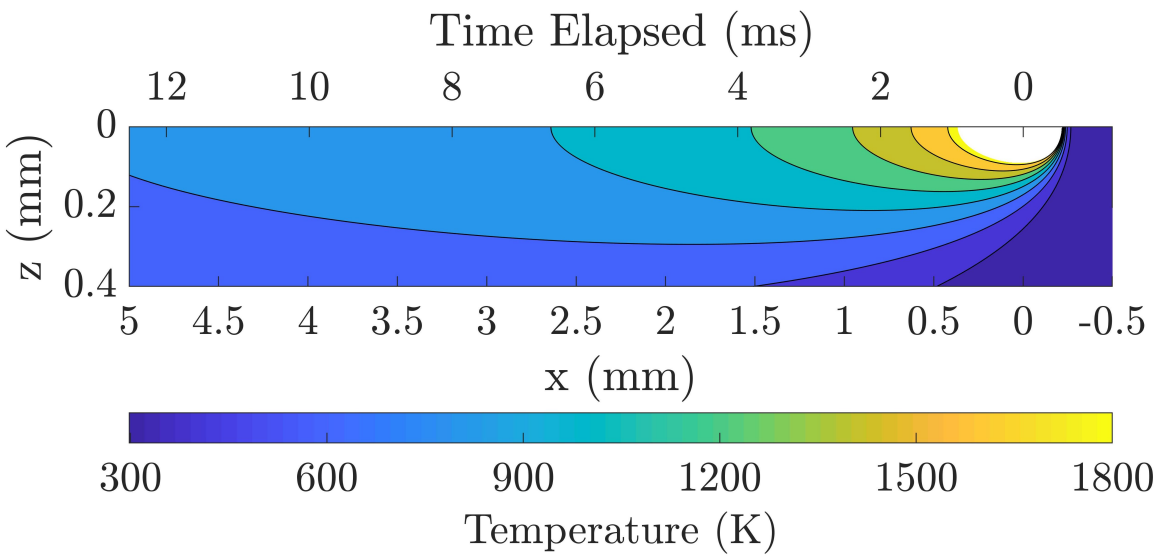

Figure 5.2: Estimation of the steady-state sub-surface temperatures via the Rosenthal equation assuming an input power of 290 W. The x- and z- axes are not to scale relative to one another to emphasize the temperature gradient in the z-direction.

Figure 5.2 shows the sub-surface temperatures estimated via the Rosenthal equation. α was set to 0.4, as α-values of 0.34-0.53 have been recorded in the transition mode between conduction and keyholing modes [65]. As will be shown in the BSE imaging results in Section 3.3, melt pool shapes of this type were observed. An apparent power of 290 W was used in place of the actual power 200 W in order to match the calculated melt pool width with the measured value seen in Fig. 5.1. The use of an apparent power suggests that factor(s) not included in the Rosenthal equation itself were in play, which will be discussed in Section 5.3.1: Mixing in the melted zone. The melt pool depth was $\sim$ 90 µm, indicating that at least 3-4 layers underwent remelting. The β-transus of Ti-185 was reached at depths up to 115 µm, while the β-transus of pure Ti was reached at depths of up to 170 µm.

5.2.2 X-ray diffraction during SLM

Figure 5.3 shows the sXRD peak evolution for the phase transformations at the melt pool surface. Frames are shown before printing (0 ms), at the start of the phase transformation (4 ms) and at its completion (64 ms). The starting intensities of the peaks, at 0 ms, varied between the five repeats. Each contained α-Ti peaks. Some contained weak AlV or Fe peaks, but they were not always present due to the size of the acquisition volume and the random sampling of powders. Hence, a representative pre-phase-transformation frame with both AlV and Fe is shown at the top of Figure 6 to demonstrate all the peaks present in the initial powder. Upon laser heating, the powder melted, however because it was molten for only 1.5 ms (see Fig. 5.1), an amorphous melt curve was not observed in the 4 ms frame (as the acquisition rate was 250 Hz, there were no intermediate frames). The first sign of a phase transformation were the suddenly-high β-Ti and low α-Ti signals (middle line, Fig. 5.3). Over the course of the phase transformation, the β-peaks shifted to the right as the sample cooled and the lattice parameter decreased. The β intensities also decreased, while α intensities increased up until the end of the phase transformation. The phase transformation ended at 36 ± 13 ms, depending on which data set from passes 5-9 was examined. At the end of the phase transformation period, a weak β-{110} peak was seen to overlap with the α-{002} peak. However, the β-{002} peak was not visible except for only one pass of the laser beam. Alone, this suggested that a low amount of β was retained. However the fact that there were considerable unmelted powders, as shown in Figure 4.6, meant that some of this α-Ti was not part of the printed layer.

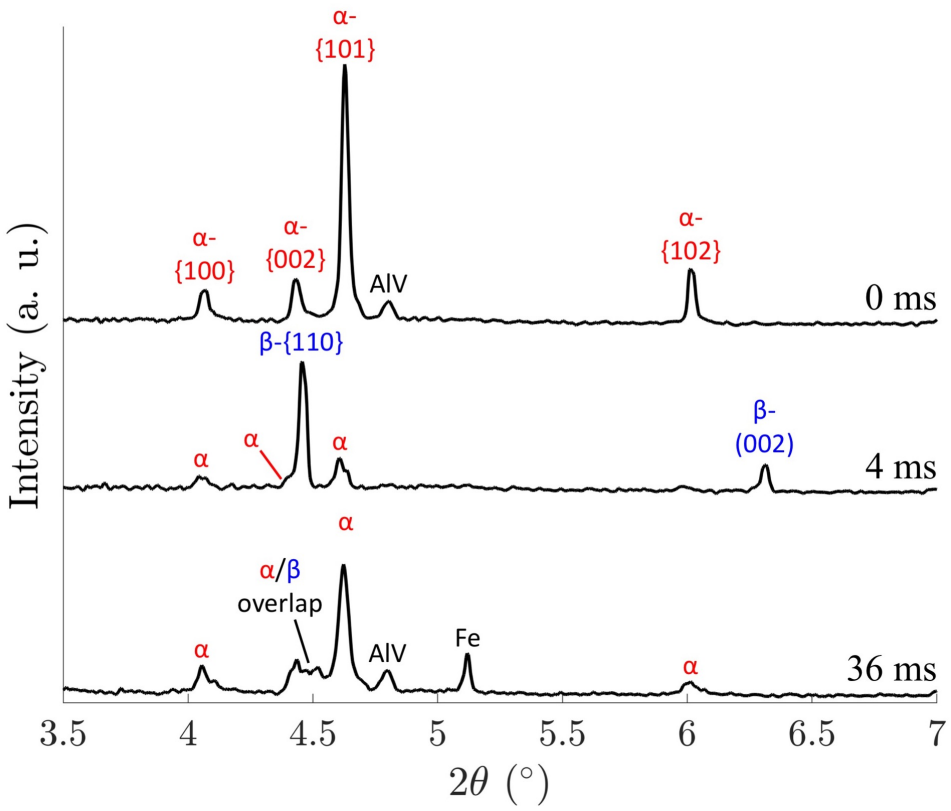

Figure 5.3: Melt pool sXRD. Frames are shown before printing (0 ms), at the start of the phase transformation (4 ms) and at its completion (64 ms).

Figure 5.4 a) shows the post-phase transformation sXRD peaks during the reheating cycles at the depths of 25, 50, 75 and 100 µm below the surface. The post-phase-transformation peaks are also included at 0 µm as a reference. Figures 5.4 show the post-phase transformation sXRD peaks at depths of 75 and 100 µm below the surface, zoomed in by a factor of 13.3, to show the presence of the β-{002} peak. This peak was used to identify whether the α-{002}/β-{110} overlapping peak corresponded to the presence of β; if the β-{002} peak was present, it indicated that the overlapping peak in question was predominantly β-{110}. At 25 µm below the surface, the sample heated up to a mixture with high β and low α intensities. Again, the β peaks shrunk and shifted to the right with respect to the initial phase transformation peaks during cooling. However, they did not fully disappear, coexisting along the grown α peaks. At 50 µm below the melt pool, this combination was reheated to have high β and low α peaks. The β peaks again shrunk and shifted to the right, while the α peaks re-emerged, without fully disappearing. The same process occurred at 75 and 100 µm below the surface. Again, due to the accumulation of unmelted powders, it is possible that this sample had less α-Ti than was indicated in the plots.

5.2.3 Microscopy

Figure 5.5 a) shows a BSE image of the sample cross-section. The depth of the melted zone and HAZ are clearly evident. The melt pool is approximately 100 µm deep at the edges, but 140 µm at the centre. The depth of the HAZ was determined by identifying the depth at which there was no more variability along the centreline. The HAZ extends up to 230 µm deep. At 300 µm, the substrate-mixed zone begins, a zone in which the substrate mixes with the printed layers. This zone continues up

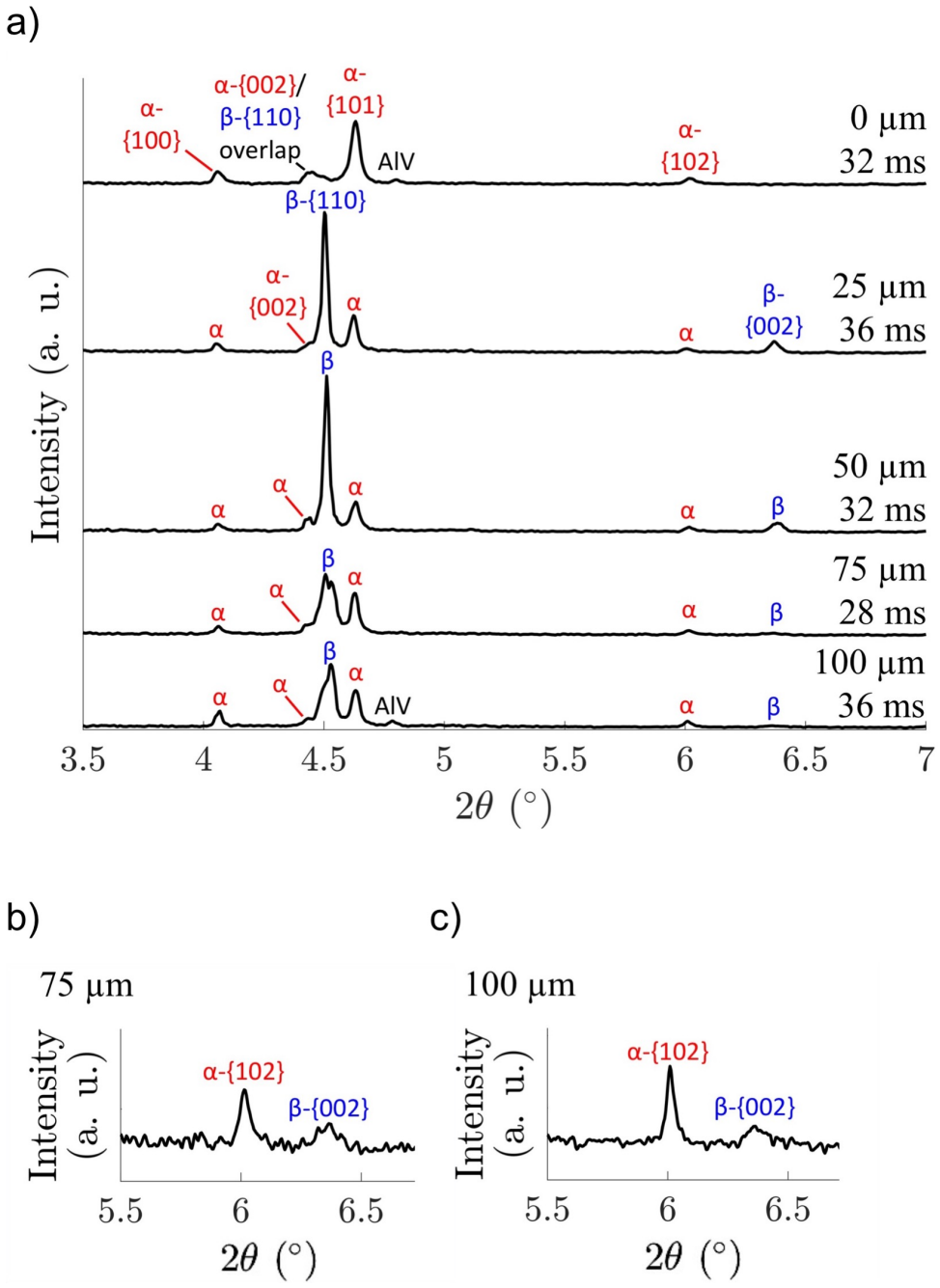

Figure 5.4: a) Post-phase-transformation sXRD frames after each laser pass when a single layer is tracked through reheating cycles. The duration of each phase transformation is also shown. b) and c) show the $\alpha\{102\}$ and β-$\{002\}$ peaks in the 2ϑ=5.5-6.7° range magnified by a factor of 13.3 at depths of 75 and 100 µm respectively.

until 400 µm, at which the sample is completely substrate. The printed layers are 200 µm thick, leaving a 100-µm thick gap in which unmelted powders accumulated, confirming that sXRD detected more α-Ti than was present in the sample. Finally, there are lines indicating the contours of the melt pools that formed during each pass. The bottom-most melt pool boundary has a keyhole-shaped mode, while the topmost boundary conforms closer to a conduction-moded melt pool shape [67, 68, 69].

The corresponding EDX images of the sample are shown in Figure 5.5 b). As can be seen, the melted zone alternates between evenly-alloyed regions and those concentrated in a single element (or two, in the case of Al and V). In the heat-affected zone, there is less homogeneity near the edges due to a lower heat input there. However, near the centre of each layer, the sample is homogeneous.

Figure 5.6 shows the EBSD image with a) and b) showing the respective orientation map and phase map of the whole section, c) and d) showing the respective orientation map and phase map of a section in the melt pool, and e) indicating the colour coding for the phase maps in a) and c). In 5.6 a) and b), the boundary between the melted zone and the HAZ is not clear. However, for the purposes of interpretation we can use the mushy zone depth determined from BSE imaging (Figure 5.5 a)) of $\sim$ 100 µm at the edges and 140 µm at the centre. The boundary between the HAZ and the rest of the sample is, however, clear. This boundary is where there are no longer large (10-40 µm wide), curved regions of α, and only small pixels of α remain. This zone extends up to the substrate-mixed zone. In the melted zone, a mixed $\alpha + \beta$ structure was observed, with some layers having more than 50% α. The heat-affected zone is mostly β. However, some α is present as curved regions 10-40 µm wide. Within the HAZ, the larger regions of α formed along the melt pool

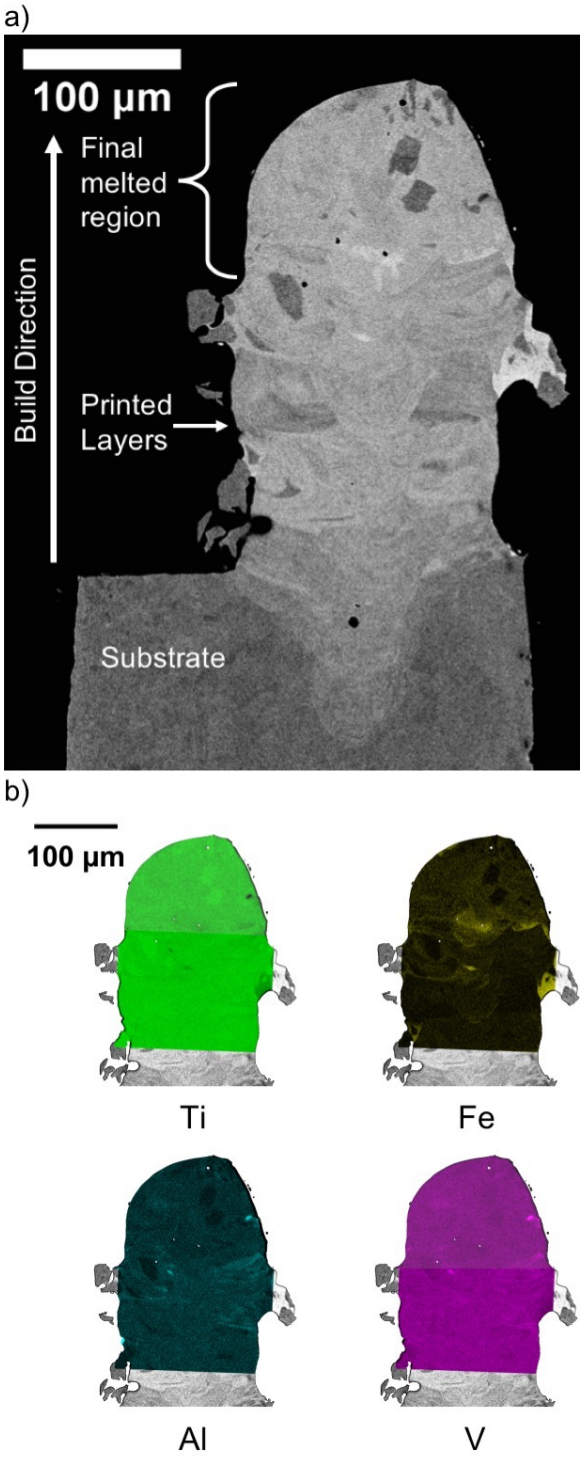

Figure 5.5: a) BSE image of the printed layers cross-sectioned perpendicular to the scanning direction. b) EDX maps of Ti, Fe, Al and V.

boundaries. Below the heat-affected zone, α is present in the form of small regions <3 µm in size (approximately 1-2 pixels wide) at the grain boundaries.

5.3 Discussion

5.3.1 Mixing in the melted zone

By combining the sXRD plots in Figures 5.3 and 5.4, the EDX maps in Figure 5.5) b) and the EBSD phase maps in Figures 5.6) b) and d), a clear view of in-situ alloying in SLM is presented. sXRD showed the transformation from α-Ti powder to a liquid, and then to a mixture of α and β, as shown in Figures 4 and 5. At depths of 25-100 µm, the similarity of the frames (α and high-β signals) (Figure 5.4) initially suggested that there was little microstructural refinement between laser passes. However, as the Rosenthal solution predicted (see Figure 5.2) and BSE imaging verified (Figure 5.5 a)), the sample remelted at these depths. At each of these depths, the material transformed to a liquid, and re-solidified within $\sim$ 1.5 ms. While a liquid, the powders would have completed a partial convective current cycle induced by Marangoni Flow, and have moved to a random position in the melted zone [12]. As shown in Figure 5.5 b), the melted zone contains mixed regions and regions high in alloying elements. The phase maps (Figure 5.6 b) and d)) show a random distribution of α and β in the melted zone. On the variable distribution of elements as shown in Figure 5.5 b), it is expected that regions high in β-stabilizers (V and Fe) contain β, and those high in Ti contained α. Because Al and V were approximately in the same position in this region, Al would not be in the α-stabilized regions and hence only low-concentration areas would be α [63]. The random distribution of elements shown in Figure 5.5 b) led to a

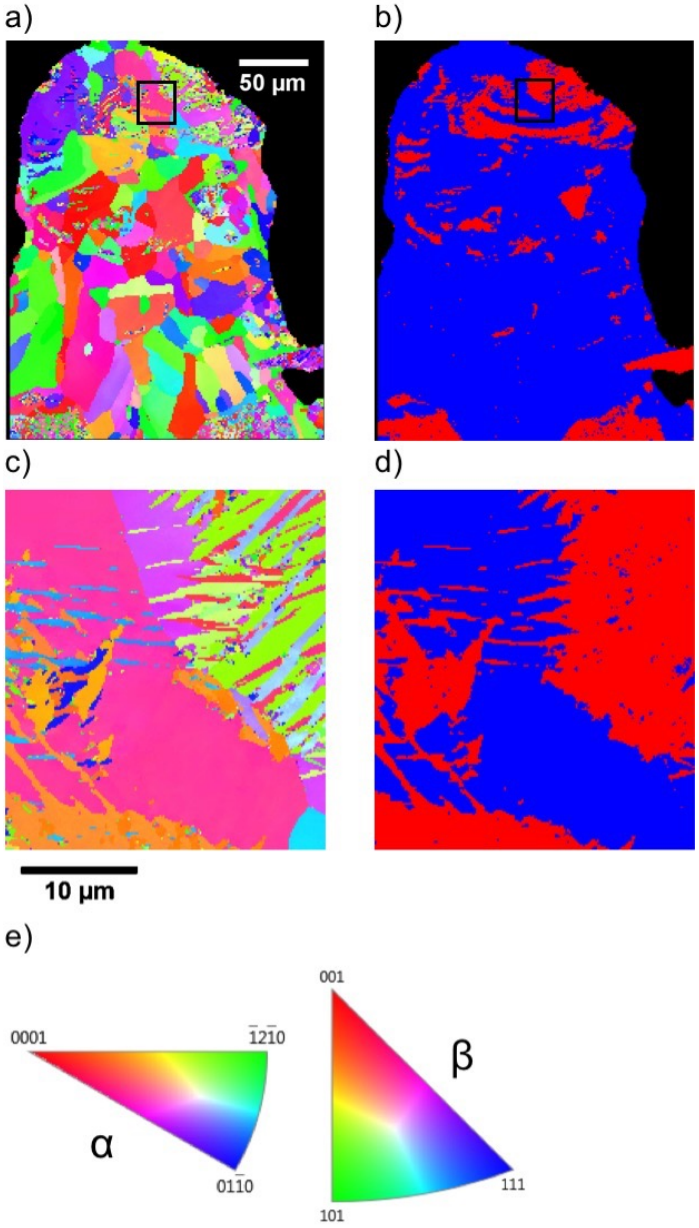

Figure 5.6: a) EBSD Orientation map and b) phase map of the microstructure. c) Orientation map and d) phase map of a high-resolution image of a melted zone area highlighted in a) and b). In b) and d), α and β are represented by red and blue respectively. e) Legend for orientation maps map in a) and c). Grain orientations are with respect to the build direction (vertical, pointing upwards). The scanning direction is into the page.

random distribution of α and β. In the 20x50x200 µm acquisition diffraction volume, the amount of α and β that formed after each remelting cycle also randomized due to the partially-alloyed powders' new positions. Hence, the α and β peak intensities in Figure 5.4 show no clear pattern of microstructural evolution at the end of the reheating cycles' sXRD patterns. This also accounts for the variability in the sXRD surface patterns (Figure 5.3), with runs showing variable amounts of β.

The extremely high cooling rates in the solid-state of 200 K/ms as shown in Figure 5.1 indicate that the α in the melted zone (Figure 5.6 b) and d)) was martensitic. The martensitic microstructure occurs in regions insufficiently β-stabilized when cooled at minimum rates of a few hundred K/ms [64]. No athermal ω is visible, however, as it forms in β-stabilized regions with rapid cooling rates [63], it is expected to be present. Because ω plates are nanoscopic, they would not be visible with EBSD, requiring TEM to be identified [70]. Additionally, our previous work on printing Ti-185 from elemental powders showed the presence of ω in the as-built bulk sample [20], confirming this mechanism of ω formation.

There are two factors which influence the mixing behaviour in the melt zone: heat imparted by the laser beam and heat generated via an exothermic mixing enthalpy. Heat generated via a negative enthalpy of mixing aids in the alloying process, while the absorption of heat from a positive enthalpy of mixing slows it [8]. As determined via ThermoCalc, Ti-185 has a negative enthalpy of mixing, and hence the heat released through alloying aided in the mixing process. The highest-concentration alloying element V (7.5 % atomic) has an endothermic enthalpy of mixing with Ti. Though enthalpies of mixing could not be determined with pre-alloyed AlV, the pre-alloying of V with Al would have decreased its enthalpy of mixing, allowing for the release

of more heat. Furthermore, the negative enthalpy of mixing of Fe would further contribute heat in the first stages of mixing. This explains why a surplus energy of 290 W was required in the Rosenthal solution (Figure 5.2) to match the actual melt pool size and depth, as the negative enthalpy of mixing was not factored into the Rosenthal solution. Additionally, in this system, a layer in the melted zone is remelted approximately 4-5 times, and each time allowed for further mixing.

5.3.2 Completion of Alloying in the Heat-Affected Zone

As is demonstrated in the EDX and EBSD phase maps in Figures 7 b) and 8 b) respectively, in the heat-affected zone, further reheating causes more mixing during each reheating cycle, causing more α to be converted to β. Grain boundary α is the first type of α to form upon ageing β-Ti (heating it below the β-transus) [64]. Though the peak temperature at the bottom of the HAZ, according to the Rosenthal solution is at least 950 K (at most 210 K below the β-transus temperature of pure Ti) (Figure 5.2), the cooling rate is still too rapid for significant α precipitation. At this depth, the maximum cooling rate ranges between 100 K/ms at 140 µm to 20 K/ms at 230 µm according to the Rosenthal Solution (shown in Figure 5.2, hence, the low amount of grain-boundary α. Additionally, the α present at the bottom of the melt pool boundaries, which formed as a result of high cooling temperatures and a lower thermal gradient, is converted to β over the length of the heat-affected zone. In the heat affected zone, further heating from the laser, along with the negative mixing enthalpy (the mixing enthalpy of Ti-185 at 900 K is -0.170 kJ/mol) further aid reheating, hence completing *in-situ* alloying.

Our previous work on printing Ti-185 from elemental powders obtained a mixed

α+β structure instead of mainly β with sub-microscopic grain-boundary α [20]. However, a lower energy density of 50.4 J/mm^3 was used, rather than 66.7 J/mm^3 as in this project. Hence, less energy was imparted per layer and less α at the edge of the melt pool boundaries was converted to β. Although the work of Azizi et al. showed homogeneity throughout the structure, the wall printed in this work only achieved homogeneity at the centreline, but not at the edges. This was due to a lower energy imparted on the track sides. However, if it was printed with multiple hatches, homogeneity could be achieved where tracks overlap with one another.

This work verifies what has previously been shown by Dobbelstein *et al.* [11] in that the surface of a laser-printed alloy is not homogenous. It expands on this by showing how mixing occurs through repeated passes of the laser. This work also confirms the observation of a graded structure between the top and bottom of a single wall laser-printed from elemental powders by Yan *et al.* and Kang *et al.* [13, 14]. It takes this work further by analysing the transformation from the melted zone to the bulk microstructure, via the heat-affected zone. This research has also used sXRD, in addition to conventional electron microscopy techniques, to explain the phase transformations in the microstructure, and relate them directly back the degree of alloying. Ultimately, this research has described how a single layer of elemental powder undergoes multiple intrinsic heating cycles as it develops into a bulk, homogenous microstructure.

The results of this investigation show that contrary to the work of [5, 11, 47, 38, 71, 4, 7, 10, 72, 73, 8, 34, 37, 74], the presence of unmelted powders at the surface is not a useful metric for determining if exposed layers in a sample are alloyed. Even though sintered unmelted powders may be absent on exposed surfaces,

the distribution of alloying elements will still be uneven, and not match the desired microscopic concentration. If it is desired to preserve exposed layers in a structure (for example, a lattice or honeycomb structure), techniques such as remelting each layer after building it may be performed. This technique has been observed in the literature to produce fewer unmelted particles at the surface, without inducing the negative impacts associated with a high laser power, such as keyholing or excessive vaporization [5, 46, 47, 11, 15, 45]. Additionally, though this was outside the scope of this project, the hatch spacing can be experimented with to facilitate homogenization away from the centre of the melt pool.

5.4 Chapter Summary

The aim of this chapter was to show how the alloying process occurred in laser AM by explaining to the reader, using Ti-185 as an example, the phase transformations and microstructural changes in the melt pool and heat-affected zone. Prior to showing the phase transformations and the final microstructures, the temperature profiles were provided to show the conditions under which printing occurred. First, the surface temperature profile as generated via IR imaging was shown. It demonstrated that the average melt pool length was ∼580 µm, and the material spent ∼1.5 ms molten. Temperatures of up to ∼2,800 K were reached. Cooling rates in the melt pool were ∼1,000 K/ms, while outside the melt pool, they decreased to ∼200 K/ms. The Rosenthal solution predicted the temperature below the surface, where the IR detector could not reach. A power of 290 W was used to match the melt pool lengths, suggesting the influence of a factor excluded from the Rosenthal solution. A melt pool depth of ∼90 µm (3-4 layers) was predicted, while the β-transus was predicted to be

reached up to $\sim$ 170 µm (6-7 layers).

Knowing the temperature changes under which the phase transformations took place, sXRD results were then shown. It was demonstrated that at the surface, α-Ti powder heated up rapidly to a liquid, solidified to β, then transformed to α, with a low amount of β. The phase transformation took <50 ms to complete. This was rapid enough that even though IR imaging confirmed that temperatures reached well above the melting point of all three constituent powders, an amorphous melt curve was not observed in a 4 ms frame. A 4 ms frame was longer than the 1.5 ms duration of melting. At depths below the surface of up to 100 µm, the printed layers melted, solidified to β and then transformed to a mixture of α+β. Again, even though sXRD did not capture melting, it was known through the Rosenthal solution that melting occurred at these depths.

Post-mortem electron microscopy results were then shown. The BSE image showed that there was an $\sim$100 µm gap between the printed layers and the glassy carbon, in which unmelted powders accumulated. It also showed melt pool boundaries on the sample. The topmost melt pool was determined to be 140 µm deep. The heat-affected-zone ranged from a depth of 140 µm to 230 µm. The elemental maps generated by EDX demonstrated the degree of alloying in each region. They showed a mixture of alloyed and unmixed regions the melted zone. In the heat-affected-zone, however, further mixing occured until an alloyed microstructure near the centreline was achieved. EBSD showed the post-printed microstructures. They showed a mixed martensitic α and β microstructure in the melted zone, which transitioned to a β microstructure with sub-microscopic grain-boundary α in the heat-affected zone.

In the discussion, the results were pieced together to explain how homogenization

occurs. In the melted zone, the laser heat and that from the exothermic enthalpy of mixing promoted partial mixing. However, the cooling rates were still too rapid for complete mixing. Hence, alloyed regions high in β and unalloyed regions high in martensitic α were produced. In the heat-affected-zone, laser heat and the exothermic mixing enthalpy further promoted homogenization. The bulk of the microstructure was transformed to β. However, cooling rates on the order of $\sim$20 K/ms promoted sub-microscopic α at grain boundaries. Though the alloying process was determined for Ti-185, the general mechanisms can apply to any system. Hence, this chapter has successfully demonstrated the alloying process.

Chapter 6

Conclusions and Future Work

6.1 Thesis Summary and Concluding Remarks

Laser additive manufacturing has the potential to manufacture out-of-equilibrium microstructures in near-net-shapes with little to no postprocessing steps. To leverage this process, novel alloys optimized for laser AM process parameters need to be developed. One option for developing and manufacturing novel alloys is in-situ alloying, which employs elemental powders that alloy in the melted and heat-affected zones. This gives a wide range of customizability which is useful in testing out different alloy compositions. Costs are lowered from not developing pre-alloyed powders. Additionally, the enthalpy of mixing may aid in heating. Elemental powders have been tested in SLM and DED. The current literature has demonstrated that homogeneity can be achieved in the bulk microstructure, although not immediately in the deposition of a layer. Upon deposition, a layer is not homogenous and may contain unalloyed powders. It is through multiple intrinsic heat treatments as subsequent layers are built upon it and it is reheated and cooled by the laser, each time with a different

thermal profile, that it alloys.

Prior to this thesis, no study had thoroughly investigated the transformations from the powder to the bulk microstructure, and related the transformations back to the degree of alloying. Additionally, no study had tracked the phase transformations or temperature changes in the melt pool, which can give insight into how an alloyed microstructure begins to form.

This thesis aimed to fill these knowledge gaps by using sXRD and IR imaging to observe the phase transformations and temperature changes in the melt pool during the SLM of a single wall of Ti-185 from elemental powders. Additionally, EDX and EBSD were used to relate the microstructure in the melted, heat-affected and alloyed zones to the degree of alloying. The Ti-185 system was chosen because it is known to achieve homogeneity, its powder components have similar melting points, and comparisons can be facilitated with the work of Azizi et al., who previously printed alloyed Ti-185 from Ti, Fe and AlV powders via SLM [20].

The following conclusions were made about the alloying process from elemental powders:

1. In the melted zone, the energy imparted from the intense, focused laser and the exothermic enthalpy competed with the insufficient diffusion of elements. Insufficient diffusion was attributed to the rapid cooling rate of over 200 K/ms and hence, the low phase transformation time (<50 ms).

2. The combination of competing driving forces yielded a partially alloyed microstructure, with alternating regions of mixed and unmixed regions. In the case specifically of printing Ti-185 from elemental powders, α was concentrated in unmixed Ti, while β was concentrated in regions high in alloying elements.

3. In the heat-affected zone, with multiple reheating cycles, induced by laser heating and the exothermic mixing enthalpy, homogenisation was achieved. In the case of Ti-185, the microstructure transformed to the desired phase β, however, with microscopic α precipitated via the high cooling rates on the order of 10-100 K/ms).

6.2 Recommended Future Work

This work has offered a fundamental understanding of how elemental powders are alloyed in laser AM. Having said this, there are multiple avenues for future research.

In the sXRD experiments, insufficient powders were sampled per frame to ensure a random sampling, preventing consistency between laser passes. Furthermore, the low frame rate of 250 Hz prevented capturing of key phenomena, such as melting (which occurred within 1.5 ms). Having said this, the following may be performed to improve the sXRD experiments:

1. Sample a higher number of powders to improve repeatability. This includes using a wider X-ray beam, or a taller beam with a higher layer height, so that the beam does not overlap multiple X-ray beams. Calta et al. successfully used beam dimensions of 300x50 µm. With the large powder sampling, they deconvoluted individual peaks into contributions from the melted and heat-affected zones [51].

2. Increase the frame rate from 250 Hz to capture the melting and solidification transformations. Given that a point on the surface was molten for 1.5 ms, the maximum frame rate observed to date of 20 kHz ([48]) would have 30 frames

with an amorphous liquid curve, which is sufficient to understand it. However, there is a trade-off between frame rate and signal strength. Improvement of the frame rate while capturing a sufficient signal strength should be explored. This may involve signal processing techniques.

In Section 2.5, different methods of improving the alloying process without using a heat treatment were identified. It is of interest to investigate how the alloying process improves with each technique. Hence, the following can be tested:

1. Remelt each layer after printing them. With increased remelting cycles, fewer number of cycles are needed to homogenize the microstructure.

2. Use fine minority element and coarse parent element (in this case, Ti) powder. This was shown by Simonelli et al. to improve homogeneity [16].

3. Satellite minority powders onto the parent element prior to printing. This was also demonstrated by Simonelli et al. to improve homogeneity [16].

Appendix A

Plotting of Individual XRD Frames

Appendix A shows the MATLAB codes used to order and plot the one-dimensional sXRD patterns. The patterns were previously converted from 2D .cbf images to 1D .mat files by collaborator Dr. Samuel Clarke (this contribution was mentioned in the Preface).

A.1 MATLAB Script to Import and Sort .mat Files

In the following code, individual .mat files representing data from each frame were inputted into MATLAB and grouped by layer. The author of this thesis modified this code from the original version by Dr. Samuel Clarke in not including a waterfall plot. Additionally, the resulting structure sample.mat was saved as `intermediate_samplev400.mat` such that this code would not need to be run again to access the sorted data.

```
1 clear all; close all;
2 dn = dir('data');
```

```
exit_flag = 0;

for i = 3:(length(dn)-1)
    d = dir([dn(i).folder '\' dn(i).name '/P3/*.mat']);
    if length(d) > 1
        fprintf('\r %s    \n',[dn(i).name]);
        sample = load_patterns(dn(i),d);
        sample = layer_sort(sample,[dn(i).folder '\' dn(i).
            name '\' dn(i).name]);
    end
end

function sample=load_patterns(dn,d)
exit_flag = 0;
c = 0;
fn = input('Is there any sorted data to load? Enter filename:
    ');
if isempty(fn) == false, load(fn); else, sample =
   sort_sample_metadata([],1); end
while exit_flag == 0
    if c > 0
        sample = sort_sample_metadata(sample,0);
    end
    for i=1:sample.layer(end).patterns.number
```

```
24          c = c+sample.layer(end).patterns.voids;
25          temp = load([dn.folder '/' dn.name '/P3/' d(c+i).
                name]);
26          fprintf('\r %s \n',[dn.name '/P3/' d(c+i).name]);
27          fprintf('\r %f \n',length(d)-(c+i));
28          sample.layer(end).data(i).th = temp.w.th;
29          %sample.layer(end).data(i).th = real(asin(9.88320442*
                sin(temp.w.th))); % Farheen added this to convert
                from ESRF to Cu-kalpha.
30          sample.layer(end).data(i).q = temp.w.q;
31          sample.layer(end).data(i).r = temp.w.r;
32          sample.layer(end).data(i).phi = deg2rad(wrapTo360(
                temp.w.phi+90));
33          sample.layer(end).data(i).int1d = temp.w.int1d.y;
34          sample.layer(end).data(i).int2d = temp.w.int2d.y;
35          sample.layer(end).data(i).y0 = (1/sample.layer(end).
                patterns.frequency)*sample.layer(end).laser.speed*
                i-(sample.layer(end).laser.direction*sample.layer(
                end).beam.position.y);
36          sample.layer(end).data(i).y0 = sample.layer(end).data
                (i).y0+(sample.layer(end).patterns.aqperiod*sample
                .layer(end).laser.speed+sample.layer(end).beam.
                size.y/2)/2-sample.layer(end).beam.size.y/2;
```

```
37          sample.layer(end).data(i).z0 = sample.layer(end).beam
                .position.z;
38      end
39      c = c+sample.layer(end).patterns.number;
40      if c == length(d), exit_flag = 1; end
41  end
42  end
43
44  function sample = sort_sample_metadata(sample,flag)
45  if flag == 1, i=1; else, i = length(sample.layer)+1;  end
46
47  % Layer number
48  if i == 1, suggestion = 1; else, suggestion = sample.layer(i
      -1).number+1; end
49  sample.layer(i).number = input(['Enter layer number -
      suggestion:', num2str(suggestion,'%5.2f') '\n']);
50  if isempty(sample.layer(i).number), sample.layer(i).number =
      suggestion; end
51
52  % Number of patterns in layer
53  if i == 1, suggestion = 250; else, suggestion = sample.layer(
      i-1).patterns.number; end
```

```
54 sample.layer(i).patterns.number = input(['Enter number
       patterns in layer - suggestion:', num2str(suggestion,'%5.2
       f') '\n']);
55 if isempty(sample.layer(i).patterns.number), sample.layer(i).
       patterns.number = suggestion; end
56
57 % How many void patterns not to be loaded
58 suggestion = 0;
59 sample.layer(i).patterns.voids = input(['Enter number of void
        patterns not to be loaded - suggestion:', num2str(
       suggestion,'%5.2f') '\n']);
60 if isempty(sample.layer(i).patterns.voids), sample.layer(i).
       patterns.voids = suggestion; end
61
62 % Enter aquisition frequency
63 if i == 1, suggestion = 250; else, suggestion = sample.layer(
       i-1).patterns.frequency; end
64 sample.layer(i).patterns.frequency = input(['Enter detector
       aquisition frequency - suggestion:', num2str(suggestion,'
       %5.2f') '\n']);
65 if isempty(sample.layer(i).patterns.frequency), sample.layer(
       i).patterns.frequency = suggestion; end
66
67 % Enter aquisition period
```

```
68 if i == 1, suggestion = 0.3; else, suggestion = sample.layer(
       i-1).patterns.aqperiod*1e3; end
69 sample.layer(i).patterns.aqperiod = input(['Enter detector
       aquisition period - suggestion:', num2str(suggestion,'%5.2
       f') 'ms \n'])*1e-3;
70 if isempty(sample.layer(i).patterns.aqperiod), sample.layer(i
       ).patterns.aqperiod = suggestion*1e-3; end
71
72 % Powder
73 if i == 1, suggestion = 'SS316L'; else, suggestion = sample.
       layer(i-1).powder; end
74 sample.layer(i).powder = input(['Enter powder - suggestion:',
        suggestion '\n']);
75 if isempty(sample.layer(i).powder), sample.layer(i).powder =
       suggestion; end
76
77 % Layer thickness
78 if i == 1, suggestion = 25; else, suggestion = sample.layer(i
       -1).thickness*1e6; end
79 sample.layer(i).thickness = input(['Enter layer thickness -
       suggestion:', num2str(suggestion,'%5.2f') 'um \n'])*1e-6;
80 if isempty(sample.layer(i).thickness), sample.layer(i).
       thickness = suggestion*1e-6; end
81
```

```
82 % Laser power
83 if i == 1, suggestion = 200; else, suggestion = sample.layer(
       i-1).laser.power; end
84 sample.layer(i).laser.power = input(['Enter laser power -
       suggestion:', num2str(suggestion,'%5.2f') ' W \n']);
85 if isempty(sample.layer(i).laser.power), sample.layer(i).
       laser.power = suggestion; end
86
87 % Laser speed
88 if i == 1, suggestion = 400; else, suggestion = sample.layer(
       i-1).laser.speed*1e3; end
89 sample.layer(i).laser.speed = input(['Enter laser speed -
       suggestion:', num2str(suggestion,'%5.2f') 'mm/s \n'])*1e
       -3;
90 if isempty(sample.layer(i).laser.speed), sample.layer(i).
       laser.speed = suggestion*1e-3; end
91
92 % Laser direction
93 if i == 1, suggestion = -1; else, suggestion = sample.layer(i
       -1).laser.direction; end
94 sample.layer(i).laser.direction = input(['Enter laser beam
       direction - suggestion:', num2str(suggestion,'%5.2f') '\n'
       ]);
```

```
95 if isempty(sample.layer(i).laser.direction), sample.layer(i).
       laser.direction = suggestion; end
96
97 % X-ray beam size
98 if i == 1, suggestion = 50; else, suggestion = sample.layer(i
       -1).beam.size.y*1e6; end
99 sample.layer(i).beam.size.y = input(['Enter X-Ray beam size (
       Y) - suggestion:', num2str(suggestion,'%5.2f') 'um \n'])*1
       e-6;
100 if isempty(sample.layer(i).beam.size.y), sample.layer(i).beam
       .size.y = suggestion*1e-6; end
101 if i == 1, suggestion = 20; else, suggestion = sample.layer(i
       -1).beam.size.z*1e6; end
102 sample.layer(i).beam.size.z = input(['Enter X-Ray beam size (
       Z) - suggestion:', num2str(suggestion,'%5.2f') 'um \n'])*1
       e-6;
103 if isempty(sample.layer(i).beam.size.z), sample.layer(i).beam
       .size.z = suggestion*1e-6; end
104
105 % X-ray beam position
106 if i == 1, suggestion = 0; else, suggestion = sample.layer(i
       -1).beam.position.y*1e6; end
```

```
107 sample.layer(i).beam.position.y = input(['Enter X-Ray beam
    position (Y) - suggestion:', num2str(suggestion,'%5.2f') '
    um \n'])*1e-6;
108 if isempty(sample.layer(i).beam.position.y), sample.layer(i).
    beam.position.y = suggestion*1e-6; end
109 if i == 1, suggestion = -40; else, suggestion = sample.layer(
    i-1).beam.position.z*1e6; end
110 sample.layer(i).beam.position.z = input(['Enter X-Ray beam
    position (Z) - suggestion:', num2str(suggestion,'%5.2f') '
    um \n'])*1e-6;
111 if isempty(sample.layer(i).beam.position.z), sample.layer(i).
    beam.position.z = suggestion*1e-6; end
112 end
113
114 function sample = layer_sort(sample,fnfig)
115 % th = sample.layer(1).data(1).th;
116 % phi = (sample.layer(1).data(1).phi).';
117 % [phi,idx] = sort(phi(:,1));
118 % for i = 1:length(sample.layer)
119 %     sample.layer(i).processed1d.int = zeros(length(th),
    length(sample.layer(i).data));
120 %     for j = 1:length(sample.layer(i).data)
121 %         sample.layer(i).data(i).phi = phi;
```

```
122 %           sample.layer(i).processed1d.y0(j) = sample.layer(i)
    .data(j).y0;
123 %           sample.layer(i).processed1d.z0(j) = sample.layer(i)
    .data(j).z0;
124 %           sample.layer(i).processed1d.int(:,j) = sample.layer
    (i).data(j).int1d;
125 %           sample.layer(i).processed2d.y0(j) = sample.layer(i)
    .data(j).y0;
126 %           sample.layer(i).processed2d.z0(j) = sample.layer(i)
    .data(j).z0;
127 %       end
128 %       sample.layer(i).processed2d.int = zeros(length(th),
    length(sample.layer(i).data),length(phi));
129 %       for k = 1:length(phi)
130 %           for j = 1:length(sample.layer(i).data)
131 %               sample.layer(i).processed2d.int(:,j,k) = sample
    .layer(i).data(j).int2d(:,k);
132 %           end
133 %       end
134 %       sample.layer(i).processed2d.int = sample.layer(i).
    processed2d.int(:,:,idx);
135 %       intbar = nanmean(sample.layer(i).processed1d.int(:,end
    -100:end),2);
136 %       intdiv = sample.layer(i).processed1d.int./intbar;
```

```
137 %     sumint = nansum(intdiv(750:1000,:),1);
138 %     [~,I] = max(sumint);
139 %     y00 = sample.layer(i).processed1d.y0(I);
140 %     sample.layer(i).processed2d.y0 =  sample.layer(i).
    processed2d.y0-y00;
141 %     sample.layer(i).processed2d.seperated = nanmean(sample.
    layer(i).processed2d.int(:,:,[find(phi==pi),find(phi==2*pi
    )]),3);
142 %     sample.layer(i).processed2d.together = nanmean(sample.
    layer(i).processed2d.int(:,:,[find(phi==pi/2),find(phi==3*
    pi/2)]),3);
143 %     set(0,'defaulttextInterpreter','latex') %latex axis
    labels
144 %     set(groot,'defaulttextinterpreter','latex');
145 %     set(groot, 'defaultAxesTickLabelInterpreter','latex');
146 %     set(groot, 'defaultLegendInterpreter','latex');
147 %     set(groot,'DefaultFigureColormap',jet);
148 %     dim = [0.6 0.6 0.3 0.3];
149 %     str = {sample.layer(i).powder,...
150 %         ['Layer = ' num2str(sample.layer(i).number)],...
151 %         ['P = ' num2str(sample.layer(i).laser.power,'%5.1f
    ') ' W'],...
152 %         ['v = ' num2str(sample.layer(i).laser.speed*1e3) '
    mm/s'],...
```

```
153 %           ['t = ' num2str(sample.layer(i).thickness*1e6) ' \
    mum'],...
154 %           ['z_0 = ' num2str(sample.layer(i).beam.position.z*1
    e6) ' \mum']};
155 %       h(1) = figure;
156 %       contourf(rad2deg(2*th),sample.layer(i).processed2d.y0*1
    e3,sample.layer(i).processed1d.int.^(1/2).',40,'LineStyle
    ','none');
157 %       xlim([4,16])
158 %       ylim([-0.005*1e3,0.01*1e3])
159 %       xlabel('$2\theta$ $deg.$','FontSize',14)
160 %       ylabel('$y_0$ $mm$','FontSize',14)
161 %       caxis manual
162 %       caxis([0,4]);
163 %       cb = colorbar;
164 %       cb.Label.String = '$\surd{I}$';
165 %       cb.TickLabelInterpreter = 'latex';
166 %       cb.Label.Interpreter = 'latex';
167 %       cb.Label.FontSize = 14;
168 %       cb.Box = 'off';
169 %       annotation('textbox',dim,'String',str,'FitBoxToText','
    on','BackgroundColor','w');
170 %       h(2) = figure;
```

```
171 %     contourf(rad2deg(2*th),rad2deg(phi),squeeze(sample.
    layer(i).processed2d.int(:,end,:)).^(1/2).',40,'LineStyle
    ','none')
172 %     xlim([4,16])
173 %     xlabel('$2\theta$ $deg.$','FontSize',14)
174 %     ylabel('$\phi$ $deg.$','FontSize',14)
175 %     caxis manual
176 %     caxis([0,4]);
177 %     cb = colorbar;
178 %     cb.Label.String = '$\surd{I}$';
179 %     cb.TickLabelInterpreter = 'latex';
180 %     cb.Label.Interpreter = 'latex';
181 %     cb.Label.FontSize = 14;
182 %     cb.Box = 'off';
183 %     annotation('textbox',dim,'String',str,'FitBoxToText','
    on','BackgroundColor','w');
184 %     h(3) = figure;
185 %     contourf(rad2deg(2*th),rad2deg(phi),squeeze(sample.
    layer(i).processed2d.int(:,end,:)).^(1/2).',40,'LineStyle
    ','none')
186 %     xlim([5.5,6])
187 %     xlabel('$2\theta$ $deg.$','FontSize',14)
188 %     ylabel('$\phi$ $deg.$','FontSize',14)
189 %     caxis manual
```

```
190 %       caxis([0,4]);
191 %       cb = colorbar;
192 %       cb.Label.String = '$\surd{I}$';
193 %       cb.TickLabelInterpreter = 'latex';
194 %       cb.Label.Interpreter = 'latex';
195 %       cb.Label.FontSize = 14;
196 %       cb.Box = 'off';
197 %       annotation('textbox',dim,'String',str,'FitBoxToText','
    on','BackgroundColor','w');
198 %       h(4) = figure;
199 %       contourf(rad2deg(2*th),sample.layer(i).processed2d.y0*1
    e3,sample.layer(i).processed2d.seperated.^(1/2).',40,'
    LineStyle','none')
200 %       xlim([4,11])
201 %       ylim([-0.01*1e3,0.04*1e3])
202 %       xlabel('$2\theta$ $deg.$','FontSize',14)
203 %       ylabel('$y_0$ $mm$','FontSize',14)
204 %       caxis manual
205 %       caxis([0,4]);
206 %       cb = colorbar;
207 %       cb.Label.String = '$\surd{I_{(\phi=180^{\circ},\phi
    =360^{\circ})}}$';
208 %       cb.TickLabelInterpreter = 'latex';
209 %       cb.Label.Interpreter = 'latex';
```

```
210 %       cb.Label.FontSize = 14;
211 %       cb.Box = 'off';
212 %       annotation('textbox',dim,'String',str,'FitBoxToText','
    on','BackgroundColor','w');
213 %       h(5) = figure;
214 %       contourf(rad2deg(2*th),sample.layer(i).processed2d.y0*1
    e3,sample.layer(i).processed2d.together.^(1/2).',40,'
    LineStyle','none')
215 %       xlim([4,11])
216 %       ylim([-0.01*1e3,0.04*1e3])
217 %       xlabel('$2\theta$ $deg.$','FontSize',14)
218 %       ylabel('$y_0$ $mm$','FontSize',14)
219 %       caxis manual
220 %       caxis([0,4]);
221 %       cb = colorbar;
222 %       cb.Label.String = '$\surd{I_{(\phi=90^{\circ},\phi
    =270^{\circ})}}$';
223 %       cb.TickLabelInterpreter = 'latex';
224 %       cb.Label.Interpreter = 'latex';
225 %       cb.Label.FontSize = 14;
226 %       cb.Box = 'off';
227 %       annotation('textbox',dim,'String',str,'FitBoxToText','
    on','BackgroundColor','w');
```

```
228 %       savefig(h,[fnfig '_L' num2str(sample.layer(i).number)
        '.fig'],'compact');
229 %       close(h);
230 % end
231 th = sample.layer(1).data(1).th;
232 phi = (sample.layer(1).data(1).phi).';
233 [phi,idx] = sort(phi(:,1));
234 for i = 1:length(sample.layer)
235     sample.layer(i).processed1d.int = zeros(length(th),length
          (sample.layer(i).data));
236     for j = 1:length(sample.layer(i).data)
237         sample.layer(i).data(i).phi = phi;
238         sample.layer(i).processed1d.y0(j) = sample.layer(i).
              data(j).y0;
239         sample.layer(i).processed1d.z0(j) = sample.layer(i).
              data(j).z0;
240         sample.layer(i).processed1d.int(:,j) = sample.layer(i
              ).data(j).int1d;
241         sample.layer(i).processed2d.y0(j) = sample.layer(i).
              data(j).y0;
242         sample.layer(i).processed2d.z0(j) = sample.layer(i).
              data(j).z0;
243     end
```

```
244     sample.layer(i).processed2d.int = zeros(length(th),length
            (sample.layer(i).data),length(phi));
245     for k = 1:length(phi)
246         for j = 1:length(sample.layer(i).data)
247             sample.layer(i).processed2d.int(:,j,k) = sample.
                    layer(i).data(j).int2d(:,k);
248         end
249     end
250     sample.layer(i).processed2d.int = sample.layer(i).
            processed2d.int(:,:,idx);
251 %     y00 = (0.014642857142857*sample.layer(i).laser.speed
    +0.204667857142857)*sample.layer(i).laser.speed;
252 %     sample.layer(i).processed1d.y0 =  sample.layer(i).
    processed1d.y0-y00;
253     set(0,'defaulttextInterpreter','latex') %latex axis
            labels
254     set(groot,'defaulttextinterpreter','latex');
255     set(groot, 'defaultAxesTickLabelInterpreter','latex');
256     set(groot, 'defaultLegendInterpreter','latex');
257     set(groot,'DefaultFigureColormap',winter);
258     dim = [0.8  0.6  0.3  0.3];
259     str = {sample.layer(i).powder,...
260         ['Layer = ' num2str(sample.layer(i).number)],...
```

```
261             ['P = ' num2str(sample.layer(i).laser.power,'%5.1f')
                    ' W'],...
262             ['v = ' num2str(sample.layer(i).laser.speed*1e3) ' mm
                    /s'],...
263             ['t = ' num2str(sample.layer(i).thickness*1e6) ' \mum
                    '],...
264             ['z_0 = ' num2str(sample.layer(i).beam.position.z*1e6
                    ) ' \mum']};
265         h(1) = figure;
266         waterfall(rad2deg(2*th),sample.layer(i).processed1d.y0*1
                e3,sample.layer(i).processed1d.int.');
267         xlabel('$2\theta$ $deg.$','FontSize',14)
268         ylabel('$y_0$ $(v.t)$ $mm$','FontSize',14)
269         annotation('textbox',dim,'String',str,'FitBoxToText','on'
                ,'BackgroundColor','w');
270         view(15,70);
271         savefig(h,[fnfig '_L' num2str(sample.layer(i).number) '.
                fig'],'compact');
272         close(h);
273     end
274     th = sample.layer(1).data(1).th;
275     positions = zeros(length(sample.layer),1);
276     for i = 1:length(sample.layer)
277         positions(i,1) = sample.layer(i).beam.position.y;
```

```
278 end
279 [positions,ia,~] = unique(round(positions,6),'sorted');
280 end
```

A.2 MATLAB Script and Function to Open and Plot data for each file

The following code was modified from the code by Dr. Samuel Clarke to open `intermediate_samplev400.mat` and plot the data using the plotting function frameplot2D.m (shown below the following script). `Frameplot2D.m` plotted each frame in its respective layer's sequence and saved each frame as a .tiff file. This allowed the frames for a given layer to be opened in software such as ImageJ and watch as a sequence.

```
1  % January 11th, 2019
2  % 2D plots with peaks
3  load ('intermediate_sample_v400.mat')
4
5  for i = 3:length(dn)
6      d = dir([dn(i).folder '\' dn(i).name '/P3/*.mat']);
7      if length(d) > 1
8          fprintf('\r %s    \n',[dn(i).name]);
9          sample2=frameplot2D(sample, [dn(i).folder '\' dn(i).
               name],length(sample.layer))
10     end
```

```
11 end

1  function sample=frameplot2D(sample,fnfig,layernum)
2
3  set(0,'defaulttextInterpreter','latex') %latex axis labels
4  set(groot,'defaulttextinterpreter','latex');
5  set(groot, 'defaultAxesTickLabelInterpreter','latex');
6  set(groot, 'defaultLegendInterpreter','latex');
7  set(groot,'DefaultFigureColormap',jet);
8
9  th = [sample.layer(1).data(1).th];
10
11 for m =1:length(sample.layer)
12         % SEQUENCE OF IMAGES
13         Imax=1.5; % maximum I axis limit on th vs Y plots
14         linew=1; % line width
15         % define your peaks
16         load ('Ti185peaksESRF.mat')
17
18         % define t, where t=0 is when shutter opens.
19         t=-48:4:948; % time in ms, normal plotting.
20
21         % Plot sequence
22         for j=1:length(t)
23             k=figure
```

```
24          % Plot XRD plot
25          Intensity=sample.layer(m).processed1d.int(:,j);
26          % Plot your peaks
27
28          % alpha-Ti
29          for theta=1:1:length(aTi)
30              diffprev=90;
31              for q=1:length(th)
32                  diff=abs(aTi(theta,1)-(rad2deg(2*th(q))))
                        ;
33                  if diff<diffprev
34                      diffprev=diff;
35                      peakindex=q;
36                  else;
37                  end
38              end
39              line([aTi(theta,1) aTi(theta,1)], [0
                    Intensity(peakindex)], 'Color', 1/255*[255
                     128 0], 'LineStyle', '-','LineWidth',
                    linew)
40          end
41
42          %beta-Ti
43          hold on
```

```
44              for theta=1:1:length(bTi)
45                  diffprev=90;
46                  for q=1:length(th)
47                      diff=abs(bTi(theta,1)-(rad2deg(2*th(q))))
                            ;
48                      if diff<diffprev
49                          diffprev=diff;
50                          peakindex=q;
51                      else;
52                      end
53                  end
54                 line([bTi(theta,1) bTi(theta,1)], [0 Intensity
                       (peakindex)], 'Color', 1/255*[0,0,235], '
                       LineStyle', '-','LineWidth',linew)
55              end
56
57              % Fe
58              ylimit=2.5;
59              hold on
60              for theta=1:1:length(Fe)
61                  diffprev=90;
62                  for q=1:length(th)
63                      diff=abs(Fe(theta,1)-(rad2deg(2*th(q))));
64                      if diff<diffprev
```

```
65                          diffprev=diff;
66                          peakindex=q;
67                      else;
68                      end
69                  end
70                  line([Fe(theta,1) Fe(theta,1)], [0 Intensity(
                        peakindex)], 'Color', 'red', 'LineStyle',
                        '-','LineWidth',linew)
71              end
72              % Al3V7
73              %ylimit=2.5;
74              ylimit=2;
75              hold on
76              for theta=1:1:length(Al3V7)
77                  diffprev=90;
78                  for q=1:length(th)
79                      diff=abs(Al3V7(theta,1)-(rad2deg(2*th(q))
                            ));
80                      if diff<diffprev
81                          diffprev=diff;
82                          peakindex=q;
83                      else;
84                      end
85                  end
```

```
86                  line([Al3V7(theta,1) Al3V7(theta,1)], [0
                        Intensity(peakindex)], 'Color', 1/255*[3
                        192 60], 'LineStyle', '-','LineWidth',
                        linew)
87              end
88              % TiC
89              %ylimit=2.5;
90              ylimit=2;
91              hold on
92              for theta=1:1:length(TiC)
93                  diffprev=90;
94                  for q=1:length(th)
95                      diff=abs(TiC(theta,1)-(rad2deg(2*th(q))))
                            ;
96                      if diff<diffprev
97                          diffprev=diff;
98                          peakindex=q;
99                      else;
100                     end
101                 end
102                 line([TiC(theta,1) TiC(theta,1)], [0
                        Intensity(peakindex)], 'Color', 1/255*[225
                         0 225], 'LineStyle', '-','LineWidth',
                        linew)
```

```
103             end
104
105             hold on
106             %Plot diffraction data
107             plot(rad2deg(2*th),Intensity, 'k-','LineWidth',1)
108             xlabel(['2$\theta$ ($^{\circ}$)'],'FontSize',36)
                   % normally it's 14
109             ylabel('Intensity','FontSize',36,'Color', [0 0
                   0])
110             % GRAPH FEATURES
111             set(gca,'XMinorTick','on','FontSize',36)
112             xlim([3.5 7.5])
113             ylim ([0 Imax])
114             title ([num2str(t(j)) ' ms'],'Interpreter', '
                   latex','FontName','Default','FontSize',36)
115             set(gcf, 'Position', [470,-71,1536,1007])
116             saveas(k,[fnfig '\L_' num2str(m) '\' num2str(j) '
                   .tiff']);
117             close(k);
118             end
119 end
120
121 end
```

Appendix B

Conversion of Infrared Images to Temperature Fields

Appendix B shows the files made by Dr. Samuel Clarke which converted IR images to temperature fields. They utilize the following functions (in the order in which they are listed below): `Load_Stack.m`, `I2T.m`, `pw_RollingShutter.m`, `prune.m` and `regrid.m`. The following is the parent script in which the functions were used:

```
clear all; close all; clc;
I = Load_Stack;
data = I2T(I,0.4,2.60128E+07,9.29823E-07,-7.81551E-05,2.66508
    E-02,102);
[data] = pw_RollingShutter(data);
[data] = prune(data);
data = re_grid(data);

```

```
beam_velocity = 100; % 100 mm/s
fp = 1603.5; % frame rate
scale = beam_velocity/(nanmean(data.shutter.v)*fp);

figure()
contourf(data.gridded.m(:,:)*scale,data.gridded.n(:,:)*scale,
    data.gridded.meanT(:,:));
axis('equal')
colorbar

figure()
contourf(data.gridded.m(:,:)*scale,data.gridded.n(:,:)*scale,
    data.gridded.T(:,:,10));
axis('equal')
colorbar
```

`Load_Stack.m`, as shown below, inputs IR images into MATLAB.

```
function I = Load_Stack
dn = dir('input');
d = dir([dn(1).folder '\' dn(1).name '/*.tif']);
frame1 = double(imread([d(1).folder '\' d(1).name]));
imsize = size(frame1);
I = zeros(imsize(1),imsize(2),length(d));
for k = 1:length(d)
    fn = [dn(1).folder '\' d(k).name];
```

```
9       I(:,:,k) = imread(fn);
10  end
```

I2T.m, as shown below, converts the IR images to temperature fields.

```
1   function data = I2T(I,epsilon,A0,A1,A2,A3,Dark)
2   % S Clark 13/09/2018
3   % Funtion to tansform an image with pixel values [I] to a
        corresponding
4   % [T]emperature field in Kelvin.
5
6   % A0 = 2.60128E+07; % Sakuma Hattori parameter
7   % A1 = 9.29823E-07; % Sakuma Hattori parameter
8   % A2 = -7.81551E-05; % Sakuma Hattori parameter
9   % A3 = 2.66508E-02; % Sakuma Hattori parameter
10  % epsilon = 0.35; % Surface Emmisivity
11  % Dark = 102; % Median dark-field value of detector
12
13  % Bit = 16; $ Bit size of the image for testing
14  % I = (1:1:2^Bit); % Generates pixel levels for testing
15
16  % Calculation of the Inverse Sakuma Hattori equation
17  % syms c2 A0 A1 A2 A3 I T eps K
18  % Sakuma_Hattori = (epsilon*A0)/(exp(c2/(A1*T+A2+A3/T))-1) ==
        I
19  % Inv_Sakuma_Hattori = solve(Sakuma_Hattori,T)
```

```
% term = log((I + A0*epsilon)/I) % Repeated term extracted
    from inspection
% Inv_Sakuma_Hattori = simplify(subs(Inv_Sakuma_Hattori(2),
    term,K))
% Correct root is the positive
c2 = 1.43877736e-2; % Second radiation constant (m K)
% [https://physics.nist.gov/cgi-bin/cuu/Value?c22ndrc]
I = double(I);
data.I2T.I = I;
I = I-Dark; I(I<0) = NaN;
K = log((I+A0*epsilon)./I);
T = ((c2+(A2^2*K.^2-2*A2*K*c2-4*A1*A3*K.^2+c2^2).^(1/2)-(A2*K
    )))./(2*A1*K);
data.I2T.T = T; data.I2T.A0 = A0; data.I2T.A1 = A1; data.I2T.
    A2 = A2;
data.I2T.A3 = A3; data.I2T.emissivity = epsilon; data.I2T.
    dark = Dark;
end
```

`pw_RollingShutter.m`, as shown below, corrects the distortion in the IR images by assuming that the velocity of the laser is constant, and modifying the spatial coordinates such that it is constant. The centre of the laser beam is set to be the origin in each frame.

```
function [data] = pw_RollingShutter(data)
% S Clark 17/10/2018
```

```
% scale = 4.3532e-6;
% fp = 1603.5;
% Funtion to calculated the distortion due to the rolling
    shutter error
% The funtion determins the [v]elocity in pixels per frame of
     the laser
% through a simple detection algorithm. The spatial
    cooridinates are
% returned for the old and the new corrected coordinates of
    each pixel in
% the image [stack].
% Define the origional x and y cooradinates of pixels
T = data.I2T.T;
[m,n] = meshgrid(1:size(T,2),1:size(T,1));
% Determine [t]ime matrix for the pixel aquisition time of a
    frame
t = zeros(size(n));
t(size(n,1)/2+1:end,:) = 2*n(1:size(n,1)/2,:)/size(n,1);
t(1:size(n,1)/2,:) = 2*flipud(n(1:size(n,1)/2,:))/...
    size(n,1);
% Coarse extraction of the centrod of the laser beam
centroids = [];
for i = 1:size(T,3)
    Tmed = medfilt2(T(:,:,i),[3,3]);
```

```
22      M = max(Tmed(:));
23      [In,Im]=ind2sub(size(Tmed),find(Tmed == M));
24      Im = round(nanmean(Im)); In = round(nanmean(In));
25      if isnan(Im*In) == 0
26          centroids = cat(1,centroids,[i,m(In,Im),n(In,Im),t(In
                ,Im)+...
27              (i-1),M]);
28      end
29  end
30  % Filter centroids
31  idx = (centroids(:,5)>max(centroids(:,5))-(max(centroids(:,5)
        )-...
32      min(centroids(:,5)))*0.25);
33  centroids = centroids(idx,:);
34  % determine velocity of laser verticall and horizontally and
        determine new
35  % coordinate matrices
36  data.shutter.dm = zeros(size(T)); data.shutter.dn = zeros(
        size(T));
37  data.shutter.v = zeros(size(T,3),1);
38  data.shutter.theta = zeros(size(T,3),1);
39  for i = centroids(1,1):centroids(end,1)
40      % select the 5 nearest neighbors to determine velocities
41      idx = sort(knnsearch(centroids(:,4),i,'K',5));
```

```
42      pm = polyfit(centroids(idx,4),centroids(idx,2),1);
43      pn = polyfit(centroids(idx,4),centroids(idx,3),1);
44      data.shutter.v(i) = (pm(1)^2+pn(1)^2)^(1/2); % Detected
            laser velocity
45      data.shutter.theta(i) = wrapTo2Pi(atan2(pn(1),pm(1)));
46      data.shutter.dm(:,:,i) = ((1-t)*pm(1))-polyval(pm,i);
47      data.shutter.dn(:,:,i) = ((1-t)*pn(1))-polyval(pn,i);
48  end
49  data.shutter.m = m+data.shutter.dm;
50  data.shutter.n = n+data.shutter.dn;
51  end
```

`prune.m`, as shown below, removes frames without the centre of the laser beam present in them.

```
1  function [data] = prune(data)
2  retain = data.shutter.v.^2 > 0;
3  data.shutter.dm = data.shutter.dm(:,:,retain);
4  data.shutter.dn = data.shutter.dn(:,:,retain);
5  data.shutter.m = data.shutter.m(:,:,retain);
6  data.shutter.n = data.shutter.n(:,:,retain);
7  data.shutter.v = data.shutter.v(retain);
8  data.shutter.theta = data.shutter.theta(retain);
9  data.I2T.I = data.I2T.I(:,:,retain);
10 data.I2T.T = data.I2T.T(:,:,retain);
11 end
```

`regrid.m`, as shown below, averages the frames from a single laser pass.

```
function data = re_grid(data)
T = data.I2T.T;
%Generate m and n
[m,n] = meshgrid(1:size(T,2),1:size(T,1));
% linear summation of contributions
m = m+data.shutter.dm;
n = n+data.shutter.dn;
[m_out,n_out] = meshgrid(round(min(m(:))):round(max(m(:)))
    ,...
     round(min(n(:))):round(max(n(:))));
T_out = zeros(size(m_out,1),size(m_out,2),size(T,3));
parfor i = 1:size(T,3)
    X = m(:,:,i); Y = n(:,:,i); V = T(:,:,i);
    F = scatteredInterpolant(X(:),Y(:),V(:));
    F.Method = 'natural'; F.ExtrapolationMethod = 'none';
    T_out(:,:,i) = F(m_out,n_out);
end
data.gridded.T = T_out;
data.gridded.m = m_out;
data.gridded.n = n_out;
data.gridded.meanT = nanmean(data.gridded.T,3);
end
```

Bibliography

[1] F. Calignano, D. Manfredi, E. P. Ambrosio, S. Biamino, M. Lombardi, E. Atzeni, A. Salmi, P. Minetola, L. Iuliano, and P. Fino, "Overview on additive manufacturing technologies," *Proceedings of the IEEE*, vol. 105, no. 4, pp. 593–612, 2017.

[2] M. Bal, "High Level Processes: Directed Energy Deposition," 2017.

[3] M. Molitch-Hou, "Overview of additive manufacturing process," in *Additive Manufacturing: Materials, Processes, Quantifications and Applications* (J. Zhang and Y.-G. Jung, eds.), p. 11, Cambridge, MA: Butterworth-Heinemann, 2018.

[4] I. Polozov, V. Sufiiarov, A. Kantyukov, and A. Popovich, "Selective Laser Melting of Ti2AlNb-based intermetallic alloy using elemental powders: Effect of process parameters and post-treatment on microstructure, composition, and properties," *Intermetallics*, vol. 112, p. 106554, 2019.

[5] M. Moorehead, K. Bertsch, M. Niezgoda, C. Parkin, M. Elbakhshwan, K. Sridharan, C. Zhang, D. Thoma, and A. Couet, "High-throughput synthesis of Mo-Nb-Ta-W high-entropy alloys via additive manufacturing," *Materials and Design*, vol. 187, p. 108358, 2020.

[6] Q. Wang, L. Ren, X. Li, S. Zhang, T. B. Sercombe, and K. Yang, "Antimicrobial Cu-bearing stainless steel scaffolds," *Materials Science and Engineering C*, vol. 68, pp. 519–522, 2016.

[7] P. Chen, S. Li, Y. Zhou, M. Yan, and M. M. Attallah, "Fabricating CoCrFeMnNi high entropy alloy via selective laser melting in-situ alloying," *Journal of Materials Science and Technology*, vol. 43, pp. 40–43, 2020.

[8] K. I. Schwendner, R. Banerjee, P. C. Collins, C. A. Brice, and H. L. Fraser, "Direct laser deposition of alloys from elemental powder blends," *Scripta Materialia*, vol. 45, pp. 1123–1129, 2001.

[9] C. Wang, X. P. Tan, Z. Du, S. Chandra, Z. Sun, C. W. J. Lim, S. B. Tor, C. S. Lim, and C. H. Wong, "Additive manufacturing of NiTi shape memory alloys using pre-mixed powders," *Journal of Materials Processing Technology*, vol. 271, pp. 152–161, 2019.

[10] H. Chen, X. Zi, Y. Han, J. Dong, S. Liu, and C. Chen, "Microstructure and mechanical properties of additive manufactured W-Ni-Fe-Co composite produced by selective laser melting," *International Journal of Refractory Metals and Hard Materials*, vol. 86, p. 105111, 2020.

[11] H. Dobbelstein, M. Thiele, E. L. Gurevich, E. P. George, and A. Ostendorf, "Direct metal deposition of refractory high entropy alloy MoNbTaW," *Physics Procedia*, vol. 83, pp. 624–633, 2016.

[12] S. J. Clark, C. L. Leung, Y. Chen, L. Sinclair, S. Marussi, and P. D. Lee, "Capturing Marangoni flow via synchrotron imaging of selective laser melting," *IOP Conference Series: Materials Science and Engineering*, vol. 861, p. 012010, 2020.

[13] L. Yan, X. Chen, W. Li, J. Newkirk, and F. Liou, "Direct laser deposition of Ti-6Al-4V from elemental powder blends," *Rapid Prototyping Journal*, vol. 22, no. 5, pp. 810–816, 2016.

[14] N. Kang, X. Lin, M. E. Mansori, Q. Z. Wang, J. L. Lu, C. Coddet, and W. D. Huang, "On the effect of the thermal cycle during the directed energy deposition application to the in-situ production of a Ti-Mo alloy functionally graded structure," *Additive Manufacturing*, vol. 31, p. 100911, 2020.

[15] E. G. Brodie, A. E. Medvedev, J. E. Frith, M. S. Dargusch, H. L. Fraser, and A. Molotnikov, "Remelt processing and microstructure of selective laser melted Ti25Ta," *Journal of Alloys and Compounds*, vol. 820, p. 153082, 2020.

[16] M. Simonelli, N. T. Aboulkhair, P. Cohen, J. W. Murray, A. T. Clare, C. Tuck, and R. J. Hague, "A comparison of Ti-6Al-4V in-situ alloying in Selective Laser Melting using simply-mixed and satellited powder blend feedstocks," *Materials Characterization*, vol. 143, pp. 118–126, 2018.

[17] J. Epp, J. Dong, H. Meyer, and A. Bohlen, "Analysis of cyclic phase transformations during additive manufacturing of hardenable tool steel by in-situ X-ray diffraction experiments," *Scripta Materialia*, vol. 177, pp. 27–31, 2020.

[18] C. Zhao, K. Fezzaa, R. W. Cunningham, H. Wen, F. De Carlo, L. Chen, A. D.

Rollett, and T. Sun, "Real-time monitoring of laser powder bed fusion process using high-speed X-ray imaging and diffraction," *Scientific Reports*, vol. 7, p. 3602, 2017.

[19] R. P. Kolli and A. Devaraj, "A Review of Metastable Beta Titanium Alloys," *Metals*, vol. 8, no. 7, p. 506, 2018.

[20] H. Azizi, H. Zurob, B. Bose, S. R. Ghiaasiaan, X. Wang, S. Coulson, V. Duz, and A. B. Phillion, "Additive manufacturing of a novel Ti-Al-V-Fe alloy using selective laser melting," *Additive Manufacturing*, vol. 21, pp. 529–535, 2018.

[21] K. C. Mills, "Titanium," in *Recommended values of thermophysical properties for selected commercial alloys*, pp. 211–217, Cambridge, England: Woodhead Publishing Ltd., 2002.

[22] Fortune Business Insights, "3D Printing Market Size, Share & Industry Analysis, By Component (Hardware, Software, and Services), By Technology (Fused Deposition Modeling, Selective Laser Sintering, Stereolithography, Direct Metal Laser Sintering, PolyJet, Multi Jet Fusion (MJF), Oth," tech. rep., 2020.

[23] T. Duda and L. V. Raghavan, "3D metal printing technology: the need to reinvent design practice," *AI and Society*, vol. 33, pp. 241–252, 2018.

[24] T. J. Horn and O. L. Harrysson, "Overview of current additive manufacturing technologies and selected applications," *Science Progress*, vol. 95, no. 3, pp. 255–282, 2012.

[25] D. D. Gu, W. Meiners, K. Wissenbach, and R. Poprawe, "Laser additive manufacturing of metallic components: Materials, processes and mechanisms," *International Materials Reviews*, vol. 57, no. 3, pp. 133–164, 2012.

[26] Y. Ding, M. Akbari, and R. Kovacevic, "Process planning for laser wire-feed metal additive manufacturing system," *International Journal of Advanced Manufacturing Technology*, vol. 95, pp. 355–365, 2018.

[27] P. A. Hooper, "Melt pool temperature and cooling rates in laser powder bed fusion," *Additive Manufacturing*, vol. 22, pp. 548–559, 2018.

[28] G. Boussinot, M. Apel, J. Zielinski, U. Hecht, and J. H. Schleifenbaum, "Strongly Out-of-Equilibrium Columnar Solidification During Laser Powder-Bed Fusion in Additive Manufacturing," 2019.

[29] W. J. Sames, F. A. List, S. Pannala, R. R. Dehoff, and S. S. Babu, "The metallurgy and processing science of metal additive manufacturing," *International Materials Reviews*, vol. 61, no. 5, pp. 315–360, 2016.

[30] D. Bourell, J. P. Kruth, M. Leu, G. Levy, D. Rosen, A. M. Beese, and A. Clare, "Materials for additive manufacturing," *CIRP Annals - Manufacturing Technology*, vol. 66, pp. 659–681, 2017.

[31] A. Grigoriev, I. Polozov, V. Sufiiarov, and A. Popovich, "In-situ synthesis of Ti2AlNb-based intermetallic alloy by selective laser melting," *Journal of Alloys and Compounds*, vol. 704, pp. 434–442, 2017.

[32] I. Polozov, V. Sufiiarov, A. Popovich, D. Masaylo, and A. Grigoriev, "Synthesis of Ti-5Al, Ti-6Al-7Nb, and Ti-22Al-25Nb alloys from elemental powders using

powder-bed fusion additive manufacturing," *Journal of Alloys and Compounds*, vol. 763, pp. 436–445, 2018.

[33] H. Schönrath, M. Spasova, S. O. Kilian, R. Meckenstock, G. Witt, J. T. Sehrt, and M. Farle, "Additive manufacturing of soft magnetic permalloy from Fe and Ni powders: Control of magnetic anisotropy," *Journal of Magnetism and Magnetic Materials*, vol. 478, pp. 274–278, 2019.

[34] V. Fallah, S. F. Corbin, and A. Khajepour, "Process optimization of Ti-Nb alloy coatings on a Ti-6Al-4V plate using a fiber laser and blended elemental powders," *Journal of Materials Processing Technology*, vol. 210, pp. 2081–2087, 2010.

[35] J. C. Wang, Y. J. Liu, P. Qin, S. X. Liang, T. B. Sercombe, and L. C. Zhang, "Selective laser melting of Ti–35Nb composite from elemental powder mixture: Microstructure, mechanical behavior and corrosion behavior," *Materials Science and Engineering A*, vol. 760, pp. 214–224, 2019.

[36] S. L. Sing, F. E. Wiria, and W. Y. Yeong, "Selective laser melting of titanium alloy with 50 wt% tantalum: Effect of laser process parameters on part quality," *International Journal of Refractory Metals and Hard Materials*, vol. 77, pp. 120–127, 2018.

[37] D. Zhao, C. Han, Y. Li, J. Li, K. Zhou, Q. Wei, J. Liu, and Y. Shi, "Improvement on mechanical properties and corrosion resistance of titanium-tantalum alloys in-situ fabricated via selective laser melting," *Journal of Alloys and Compounds*, vol. 804, pp. 288–298, 2019.

[38] K. D. Traxel and A. Bandyopadhyay, "Reactive-deposition-based additive manufacturing of Ti-Zr-BN composites," *Additive Manufacturing*, vol. 24, pp. 353–363, 2018.

[39] R. Martinez, I. Todd, and K. Mumtaz, "In situ alloying of elemental Al-Cu12 feedstock using selective laser melting," *Virtual and Physical Prototyping*, vol. 14, no. 3, pp. 242–252, 2019.

[40] C. A. Biffi, A. G. Demir, M. Coduri, B. Previtali, and A. Tuissi, "Laves phases in selective laser melted TiCr1.78 alloys for hydrogen storage," *Materials Letters*, vol. 226, pp. 71–74, 2018.

[41] T. Nagase, T. Hori, M. Todai, S.-H. Sun, and T. Nakano, "Additive manufacturing of dense components in beta-titanium alloys with crystallographic texture from a mixture of pure metallic element powders," *Materials and Design*, vol. 173, p. 107771, 2019.

[42] T. Hanemann, L. N. Carter, M. Habschied, N. J. Adkins, M. M. Attallah, and M. Heilmaier, "In-situ alloying of AlSi10Mg+Si using Selective Laser Melting to control the coefficient of thermal expansion," *Journal of Alloys and Compounds*, vol. 795, pp. 8–18, 2019.

[43] S. Ewald, F. Kies, S. Hermsen, M. Voshage, C. Haase, and J. H. Schleifenbaum, "Rapid alloy development of extremely high-alloyed metals using powder blends in laser powder bed fusion," *Materials*, vol. 12, no. 10, p. 1706, 2019.

[44] Q. Guo, C. Zhao, M. Qu, L. Xiong, S. M. H. Hojjatzadeh, L. I. Escano, N. D. Parab, K. Fezzaa, T. Sun, and L. Chen, "In-situ full-field mapping of melt

flow dynamics in laser metal additive manufacturing," *Additive Manufacturing*, vol. 31, p. 100939, 2020.

[45] D. Lin, L. Xu, X. Li, H. Jing, G. Qin, H. Pang, and F. Minami, "A Si-containing FeCoCrNi high-entropy alloy with high strength and ductility synthesized in situ via selective laser melting," *Additive Manufacturing*, vol. 35, p. 101340, 2020.

[46] H. Dobbelstein, E. L. Gurevich, E. P. George, A. Ostendorf, and G. Laplanche, "Laser metal deposition of a refractory TiZrNbHfTa high-entropy alloy," *Additive Manufacturing*, vol. 24, pp. 386–390, 2018.

[47] H. Dobbelstein, E. L. Gurevich, E. P. George, A. Ostendorf, and G. Laplanche, "Laser metal deposition of compositionally graded TiZrNbTa refractory high-entropy alloys using elemental powder blends," *Additive Manufacturing*, vol. 25, pp. 252–262, 2019.

[48] S. Hocine, H. Van Swygenhoven, S. Van Petegem, C. S. T. Chang, T. Maimaitiyili, G. Tinti, D. Ferreira Sanchez, D. Grolimund, and N. Casati, "Operando X-ray diffraction during laser 3D printing," *Materials Today*, vol. 34, pp. 30–40, 2020.

[49] S. Hocine, S. Van Petegem, U. Frommherz, G. Tinti, N. Casati, D. Grolimund, and H. Van Swygenhoven, "A miniaturized selective laser melting device for operando X-ray diffraction studies," *Additive Manufacturing*, vol. 34, p. 101194, 2020.

[50] N. P. Calta, J. Wang, A. M. Kiss, A. A. Martin, P. J. Depond, G. M. Guss, V. Thampy, A. Y. Fong, J. Nelson Weker, K. H. Stone, C. J. Tassone, M. J. Kramer, M. F. Toney, A. Van Buuren, and M. J. Matthews, "An instrument for

in situ time-resolved X-ray imaging and diffraction of laser powder bed fusion additive manufacturing processes," *Review of Scientific Instruments*, vol. 89, p. 055101, 2018.

[51] N. P. Calta, V. Thampy, D. R. Lee, A. A. Martin, R. Ganeriwala, J. Wang, P. J. Depond, T. T. Roehling, A. Y. Fong, A. M. Kiss, C. J. Tassone, K. H. Stone, J. Nelson Weker, M. F. Toney, A. W. Van Buuren, and M. J. Matthews, "Cooling dynamics of two titanium alloys during laser powder bed fusion probed with in situ X-ray imaging and diffraction," *Materials and Design*, vol. 195, p. 108987, 2020.

[52] C. Leyens and M. Peters, eds., *Titanium and Titanium Alloys: Fundamentals and Applications*. Weinheim: Wiley-VCH Verlag GmbH & Co. KGaA, 2003.

[53] "Principles of Alloying Titanium," in *Titanium: Physical Metallurgy, Processing, and Applications* (F. H. Froes, ed.), pp. 51–74, Materials Park, OH: ASM International, 2015.

[54] J. D. Cotton, R. D. Briggs, R. R. Boyer, S. Tamirisakandala, P. Russo, N. Shchetnikov, and J. C. Fanning, "State of the Art in Beta Titanium Alloys for Airframe Applications," *JOM*, vol. 67, no. 6, pp. 1281–1303, 2015.

[55] L. M. Gammon, R. D. Briggs, J. M. Packard, K. W. Baston, R. Boyer, and C. W. Domby, "Metallography and Microstructures of Titanium and Its Alloys," in *ASM Handbook, Volume 9: Metallography and Microstructures* (G. F. Vander Voort, ed.), pp. 899–917, ASM International, 2004.

[56] H. Okamoto, "Al-V (Aluminum-Vanadium)," *Journal of Phase Equilibria and Diffusion*, vol. 22, no. 1, p. 86, 2001.

[57] C. L. A. Leung, S. Marussi, R. C. Atwood, M. Towrie, P. J. Withers, and P. D. Lee, "In situ X-ray imaging of defect and molten pool dynamics in laser additive manufacturing," *Nature Communications*, vol. 9, p. 1355, 2018.

[58] C. L. A. Leung, S. Marussi, M. Towrie, R. C. Atwood, P. J. Withers, and P. D. Lee, "The effect of powder oxidation on defect formation in laser additive manufacturing," *Acta Materialia*, vol. 166, pp. 294–305, 2019.

[59] Y. Chen, S. J. Clark, C. L. A. Leung, L. Sinclair, S. Marussi, M. P. Olbinado, E. Boller, A. Rack, I. Todd, and P. D. Lee, "In-situ Synchrotron imaging of keyhole mode multi-layer laser powder bed fusion additive manufacturing," *Applied Materials Today*, vol. 20, p. 100650, 2020.

[60] L. Sinclair, C. L. A. Leung, S. Marussi, S. J. Clark, Y. Chen, M. P. Olbinado, A. Rack, J. Gardy, G. Baxter, and P. D. Lee, "In situ radiographic and ex situ tomographic analysis of pore interactions during multilayer builds in laser powder bed fusion," *Additive Manufacturing*, p. 101512, 2020.

[61] D. Rosenthal, "The theory of moving sources of heat and its applications to metal treatments," *Transactions of the ASME*, vol. 68, no. 8, pp. 849–866, 1946.

[62] S. Bontha, N. W. Klingbeil, P. A. Kobryn, and H. L. Fraser, "Thermal process maps for predicting solidification microstructure in laser fabrication of thin-wall structures," *Journal of Materials Processing Technology*, vol. 178, no. 1-3, pp. 135–142, 2006.

[63] G. Lutjering and J. C. Williams, *Titanium*. Springer-Verlag Berlin Heidelberg, 2nd ed., 2007.

[64] S. Banerjee and P. Mukhopadyay, *Phase Transformations: Examples from Titanium and Zirconium Alloys*. Oxford: Pergamon, 2007.

[65] T. R. Allen, W. Huang, J. R. Tanner, W. Tan, J. M. Fraser, and B. J. Simonds, "Energy-Coupling Mechanisms Revealed through Simultaneous Keyhole Depth and Absorptance Measurements during Laser-Metal Processing," *Physical Review Applied*, vol. 13, p. 06070, 2020.

[66] J. I. Goldstein, D. E. Newbury, J. R. Michael, N. W. Ritchie, J. H. J. Scott, and D. C. Joy, *Scanning Electron Microscopy and X-Ray Microanalysis*. New York: Springer, 4th ed., 2018.

[67] W. E. King, H. D. Barth, V. M. Castillo, G. F. Gallegos, J. W. Gibbs, D. E. Hahn, C. Kamath, and A. M. Rubenchik, "Observation of keyhole-mode laser melting in laser powder-bed fusion additive manufacturing," *Journal of Materials Processing Technology*, vol. 214, pp. 2915–2925, 2014.

[68] R. Cunningham, C. Zhao, N. Parab, C. Kantzos, J. Pauza, K. Fezzaa, T. Sun, and A. D. Rollett, "Keyhole threshold and morphology in laser melting revealed by ultrahigh-speed x-ray imaging," *Science*, vol. 363, no. 6429, pp. 849–852, 2019.

[69] V.-P. Matilainen, H. Piili, A. Salminen, and O. Nyrhilä, "Preliminary Investigation of Keyhole Phenomena during Single Layer Fabrication in Laser Additive Manufacturing of Stainless Steel," *Physics Procedia*, vol. 78, pp. 377–387, 2015.

[70] E. W. Collings, *The Physical Metallurgy of Titanium Alloys*. Metals Park: American Society for Metals, 1984.

[71] H. Attar, M. Bönisch, M. Calin, L. C. Zhang, K. Zhuravleva, A. Funk, S. Scudino, C. Yang, and J. Eckert, "Comparative study of microstructures and mechanical properties of in situ Ti-TiB composites produced by selective laser melting, powder metallurgy, and casting technologies," *Journal of Materials Research*, vol. 29, no. 17, pp. 1941–1950, 2014.

[72] K. Geng, Y. Yang, S. Li, R. D. Misra, and Q. Zhu, "Enabling high-performance 3D printing of Al powder by decorating with high laser absorbing Co phase," *Additive Manufacturing*, vol. 32, p. 101012, 2020.

[73] C. Haase, F. Tang, M. B. Wilms, A. Weisheit, and B. Hallstedt, "Combining thermodynamic modeling and 3D printing of elemental powder blends for high-throughput investigation of high-entropy alloys – Towards rapid alloy screening and design," *Materials Science and Engineering A*, vol. 688, no. January, pp. 180–189, 2017.

[74] D. Zhao, C. Han, J. Li, J. Liu, and Q. Wei, "In situ fabrication of a titanium-niobium alloy with tailored microstructures, enhanced mechanical properties and biocompatibility by using selective laser melting," *Materials Science and Engineering C*, vol. 111, p. 110784, 2020.